UNIVERSIDAD AUTÓNOMA DE SAN LUÍS POTOSÍ

Doctorado Institucional en Ingeniería y Ciencia de Materiales

Additive-Synergized MICP for Heavy Metal Immobilization and Tailings Ecological Restoration

PARA OBTENER EL GRADO DE

DOCTOR EN INGENIERÍA Y CIENCIA DE MATERIALES

QUE PRESENTA
Zijia Zhang

DIRECTORA
Dra. Jessica Viridiana García Meza

PATROCINADO POR SECIHTI Beca número 814247

San Luis Potosí, SLP, Junio de 2026

UNIVERSIDAD AUTÓNOMA DE SAN LUÍS POTOSÍ

Doctorado Institucional en Ingeniería y Ciencia de Materiales

Heavy Metal Immobilization and Tailings Ecological Restoration via Additive-Engineered MICP

PARA OBTENER EL GRADO DE

DOCTOR EN INGENIERÍA Y CIENCIA DE MATERIALES

QUE PRESENTA

Zijia Zhang

DIRECTORA

Dra. Jessica Viridiana García Meza

Sinodales

Dra. Jessica Viridiana García Meza_____

Dra. Ling Xia_____

Dr. Lorenzo Borselli_____

Dr. Sergio Casa Flores_____

Dr. Edgar Daniel Páez Pérez_____

San Luis Potosí, SLP, Junio de 2026

Acknowledgement

This work was financially supported by the Hubei Provincial Natural Science Foundation of China (2023AFA087), the National Natural Science Foundation of China (22478311, 32061123009), and a doctoral scholarship (No. 814247) from the Mexican government through SECIHTI. The authors sincerely acknowledge this generous support, which was essential for the successful completion of this research.

I am deeply grateful to my doctoral supervisor, Dra. Jessica Viridiana García Meza, for her patient guidance throughout this research and thoughtful support in helping me adapt to life in Mexico. Far away from home, her kindness and encouragement have made this foreign country feel warm and familiar, and I will always cherish her trust and support. My sincere thanks also go to my joint supervisor, Dr. Zhenbin Wu, for his invaluable guidance, insightful suggestions, and continuous encouragement throughout my doctoral studies. I am also deeply thankful to Dra. Ling Xia, who has guided me since my master's studies and continued to support me during my doctoral research. She has provided steady support for my experimental equipment, instruments, and funding, while patiently instructing me on numerous academic details; her rigorous attitude and constant encouragement have accompanied me from my master's research to the completion of this doctoral dissertation, for which I am truly grateful. I further extend my heartfelt gratitude to Dr. Shaoxian Song, the principal investigator of our research group, whose valuable guidance and generous support have shaped my research framework, and whose trust has given me the confidence to grow as a researcher. I feel extremely fortunate to have had his guidance throughout this academic journey.

My sincere gratitude goes to the members of my doctoral dissertation committee: Dra. Ling Xia, Dr. Lorenzo Borselli (tutor), Dra. J. Viridiana García Meza, Dr. Sergio Casa Flores (externo), and Dr. Edgar Daniel Páez Pérez. Thank you for your valuable time, insightful comments, and rigorous review, which have greatly improved this dissertation. I deeply appreciate your guidance and support.

Finally, I thank my dear friends Jie Wu, Cui Zhang, Weiquan Zhan, Yuan Yuan, Keqiang Zhou, Yujing Bi, Jianhui Zhu, Lei Hou, etc. for their companionship and support throughout my doctoral journey. I also owe my deepest gratitude to my beloved parents, sister and wife for their selfless love and unwavering backing—you are my eternal spiritual pillar.

Abstract

Microbially Induced Carbonate Precipitation (MICP) offers a promising pathway for heavy metal immobilization, yet its practical application is constrained by four interconnected bottlenecks: loss of microbial activity under metal stress, poor control over mineralization kinetics, environmental risks from ammonia and chloride byproducts, and failure to restore soil ecological functions after treatment. To overcome these limitations, this study established a four-dimensional additive engineering framework targeting bioactivity maintenance, mineralization process control, byproduct risk mitigation, and ecological recovery. Four functional additive systems were systematically investigated.

In Chapter III, yeast extract was shown to act as a double-edged sword: moderate dosages promoted microbial growth and Cu^{2+} tolerance, whereas excessive concentrations chelated Cu^{2+} and suppressed carbonate precipitation, revealing a critical nutrient–ligand balance for maintaining bioactivity under metal stress.

In Chapter IV, montmorillonite-composite microcapsules provided a physical protective barrier that shielded microorganisms from lead toxicity, improved microbial survival and metabolic stability, and enhanced Pb immobilization through coupled adsorption and biomineralization.

In Chapter VI, a peat-coupled MICP system was developed for copper tailings, which stabilized Cu through carbonate precipitation, transformed harmful ammonia into plant-available nitrogen, improved soil carbon and nitrogen pools, and reconstructed indigenous microbial communities—thereby overcoming the "remediated but infertile" limitation of conventional MICP.

Collectively, this study elucidates the synergistic mechanisms of functional additives within the four-dimensional framework, optimizes key parameters for each system, and establishes a green, sustainable integrated technology for heavy metal immobilization and tailings ecological restoration. The findings enrich the theoretical foundation of MICP additive engineering and provide critical technical support for mine tailings management and ecological restoration.

Resumen

La precipitación de carbonato inducida por microorganismos (MICP, por sus siglas en inglés) constituye una estrategia prometedora para la inmovilización de metales pesados; sin embargo, su aplicación práctica se ve limitada por cuatro cuellos de botella interrelacionados: (i) la pérdida de actividad microbiana bajo estrés metálico, (ii) el escaso control de la cinética de mineralización, (iii) los riesgos ambientales asociados a subproductos como el amoníaco y los cloruros, y (iv) la incapacidad de restaurar las funciones ecológicas del suelo tras el tratamiento. Para superar estas limitaciones, el presente estudio estableció un marco de ingeniería de aditivos en cuatro dimensiones, orientado al mantenimiento de la bioactividad, el control del proceso de mineralización, la mitigación de riesgos por subproductos y la recuperación ecológica. En este contexto, se investigaron sistemáticamente cuatro sistemas de aditivos funcionales.

En el Capítulo III, se demostró que el extracto de levadura actúa como una espada de doble filo: dosis moderadas promovieron el crecimiento microbiano y la tolerancia al Cu^{2+}, mientras que concentraciones elevadas quelaron el Cu^{2+} y suprimieron la precipitación de carbonato, evidenciando un equilibrio crítico entre nutrientes y ligandos para mantener la bioactividad bajo estrés metálico.

En el Capítulo IV, las microcápsulas compuestas de montmorillonita proporcionaron una barrera protectora física que protegió a los microorganismos frente a la toxicidad del plomo, mejoró su supervivencia y estabilidad metabólica, y potenció la inmovilización de Pb mediante la adsorción acoplada con la biomineralización.

En el Capítulo VI, se desarrolló un sistema MICP acoplado con turba para relaves de cobre, el cual estabilizó el Cu mediante precipitación de carbonato, transformó el amoníaco nocivo en nitrógeno disponible para las plantas, mejoró los reservorios de carbono y nitrógeno del suelo, y reconstruyó las comunidades microbianas autóctonas, superando así la limitación de “remediado pero infértil” asociada a la MICP convencional.

En conjunto, este estudio dilucida los mecanismos sinérgicos de los aditivos funcionales dentro de un marco multidimensional, optimiza los parámetros clave de cada sistema y establece una tecnología integrada, verde y sostenible para la inmovilización de metales pesados y la restauración ecológica de relaves. Estos hallazgos amplían la base teórica de la ingeniería de aditivos aplicada a la MICP y proporcionan un soporte técnico sólido para la gestión de relaves mineros y la restauración ecológica.

CONTENTS

Index of Figures

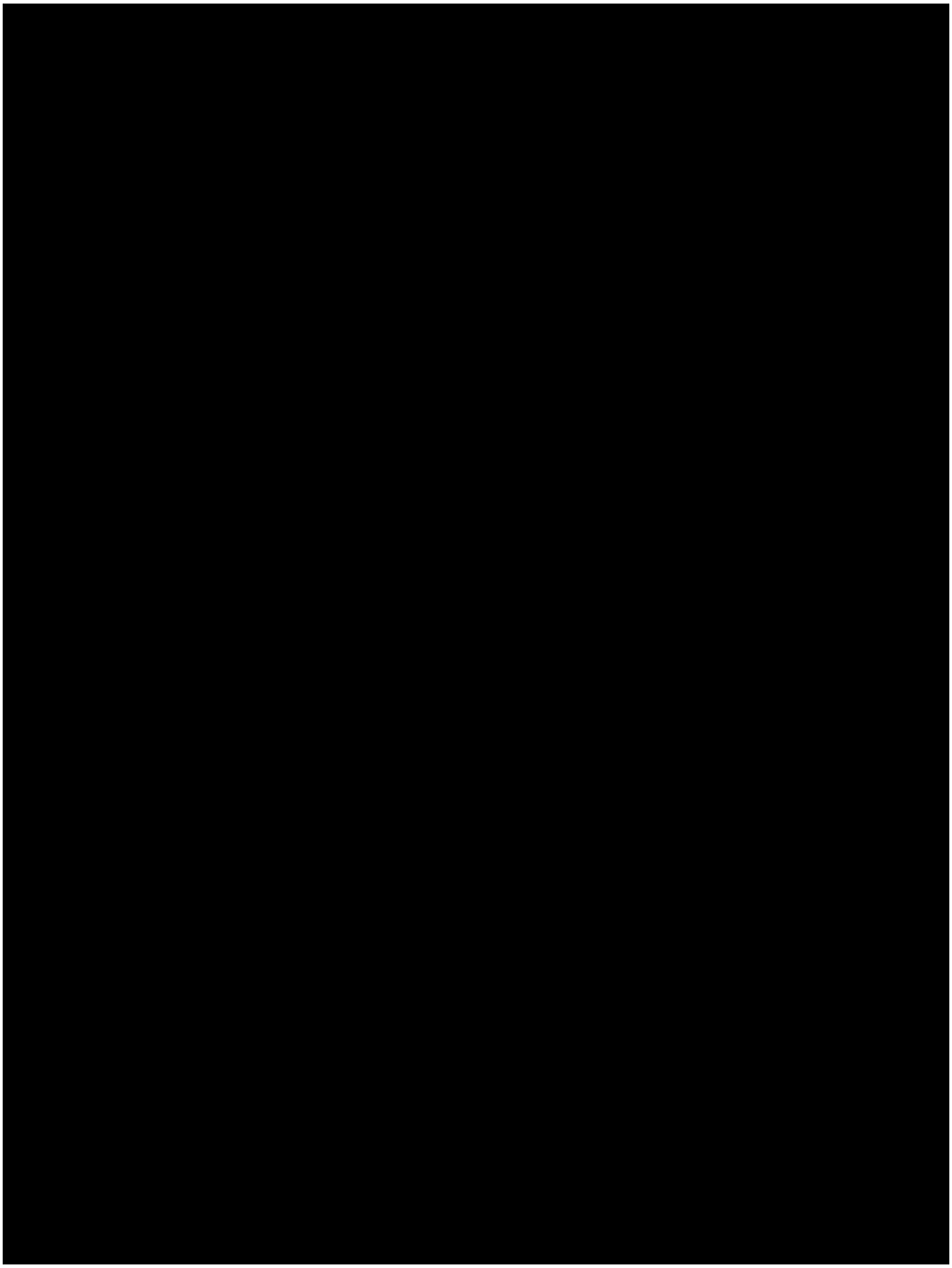

Index of Tables

Chapter I. Introduction

1.1 Justification

Heavy metal contamination of soil and water resources has emerged as a critical global environmental issue, threatening ecosystem integrity and public health. Industrial activities such as mining, smelting, electroplating, and chemical manufacturing have released substantial quantities of toxic metals—including copper, lead, cadmium, and zinc—into the environment [1-3]. Unlike organic pollutants, heavy metals are non-biodegradable and persist in ecosystems, accumulating through food chains and posing chronic health risks to humans and wildlife, such as neurological disorders, kidney damage, developmental abnormalities, and various cancers [4-6]. It is estimated that over 20 million hectares of agricultural soil worldwide are contaminated by heavy metals, causing significant economic losses of hundreds of billions of dollars annually due to reduced crop yields and degraded ecosystem services [1, 7]. Conventional remediation technologies, including soil excavation, chemical washing, and solidification/stabilization, are often limited by high costs, secondary pollution risks, damage to soil structure, and poor scalability for large-scale applications [8-10]. Phytoremediation, despite its environmental friendliness, is restricted by long remediation cycles, low biomass productivity of hyperaccumulator plants, and challenges in the post-remediation disposal of contaminated biomass [11-13]. Therefore, there is an urgent need to develop green, efficient, and sustainable in-situ remediation technologies that can simultaneously immobilize heavy metals and restore ecological functions.

Microbially Induced Carbonate Precipitation (MICP) has emerged as a promising biotechnological approach for heavy metal remediation [14, 15]. This technology harnesses diverse microbial metabolic pathways—including urea hydrolysis, denitrification, sulfate reduction, photosynthesis, ammonification, and methane oxidation—to generate carbonate ions that precipitate with metal cations to form stable carbonate minerals [16-18]. Among these pathways, urea hydrolysis mediated by ureolytic bacteria is the most widely adopted, owing to its high reaction efficiency, controllability, abundant microbial resources, and mature engineering applications [19, 20]. Denitrification and sulfate reduction pathways are advantageous for anaerobic environments, while photosynthetic pathways enable carbon sequestration coupled with metal immobilization [21-23]. Regardless of the metabolic pathway, MICP

presents distinct merits: the biological process occurs under ambient temperature and pressure without harsh chemical reagents; the resulting carbonate precipitates feature high thermodynamic stability, ensuring long-term metal immobilization with low leaching toxicity; and the mineralization products exert both cementation and filling effects, which can improve soil aggregate structure, enhance mechanical stability, and reduce permeability [24-26].

Nevertheless, the practical application of MICP in heavy metal-contaminated environments is constrained by four interconnected bottlenecks that severely limit its remediation efficiency, long-term stability, and environmental sustainability [27, 28]. First, microbial bioactivity is impaired under heavy metal stress: metal ions damage cell membrane integrity, inhibit key metabolic enzymes such as urease, interfere with energy metabolism, and induce oxidative stress, leading to delayed reaction initiation and reduced mineralization efficiency [29, 30]. Second, the mineralization process is poorly controllable: different metal ions exert differential effects on crystal nucleation energy barriers, growth kinetics, and phase stability, potentially resulting in uneven precipitate distribution, formation of metastable soluble phases, pore clogging, and compromised long-term stability of immobilized metals [31, 32]. Third, byproducts generate environmental risks: the MICP process produces considerable ammonium nitrogen (approximately 2 mol of NH_4^+ per mole of $CaCO_3$ precipitated), which may contribute to water eutrophication, while chloride ions from conventional calcium chloride substrates accumulate and can induce soil salinization, degrading soil structure and inhibiting plant growth [33-35]. Fourth, ecological compatibility is insufficient: the injection of high-concentration cementation solutions, combined with alkaline conditions and byproduct toxicity, can substantially reduce the diversity of indigenous soil microbial communities, disrupt key biogeochemical cycles, and leave remediated sites in a state that cannot support self-sustaining ecosystems [36, 37].

To address these critical bottlenecks, this study proposes an additive engineering strategy that shifts from traditional single-factor optimization to multi-objective synergistic regulation. Based on a systematic literature review, a four-dimensional regulatory framework is established, covering bioactivity maintenance, mineralization process control, byproduct risk mitigation, and ecological function recovery. Through systematic investigation of functional additives (organic nutrients, clay minerals, waste-derived materials, and natural organic substrates), this research aims to enhance microbial tolerance, regulate mineralization kinetics, convert harmful byproducts into

valuable resources, and restore soil fertility and microbial community structure simultaneously. By elucidating the synergistic mechanisms between functional materials and the MICP system within this framework, optimizing key parameters for each synergistic system, and verifying its effectiveness via laboratory tests and field-scale applications, this study intends to upgrade MICP from a single heavy metal immobilization technique to a comprehensive ecological restoration platform, providing theoretical foundations and technical support for the sustainable remediation of heavy metal-contaminated mine tailings and industrial sites.

1.2 Objectives

1.2.1 General objective

To establish a four-dimensional additive engineering framework for Microbially Induced Carbonate Precipitation (MICP) that synergistically addresses the key bottlenecks of microbial bioactivity maintenance, mineralization process control, byproduct risk mitigation, and ecological function recovery, thereby developing a green, efficient, and sustainable integrated remediation technology for heavy metal-contaminated sites.

1.2.2 Goals

(1) For bioactivity maintenance: to elucidate the nutrient–ligand trade-off of yeast extract and its dual role in MICP-based copper remediation.

(2) For bioactivity protection: to prepare montmorillonite-based microcapsules for shielding functional microorganisms and enhancing lead immobilization.

(3) For mineralization process control: to repurpose functionalized nanoplastics as MICP accelerators for the simultaneous removal of copper and nanoplastics.

(4) For byproduct risk mitigation and ecological function recovery: to construct a peat-integrated MICP system for heavy metal immobilization and ecological restoration of copper tailings.

References

[1] L. Liu, W. Li, W. Song, M. Guo, Remediation techniques for heavy metal-contaminated soils: Principles and applicability, Sci. Total Environ., 633 (2018) 206-219.

[2] Y. Du, L. Chen, P. Ding, L. Liu, Q. He, B. Chen, Y. Duan, Different exposure profile

of heavy metal and health risk between residents near a Pb-Zn mine and a Mn mine in Huayuan county, South China, Chemosphere, 216 (2019) 352-364.

[3] M. Adnan, B.H. Xiao, M.U. Ali, P.W. Xiao, P. Zhao, H.Y. Wang, S. Bibi, Heavy metals pollution from smelting activities: A threat to soil and groundwater, Ecotoxicology and Environmental Safety, 274 (2024).

[4] L. Tong, A. Yang, M. Fan, D. Zheng, J. Li, H. Liu, C. Li, Y. Tang, L. Cheng, Assessment of heavy metal sources and health risks in soil-crop systems of fragmented farmland, Frontiers in public health, 13 (2025) 1637595.

[5] G.J. Brewer, Risks of Copper and Iron Toxicity during Aging in Humans, Chemical Research in Toxicology, 23 (2010) 319-326.

[6] Z. Mei, G. Liu, B. Zhao, Z. He, S. Gu, Emerging roles of epigenetics in lead-induced neurotoxicity, Environment International, 181 (2023) 108253.

[7] Q.C. Zhang, C.C. Wang, Natural and Human Factors Affect the Distribution of Soil Heavy Metal Pollution: a Review, Water Air and Soil Pollution, 231 (2020).

[8] A. Azimi, A. Azari, M. Rezakazemi, M. Ansarpour, Removal of Heavy Metals from Industrial Wastewaters: A Review, ChemBioEng Reviews, 4 (2017) 37-59.

[9] X.Y. Nie, X.H. Huang, M. Li, Z.C. Lu, X.H. Ling, Advances in Soil Amendments for Remediation of Heavy Metal-Contaminated Soils: Mechanisms, Impact, and Future Prospects, Toxics, 12 (2024).

[10] W.Y. Shi, H.B. Shao, H. Li, M.A. Shao, S. Du, Progress in the remediation of hazardous heavy metal-polluted soils by natural zeolite, Journal of Hazardous Materials, 170 (2009) 1-6.

[11] S.Y. Bai, X. Han, D. Feng, Shoot-root signal circuit: Phytoremediation of heavy metal contaminated soil, Frontiers in Plant Science, 14 (2023).

[12] B.G.E. Sierra, J.M. Guerrero, S. Sokolski, Phytoremediation of Heavy Metals in Tropical Soils an Overview, Sustainability, 13 (2021).

[13] A. Mahar, P. Wang, A. Ali, M.K. Awasthi, A.H. Lahori, Q. Wang, R.H. Li, Z.Q. Zhang, Challenges and opportunities in the phytoremediation of heavy metals contaminated soils: A review, Ecotoxicology and Environmental Safety, 126 (2016) 111-121.

[14] Y.R. Dong, Z.Q. Gao, J.Z. Di, D. Wang, Z.H. Yang, Y.F. Wang, X.Y. Guo, K.F. Li, Experimental study on solidification and remediation of lead-zinc tailings based on microbially induced calcium carbonate precipitation (MICP), Constr. Build. Mater., 369 (2023).

[15] S. Wang, L. Fang, M.F. Dapaah, Q. Niu, L. Cheng, Bio-Remediation of Heavy Metal-Contaminated Soil by Microbial-Induced Carbonate Precipitation (MICP)—A Critical Review, in: Sustainability, 2023, pp. 7622.

[16] J.Q. Tan, H. Yi, Z.J. Zhang, D.L. Meng, Y.T. Li, L. Xia, S.X. Song, L. Wu, R.M.T. Sáncheze, M.E. Farías, Montmorillonite facilitated Pb(II) biomineralization by Chlorella sorokiniana FK in soil, Journal of Hazardous Materials, 423 (2022).

[17] L.Y. Alvarado-Mata, J.M. Sánchez-Lozano, J.I. de la Torre, A.R. Alvarez-Valdez, J.P. Salinas-Mireles, A.Y.C. Hita-Wong, M.J. Castro-Alonso, M.P. Luevanos-Escareño, R. Narayanasamy, N. Balagurusamy, Advances in microbially induced carbonate precipitation metabolic pathways and regulatory mechanisms for bioconcrete development, Journal of Sustainable Cement-Based Materials, 14 (2025) 1987-2011.

[18] M. Seifan, A. Berenjian, Microbially induced calcium carbonate precipitation: a widespread phenomenon in the biological world, Applied Microbiology and Biotechnology, 103 (2019) 4693-4708.

[19] Y.Z. Liu, K.J. Hu, M.L. Pan, W. Dong, X.J. Wang, X.Y. Zhu, Research and Application of Green Technology Based on Microbially Induced Carbonate Precipitation (MICP) in Mining: A Review, Sustainability, 17 (2025).

[20] D. Arias, K. Gallardo, M. Saldana, F. Galleguillos-Madrid, Urease-Driven Microbially Induced Carbonate Precipitation (MICP) for the Circular Valorization of Reverse Osmosis Brine Waste: A Perspective Review, in: Minerals, 2025, pp. 543.

[21] Y.Q. Gao, L.Y. Wang, J. He, J. Ren, Y.F. Gao, Denitrification-based MICP for cementation of soil: treatment process and mechanical performance, Acta Geotechnica, 17 (2022) 3799-3815.

[22] M.J. Castro-Alonso, L.E. Montañez-Hernandez, M.A. Sanchez-Muñoz, M.R.M. Franco, R. Narayanasamy, N. Balagurusamy, Microbially Induced Calcium Carbonate Precipitation (MICP) and Its Potential in Bioconcrete: Microbiological and Molecular Concepts, Frontiers in Materials, 6 (2019).

[23] Z.J. Zhang, K.Q. Zhou, J.V. Garcia-Meza, S.X. Song, L. Xia, Montmorillonite enhances the remediation of lead (II) by polyvinyl alcohol/sodium alginate/Chlorella sorokiniana FK microcapsules, Applied Clay Science, 273 (2025).

[24] M. Chen, Y. Li, X. Jiang, D. Zhao, X. Liu, J. Zhou, Z. He, C. Zheng, X. Pan, Study on soil physical structure after the bioremediation of Pb pollution using microbial-induced carbonate precipitation methodology, Journal of Hazardous Materials, 411 (2021) 125103.

[25] S.H. Liu, K.J. Wen, C. Armwood, C.M. Bu, C. Li, F. Amini, L. Li, Enhancement of MICP-Treated Sandy Soils against Environmental Deterioration, Journal of Materials in Civil Engineering, 31 (2019).

[26] G.S. Ji, C.C. Huan, Y. Zeng, Q. Lyu, Y.L. Du, Y. Liu, L.S. Xu, Y. He, X.P. Tian, Z.Y. Yan, Microbiologically induced calcite precipitation (MICP) in situ remediated heavy metal contamination in sludge nutrient soil, Journal of Hazardous Materials, 473 (2024).

[27] Z. Wang, H. Qin, X. Dong, W. Zhang, Classification of additives and their influence mechanisms in improving the performance of biologically induced carbonate precipitation, Environmental Research, 275 (2025) 121376.

[28] A.J. Mugwar, M.J. Harbottle, Toxicity effects on metal sequestration by microbially-induced carbonate precipitation, Journal of Hazardous Materials, 314 (2016) 237-248.

[29] L. Fang, Q. Niu, L. Cheng, J. Jiang, Y.-Y. Yu, J. Chu, V. Achal, T. You, Ca-mediated alleviation of Cd2+ induced toxicity and improved Cd2+ biomineralization by Sporosarcina pasteurii, Sci. Total Environ., 787 (2021) 147627.

[30] W. Zhang, H. Zhang, R. Xu, H. Qin, H. Liu, K. Zhao, Heavy metal bioremediation using microbially induced carbonate precipitation: Key factors and enhancement strategies, Front Microbiol, 14 (2023) 1116970.

[31] M. Şimşek, S. Çelik, H. Akoğuz, Comparative Study of Mechanical and Microstructural Properties of Biocemented Sandy Soils Enhanced with Biopolymer: Evaluation of Mixing and Injection Treatment Methods, in: Applied Sciences, 2025, pp. 8090.

[32] J.T. DeJong, B.M. Mortensen, B.C. Martinez, D.C. Nelson, Bio-mediated soil improvement, Ecological Engineering, 36 (2010) 197-210.

[33] J. Xiang, J. Qiu, Y. Wang, X. Gu, Calcium acetate as calcium source used to biocement for improving performance and reducing ammonia emission, Journal of Cleaner Production, 348 (2022) 131286.

[34] Y.-t. Duan, X. Xu, L. Niu, Z. Wang, X.-g. Huang, C.-l. Zheng, Study on the mechanism and stability of microbially induced struvite precipitation (MISP) for enhanced immobilization of uranium, Journal of Cleaner Production, 449 (2024) 141536.

[35] W. Nie, J. Shi, R.X. Li, W.J. Niu, Q.F. Tian, K. Tong, Z.H. Zhang, Coupled MICP-MISP biotechnologies for eco-friendly dust control in open-pit coal mines: Strength

enhancement and ammonium recycling, Journal of Environmental Chemical Engineering, 13 (2025).
[36] Z. Zhang, Q. Zhang, J.V. Garcia-Meza, Z. Wu, D. Meng, L. Xia, Synergistic effects of peat and MICP for copper tailings remediation: Metal immobilization, nutrient retention, and microbial regulation, Journal of Hazardous Materials, 502 (2026) 141028.
[37] M. Xu, J. Ma, X.H. Zhang, G. Yang, L.L. Long, C. Chen, C. Song, J. Wu, P. Gao, D.X. Guan, Biochar-bacteria partnership based on microbially induced calcite precipitation improves Cd immobilization and soil function, Biochar, 5 (2023).

Chapter III. Yeast Extract as a Double-Edged Sword in Microbial Induced Carbonate Precipitation for Copper Remediation: Unraveling the Nutrient - Ligand Dilemma

3.1 Introduction

The rapid progression of industrialization has precipitated a global surge in heavy metal-contaminated wastewater, with copper (Cu^{2+}) emerging as a predominant contaminant due to its extensive use in mining, metallurgy, and chemical industries [1-4]. Annually, millions of tons of copper-laden effluents are discharged into aquatic ecosystems, where Cu^{2+} persists due to its non-degradability and bioaccumulates through the food chain, ultimately endangering human health [5]. Chronic exposure to elevated Cu^{2+} levels disrupt cellular homeostasis by binding irreversibly to sulfhydryl groups in enzymes and proteins, leading to neurodegenerative disorders, hepatic cirrhosis, and renal dysfunction [6-9]. Conventional remediation methods, such as chemical precipitation and ion exchange, face critical limitations, including high operational costs, sludge generation, and inefficiency in low-concentration systems [10-12]. In contrast, bio-based strategies, particularly microbial-induced carbonate precipitation (MICP), offer a sustainable alternative by leveraging natural biogeochemical processes for metal immobilization [13, 14].

Current MICP technologies primarily exploit three metabolic pathways: urea hydrolysis, nitrate reduction, and photosynthesis [15-18]. Among these, the urea hydrolysis pathway has been the most extensively studied. In this process, ureolytic bacteria enzymatically convert urea into carbonate ions (CO_3^{2-}) and ammonia (NH_3). The generated CO_3^{2-} reacts with divalent metal cations (e.g., Cu^{2+}, Ca^{2+}) to form insoluble carbonate precipitates [19, 20]. Meanwhile, the hydrolysis of ammonia leads to an increase in environmental pH, which helps maintain a stable state of carbonate precipitate [21, 22]. Research has shown that this technology has high removal efficiency for metal cations such as Pb^{2+} and Cd^{2+}, as well as radioactive nuclides [13, 23, 24]. For instance, MICP leveraging nano-hydroxyapatite (nHAP) effectively immobilizes Pb^{2+} by facilitating ion exchange (Ca^{2+}/Pb^{2+}) and subsequent formation of stable carbonate-bearing pyromorphite [24]. Nevertheless, when it comes to dealing with transition metal ions such as Cu^{2+}, significant differences in their removal rates are

observed. The lowest removal rate is approximately 0%, while the highest can reach over 90% [25-27]. Scholars attribute the low copper removal efficiency to the formation of the stable copper ammonia complexes, $[Cu(NH_3)_4]^{2+}$, between Cu^{2+} and ammonia released from urea hydrolysis under alkaline conditions [28, 29]. However, when the urea concentration in the reaction solution was adjusted, no significant change in the copper removal rate was observed [30]. Thus, we have reason to believe that apart from copper-ammonia complexes, there are other factors contributing to the differences in Cu^{2+} removal rates.

A pivotal yet overlooked factor lies in the organic nutrients essential for bacterial cultivation. Standard MICP protocols rely on complex media enriched with yeast extract (YE), peptone, or beef extract to supply carbon, nitrogen, and micronutrients [20, 31]. Studies have shown that these organic components contain rich coordination groups (e.g., amino, carboxyl, hydroxyl groups), which can form very stable complexes with a variety of transition metal ions in solution (e.g., Cu^{2+}, Ni^{2+}) [32-34]. Interestingly, when comparing literature on different Cu^{2+} removal rates, it is noted that Cu^{2+} typically exhibits lower removal efficiencies in organic-rich media. For example, when the medium contains 3 g/L beef extract, the Cu^{2+} removal efficiency is about 10%, while with 2 g/L yeast extract, it is almost 0% [25, 28]. Conversely, when tested in a medium containing only physiological saline or 0.5 M urea, Cu^{2+} removal rates substantially increased, reaching approximately 75% and 90%, respectively [27, 35]. This inverse correlation implies that organic components may sequester Cu^{2+} into soluble complexes, thereby limiting the bioavailability of Cu^{2+} for carbonate co-precipitation. This mechanism is further corroborated by parallel findings on the role of organic functional groups in metal adsorption and immobilization [36, 37]. Despite its profound implications, the role of organic additives in modulating Cu^{2+} speciation and MICP efficacy remains unexplored.

In this study, yeast extract (YE) was deliberately selected over other common complex nutrients such as beef extract and peptone, not only for its role as a rich source of vitamins, peptides, and growth factors that are essential to microbial proliferation, but more critically for its consistently high content of amino acids and multifunctional groups that confer superior metal-chelating capability. We hypothesize that at higher concentrations, YE's chelation effect outweighs its nutritional contributions, resulting in competitive binding of Cu^{2+} and consequent inhibition of carbonate precipitation. To test this hypothesis, we aim to: (i) isolate ureolytic bacteria exhibiting high copper

tolerance from copper tailings; (ii) investigate the influence of YE concentration on bacterial growth, copper resistance, and the efficacy of carbonate precipitation for Cu^{2+} removal; and (iii) analyze copper speciation changes via UV-visible (UV-vis) absorption spectrum and competitive ligand exchange-adsorptive cathodic stripping voltammetry (CLE-ACSV) techniques to unravel the mechanistic role of YE in modulating MICP performance.

3.2 Materials and methods

3.2.1 Isolation and identification of ureolytic bacteria

10 g of contaminated soil collected from a gold-copper mine in China was weighed and added into sterile water at a solid-to-liquid ratio of 1:10. The soil was placed in a shaking bed at 30 ℃ and 150 rpm for 12 h and then left to stand for 30 min. The supernatant was diluted with concentration gradients of 10^{-2}, 10^{-3}, 10^{-4}, 10^{-5}, and 10^{-6} to obtain the diluent. 1 mL of the diluent at different gradients was pipetted and evenly spread on the separation medium (5 g/L peptone, 5 g/L NaCl, 0.01 g/L $NiCl_2 \cdot 6H_2O$, 1.5 g/L YE, 1.5 g/L beef extract, 10 g/L agar, 0.012 g/L phenol red). The medium was incubated in a biochemical incubator at 30 ℃ until colonies emerged and the medium turned red. Subsequently, colonies with a red halo were selected and inoculated, and repeated cultures were carried out until purified single colonies were obtained. The isolated and purified strains were identified by 16S rDNA gene sequencing. The morphology of the bacterial strains was observed using scanning electron microscopy (SEM, TESCAN MIRA/CZ).

3.2.2 Growth and Cu^{2+} tolerance of SX1 at different YE concentrations

SX1 was inoculated into a nutrient broth medium (comprising 1.5 g/L YE, 2.7 g/L glucose, 5 g/L sodium chloride, with a pH of 6.8 ± 0.2). It was then incubated at 150 rpm and 30 °C for 24 h. Subsequently, the culture was centrifuged and washed to prepare a bacterial suspension with an optical density at 600 nm (OD_{600}) of 1. The concentrations of other substances in the culture medium were maintained constant, while the YE concentration was adjusted to 0, 0.5, 1, 1.5, 2, and 3 g/L. After inoculating 2% (v/v) of this bacterial suspension, samples were taken at 0, 4, 8, 12, 24, 36, and 48 h of cultivation to measure the OD_{600}.

Culture media containing 0.5, 1, 1.5, 2, and 3 g/L YE were prepared. A series of Cu^{2+} concentrations (0, 0.1, 0.5, 1, 2, 4, 6, and 8 mM) were added to these media and

mixed thoroughly. Next, a 2% (v/v) bacterial suspension (OD_{600} = 1) was inoculated, and the cultures were incubated in a constant temperature incubator for 48 h. After that, samples were taken to measure the OD_{600}. Finally, GraphPad Prism software was utilized to calculate the half - maximal inhibitory concentration (IC_{50}).

3.2.3 Cu^{2+} removal experiments

A 2% (v/v) bacterial suspension (OD_{600} = 1) was inoculated into a nutrient broth urea medium containing 5 mM copper. The medium also consisted of 0.5, 1.0, 1.5, 2, or 3 g/L YE, 2.7 g/L glucose, 5 g/L sodium chloride, 1.0 g/L urea, and had a pH of 6.8 ± 0.2. Samples were taken at 0, 4, 8, 12, 24, 36, and 48 h to determine urease activity, NH_4^+-N concentration, and copper concentration. Urease activity was determined using the phenol - hypochlorite photometric method [38]. First, 250 μL of the sample was added to a mixed solution composed of 1 mL phosphate potassium buffer (0.1 M, pH = 8) and 2.5 mL urea (0.1 M). This mixture was then incubated at 37°C for 5 min. Subsequently, 1 mL each of phenol nitroprusside and alkaline hypochlorite were added, and the incubation continued at 37 °C for an additional 25 min. The optical density was finally measured at a wavelength of 626 nm. NH_4^+-N concentration was determined by Nessler's reagent spectrophotometry [39]. Briefly, an appropriate amount of the sample was transferred into a 50 mL colorimeter and diluted to the mark with deionized water. 1 mL of potassium sodium tartrate solution was added and mixed well, followed by the addition of 1 mL of Nessler reagent. The solution was stirred thoroughly. After standing for 10 min, the optical density was measured at a wavelength of 420 nm. The concentration of Cu^{2+} was determined by flame atomic absorption spectroscopy (AAS, PERKIN ELMER/USA).

After the 48h reaction was completed, the final pH value of the solution was measured using an acidity meter (S400 Basic/USA). We used the para-dimethyl-amino-benzaldehide (PDAB) method to determine the concentration of urea (S400 Basic/USA) [19]. In brief, an appropriate amount of the sample was placed into a 25 mL colorimetric tube. Then, 10 mL of PDAB and 4 mL of sulfuric acid solution (2 mM) were added, and the volume was adjusted to the mark with deionized water. The mixture was shaken well and allowed to stand for 10 minutes before measuring the absorbance at 422 nm. Finally, based on the measured amount of decomposed urea, the theoretical NH_4^+-N concentration was calculated with a 1:2 ratio. All experiments were conducted in triplicate under controlled temperature conditions (30 ± 2 °C) for microbial cultivation.

Analytical measurements were performed at ambient temperature (25 ± 2 °C) unless otherwise specified.

3.2.4 Characterization of Mineralized Products

The precipitate was enriched by centrifugation at 8000 rpm for 10 min. It was then washed three times with sterile water and finally freeze - dried to obtain the mineralized products. An analytical balance (AP135W/JPN) was used to determine the weight of the dry mineralized precipitates. Scanning electron microscopy (SEM) and energy dispersive spectroscopy (EDS, TESCAN-MIRA/CZ) were used to analyze the microstructure and element distribution of mineralized precipitates. X-ray diffraction (XRD, D8 ADVANCE/GER) was used to analyze the crystal structure of mineralized precipitates. Fourier transform infrared spectroscopy (FT-IR, NEXUS/USA) was used to identify surface functional groups of mineralized precipitates. Thermogravimetric analyzer (STA449F3, GER) was used to evaluate the mass loss (TG) and mass loss rate (dTG) of mineralized precipitates at a heating rate of 10 ℃/min in a nitrogen atmosphere within the range of room temperature to 1000 ℃. X-ray photoelectron spectroscopy (XPS, ESCALAB 250Xi/USA) was used to analyze the chemical valence states of carbon, oxygen, and copper elements in mineralized precipitates.

3.2.5 Cu^{2+}-YE interaction experiments

To understand the interaction between Cu^{2+} and YE, a series of experiments were carried out. First, prepare solutions with YE concentrations of 0.5, 1, 1.5, 2, and 3 g/L. Sterilize these solutions at 121 ℃ for 20 min. Subsequently, add 0 - 8 mM copper to each group, mix thoroughly, and use a UV-visible spectrophotometer (UV-vis, DR6000/USA) to dilute and determine the UV-vis spectrum within the range of 200 - 500 nm.

Competitive ligand exchange-adsorptive cathodic stripping voltammetry (CLE-ACSV) has been widely used for the morphological analysis of metal ions in water [40, 41]. The main process of this technology is as follows: first, the competing ligand (salicylaldoxime, SA) is added to the Cu^{2+}-YE composite water body. After reaction equilibrium, Cu^{2+} in the water body will exist in various forms, and its total concentration can be described by the mass balance equation (Eq.1):

$$[Cu]_T = [Cu^{2+}] + \sum_i [CuX_i] + \sum [CuSA_x] + \sum [CuYE] \quad (1)$$

Where $[Cu]_T$ is the total dissolved copper, $[Cu^{2+}]$ is the free copper ion, $[CuX_i]$,

[$CuSA_x$] and [CuYE] are the complexes formed by the combination of copper with inorganic ligand (X_i), competitive ligand (SA) and YE ligand. Due to the negligible presence of free copper ion and inorganic ligand complexed copper, (Eq. 1) can be abbreviated as (Eq. 2):

$$[Cu]_T = \sum[CuSA_x] + \sum[CuYE] = [Cu^{2+}]\left(\alpha'_{CuSA_x} + \alpha'_{CuYE}\right) \quad (2)$$

Where the conditional side reaction coefficient (α'_{CuSA_x} and α'_{CuYE}) of copper complexing with SA and YE. SA undergoes secondary hydrolysis with Cu^{2+} to form two types of complexes, 1:1 and 1:2 ([$CuSA^+$] and [$CuSA_2$]). Typically, macromolecular organic ligand (such as YE) combine with metal ions to form 1:1 complexe ([CuYE]) [32]. Therefore, α'_{CuSA_x} and α'_{CuYE} are as follows (Eq. 3-4):

$$\alpha'_{CuSA_x} = \frac{\sum[CuSA_x]}{[Cu^{2+}]} = \frac{[CuSA^+]+[CuSA_2]}{[Cu^{2+}]} = K'_{CuSA}[SA] + K'_{CuSA_2}[SA]^2 \quad (3)$$

$$\alpha'_{CuYE} = \frac{\sum[CuYE]}{[Cu^{2+}]} = K'_{CuYE}[YE] \quad (4)$$

Among them, [SA] and [YE] are the concentrations of SA and YE in the solution, respectively; K'_{CuSA}, K'_{CuSA_2} and K'_{CuYE} are the conditional stability constants for [$CuSA^+$], [$CuSA_2$] and [CuYE], respectively. According to previous research, the calculation equation of K'_{CuSA} and K'_{CuSA_2} are shown in (Eq. 5) and (Eq. 6) respectively. Considering that the salinity in this work is approximately zero, take an approximate value of salinity = 1×10^{-5} [42].

$$log(K'_{CuSA}) = (10.12 \pm 0.03) - (0.37 \pm 0.02)\ log\ (Salinity) \quad (5)$$

$$log\ (K'_{CuSA_2}) = (15.78 \pm 0.08) - (0.53 \pm 0.07)\ log(Salinity) \quad (6)$$

Subsequently, labile copper (free copper ion, inorganic complexed copper, and copper complexed with SA, Eq. 7) will be adsorbed onto the hanging mercury electrode. Finally, by applying a cathodic scanning potential, the adsorbed Cu^{2+} will be reduced to Cu (0) and generate a current signal (Eq. 8).

$$[Cu_{labile}] = \sum[CuSA_x] = \alpha'_{CuSA_x}[Cu^{2+}] \quad (7)$$

$$i_p = S[Cu_{labile}] \quad (8)$$

Where i_p is the peak current measured by the instrument, and S is the sensitivity of the method. When a copper concentration sufficient to saturate ligands in yeast extract is added, the relationship between current and added copper will become linear. The slope of these linear regions is the calibrated S.

According to different titration concentrations, [CuYE] and [Cu^{2+}] can be calculated using equations (9) and (10). By fitting the modified version of the Langmuir equation (Eq. 11) to the data of [CuYE] and [Cu^{2+}], the total ligand concentration $[YE]_T$

and conditional stability constant K'_{CuYE} can be obtained.

$$[CuYE] = [Cu]_T - [Cu_{labile}] \quad (9)$$

$$[Cu^{2+}] = \frac{[Cu_{labile}]}{\alpha'_{CuSA_x}} \quad (10)$$

$$[CuYE] = [YE]_T \frac{K'_{CuYE}[Cu^{2+}]}{1+K'_{CuYE}[Cu^{2+}]} \quad (11)$$

Based on the above theory, the specific measurement steps are as follows: An appropriate amount of sterilized YE solution was placed in a Teflon (FEP) voltammetric cup, followed by the addition of 6.0 mM HEPPS buffer. Then, 0-12 μM copper was added and the solution was equilibrated for 1 h. Subsequently, 50 μM SA-a concentration optimized through preliminary titration tests to ensure effective competition with Cu^{2+} while minimizing background interference-was introduced. The final solution volume is 10 mL, with YE concentrations of 0, 0.001, 0.002, and 0.003 g/L. The measurement was performed using LviumStart electrochemical workstation, equipped with a hanging mercury drop electrode (HDME), a saturated Ag/AgCl reference electrode, and a platinum wire counter electrode. First, blow the sample with high-purity nitrogen gas for 5 min, and then deposit at a potential of -0.3 V for 120 s. After 20 s of equilibrium, scan the sample in differential pulse mode in the range of 0 V to -0.6 V, generating a current proportional to Cu_{labile} concentration.

3.3 Results and discussion

3.3.1 Isolation and identification of strain SX1

When urease producing bacteria break down urea to produce ammonia, it causes the pH of the surrounding environment to increase, turning a plate culture-medium containing phenol red (a pH indicator) from orange to red. Based on this principle, a target strain (SX1) was selected, which turned the plate red (Figure 3.1 a-b). Microscopic examination showed that SX1 was rod-shaped (Figure 3.1 c). The 16SrDNA sequence of strain SX1 was compared by BLAST in the NCBI database, and the result showed that SX1 had more than 99% homology with several strains of *Lysinbacillus*. At the same time, the phylogenetic tree constructed by MEGA 11 software shows that the genetic distance between SX1 and *Lysinibacillus xylanilyticus strain WJ-11* (KC211302.1) is the closest, and they are located on the same branch of the phylogenetic tree (Figure 3.1 d). The 16SrDNA sequence analysis and phylogenetic tree analysis of SX1 strain revealed that the strain was *Lysinibacillus xylanilyticus*.

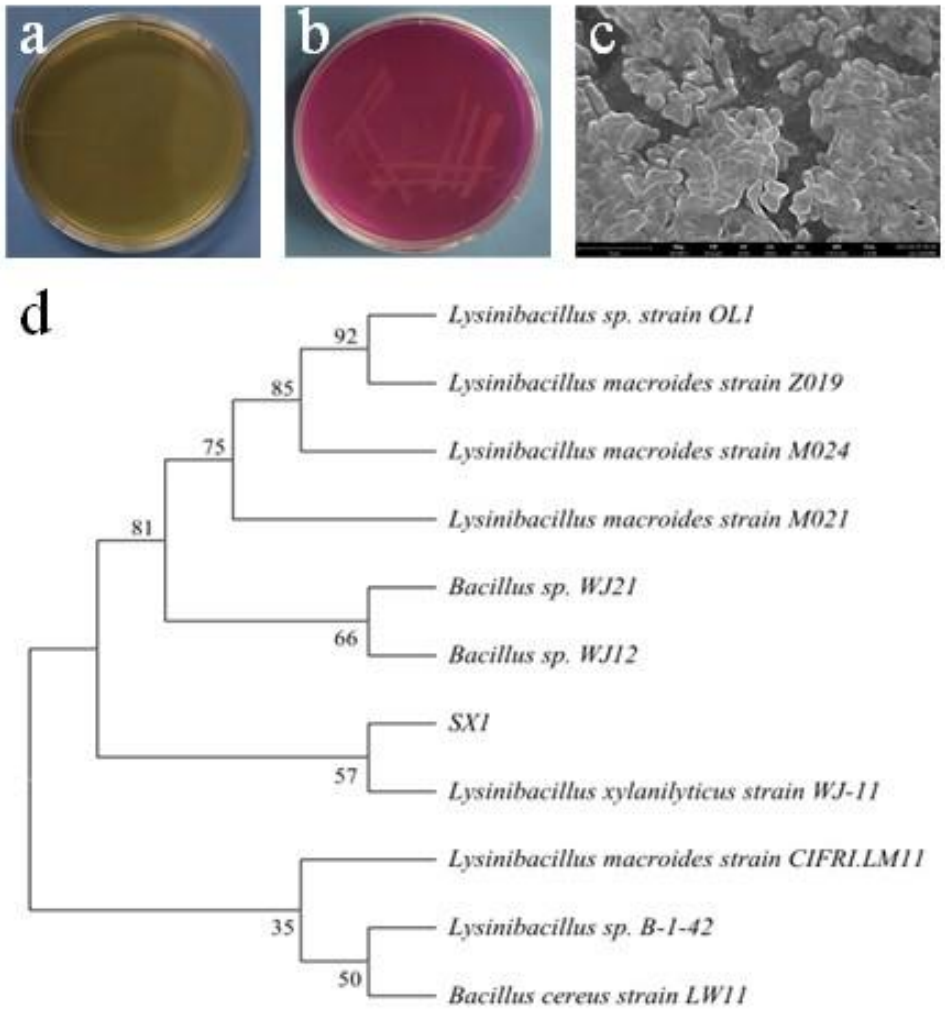

Figure. 3.1 (a) Phenol red plate medium without colonies, (b) Phenol red plate medium with strain SX1, and (c) micrograph of strain SX1, (d) Phylogenetic tree based on 16SrRNA gene sequence of SX1 and its related species.

3.3.2 Isolation and identification of strain SX1

It is widely acknowledged, YE is rich in nutrients, including carbohydrates, fatty acids, proteins, amino acids, peptides, vitamins, and trace elements, which can provide essential nutrients for the growth of microorganisms [43, 44]. Our research further validates this point. As shown in Figure 3.2 a, the SX1 strain failed to grow and reproduce in the absence of YE in the culture medium, indicating that-even with glucose supplied as a carbon source-YE is still required to provide critical nutrients such as amino acids, vitamins, and trace elements, which are indispensable for SX1 proliferation. In the range of 0 - 2.0 g/L, as the concentration of YE in the culture

medium escalates, the biomass of SX1 also augments. Interestingly, when the concentration of YE in the culture medium reaches 3.0 g/L, the growth of SX1 is inhibited again. This may be attributed to the imbalance of nutrient ratios such as carbon and nitrogen caused by excessive YE [45]. Therefore, an excessively elevated or decreased YE level in the medium is deleterious to SX1 strain proliferation.

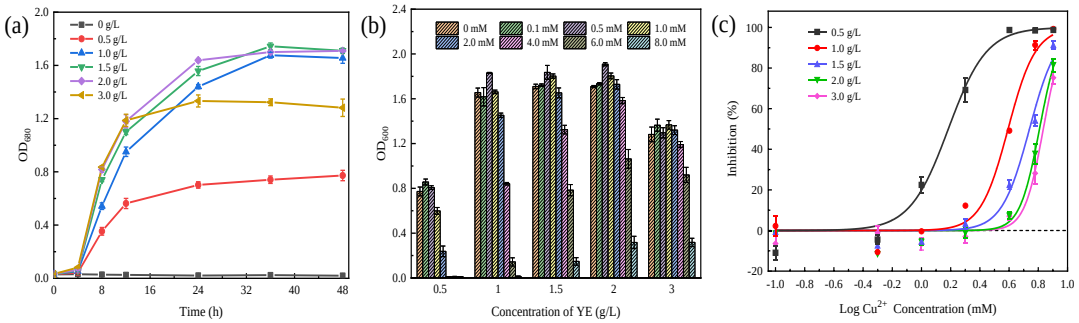

Figure 3.2 (a) SX1 growth curves at different YE concentrations, (b) The OD_{600} and (c) inhibition rate of SX1 after 48 h of culture with 0-8 mM Cu^{2+} added in 0.5-3.0 g/L YE concentration medium.

Having explored the impact of YE on SX1 growth, we now turn to investigate its effect on SX1's resistance to Cu^{2+} toxicity. We measured the OD_{600} of SX1 after 48 h of cultivation with Cu^{2+} in a certain concentration range in a culture medium containing 0.5 - 3.0 g/L YE. As can be seen from Figure 3.2 b, when the concentration of Cu^{2+} in the medium was low, the biomass of SX1 bacteria increased. This phenomenon is mainly because copper can participate in the synthesis of a variety of proteins in microbial cells, and then regulate cell metabolism and growth and development [35, 46]. However, when the concentration of Cu^{2+} in the medium rose excessively, the growth of SX1 strains in all experimental groups was inhibited to different degrees. This is because excessive Cu^{2+} will cause severe damage to the cell membrane structure of microorganisms and the key enzymes of metabolism [47]. The inhibitory curve and the corresponding semi-maximum inhibitory concentration (IC_{50}) can be obtained by fitting the data in Figure 3.2 b. As can be seen from Figure 3.2 c and Table 3.1, IC_{50} increases with the increase of YE concentration, indicating that YE can enhance SX1's resistance to copper toxicity.

The electron microscope shows that under different concentrations of YE cultivation, the morphology of SX1 was relatively regular and rod shaped, with no significant differences, indicating that changes in YE concentration had a relatively

small impact on the morphology of SX1 (Figure 3.3 a-e). When different YE concentration groups were exposed to 5 mM Cu^{2+} simultaneously, obvious deformation of SX1 strains was observed, and the lower the YE concentration, the more pronounced the morphological change (Figure 3.3 f-j), which further indicates that YE could reduce copper toxicity to SX1.

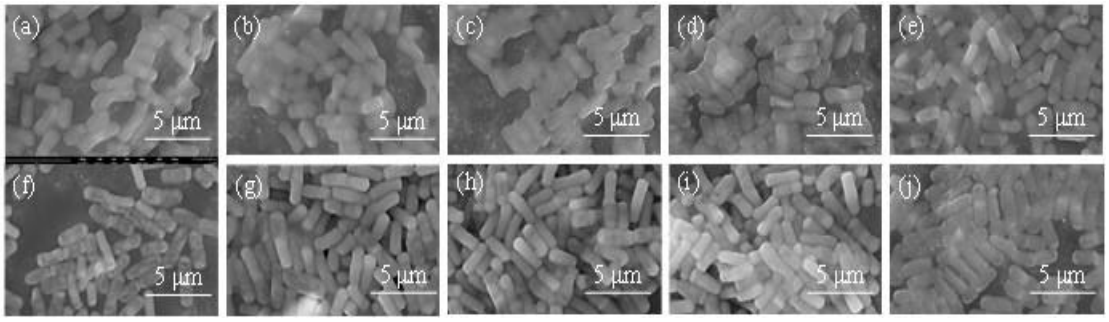

Figure 3.3 Morphology of SX1 cultured in medium containing (a) 0.5 g/L, (b) 1.0 g/L, (c) 1.5 g/L, (d) 2.0 g/L, (e) 3.0 g/L YE for 48 h; (f-j) The morphology corresponding to after exposure to 5 mM Cu^{2+}.

Table 3.1 Toxicity analysis of Cu(II) at different YE concentrations.

Concentration of YE (g/L)	IC_{50} (mM)	IC_{50} (95% CI)	Regression curve	R^2
0.5	1.526	1.402-1.660	y=100/(1+10^((0.1837-x) *3.305))	0.9844
1.0	3.917	3.612-4.171	y=100/(1+10^((0.5930-x) *4.620))	0.9812
1.5	5.491	5.214-5.767	y=100/(1+10^((0.7396-x) *4.574))	0.9754
2.0	6.429	6.185-6.674	y=100/(1+10^((0.8082-x) *6.450))	0.9683
3.0	6.827	6.602-7.060	y=100/(1+10^((0.8343-x) *6.827))	0.9673

3.3.3 Effect of YE on Cu^{2+} removal by MICP

As illustrated in Figure 3.4 a, Cu^{2+} removal efficiency exhibited pronounced dependence on YE concentration over a 48-hour treatment period. At 0.5 g/L YE,

negligible removal (<1%) was observed, attributable to Cu^{2+} toxicity overwhelming bacterial viability under nutrient-limited conditions. In contrast, increasing YE concentrations to 1.0 - 3.0 g/L yielded progressively lower removal efficiencies: 62.8% (1.0 g/L), 44.4% (1.5 g/L), 26.3% (2.0 g/L), and 6.8% (3.0 g/L). A robust inverse correlation ($R^2 = 0.98$) between YE concentration and Cu^{2+} removal was confirmed by linear regression (Figure 3.4 e), demonstrating that YE concentration dictates the trade-off between microbial resilience and Cu^{2+} removal rate. Optimal remediation occurred at intermediate YE concentrations (1.0 - 1.5 g/L), where nutritional support and metal complexation reached a critical equilibrium. Subsequently, the precipitation mass produced after 48 h of treatment at different YE concentrations was measured (Figure 3.4 b). At a YE concentration of 0.5 g/L, almost no precipitation is produced, indicating that Cu^{2+} cannot form a mineralized precipitate when SX1 does not grow. Within the concentration range of 1.0 - 3.0 g/L YE, the lower the YE concentration, the higher the precipitation mass, further confirming the direct impact of YE concentration on the efficacy of MICP in Cu^{2+} removal.

Figure 3.4 c illustrates the temporal evolution of urease activity under varying YE concentrations. Urease activity increased substantially with higher YE supplementation. For instance, after 48 hours, activity reached 17.25, 34.93, 40.79, and 39.92 at 1.0, 1.5, 2.0, and 3.0 g/L YE, respectively, while remaining minimal (0.005) at 0.5 g/L YE due to limited microbial growth. Notably, even at 3.0 g/L YE-where biomass declined-urease activity remained high, suggesting that factors beyond biomass, such as nutrient-induced metabolic activation or stress response, contributed to enhanced urease expression. This elevated enzymatic activity confirms that the low Cu^{2+} removal efficiency observed at high YE concentrations was not caused by insufficient urease availability. After analyzing the urease activity, we now focus on the NH_4^+-N concentration in the solution. The evolution of NH_4^+-N concentration over time in solutions at different YE concentrations was measured (Figure 3.4 d). It is evident that, similar to the trend in urease activity, NH_4^+-N concentration increases with increasing YE concentration. After 48 h of treatment, NH_4^+-N concentrations in the 0.5, 1.0, 1.5, 2.0, and 3.0 g/L YE concentration groups reached 0.15, 11.49, 18.49, 19.12, and 20.20 mM, respectively. Interestingly, unlike the actual measured NH_4^+-N concentration, the theoretical NH_4^+-N concentrations calculated based on urea decomposition are 0.19, 14.98, 24.40, 29.16, and 31.08 mM (Figure 3.4 f), respectively. This disparity is attributed to three factors. First, part of the NH_4^+-N is assimilated by microorganisms

as a nitrogen source. Second, elevated NH_4^+-N concentrations can increase pH (Figure 3.4 b), promoting the conversion of NH_4^+ to NH_3 and its subsequent volatilization (Eq. 12). Third, a fraction of NH_4^+-N may form stable copper-ammonia complexes, which cannot be detected by the Nessler's reagent method due to their strong coordination stability. In addition, at a concentration of 1.5 - 3.0 g/L YE, the NH_4^+-N concentration and pH value are relatively close, but there is a significant difference in Cu^{2+} removal rate, indicating that the formation of copper ammonia complexes may not be the main reason for the low Cu^{2+} removal rate [28].

$$NH_4^+ + OH^- \leftrightarrow NH_3 \uparrow + H_2O \quad (12)$$

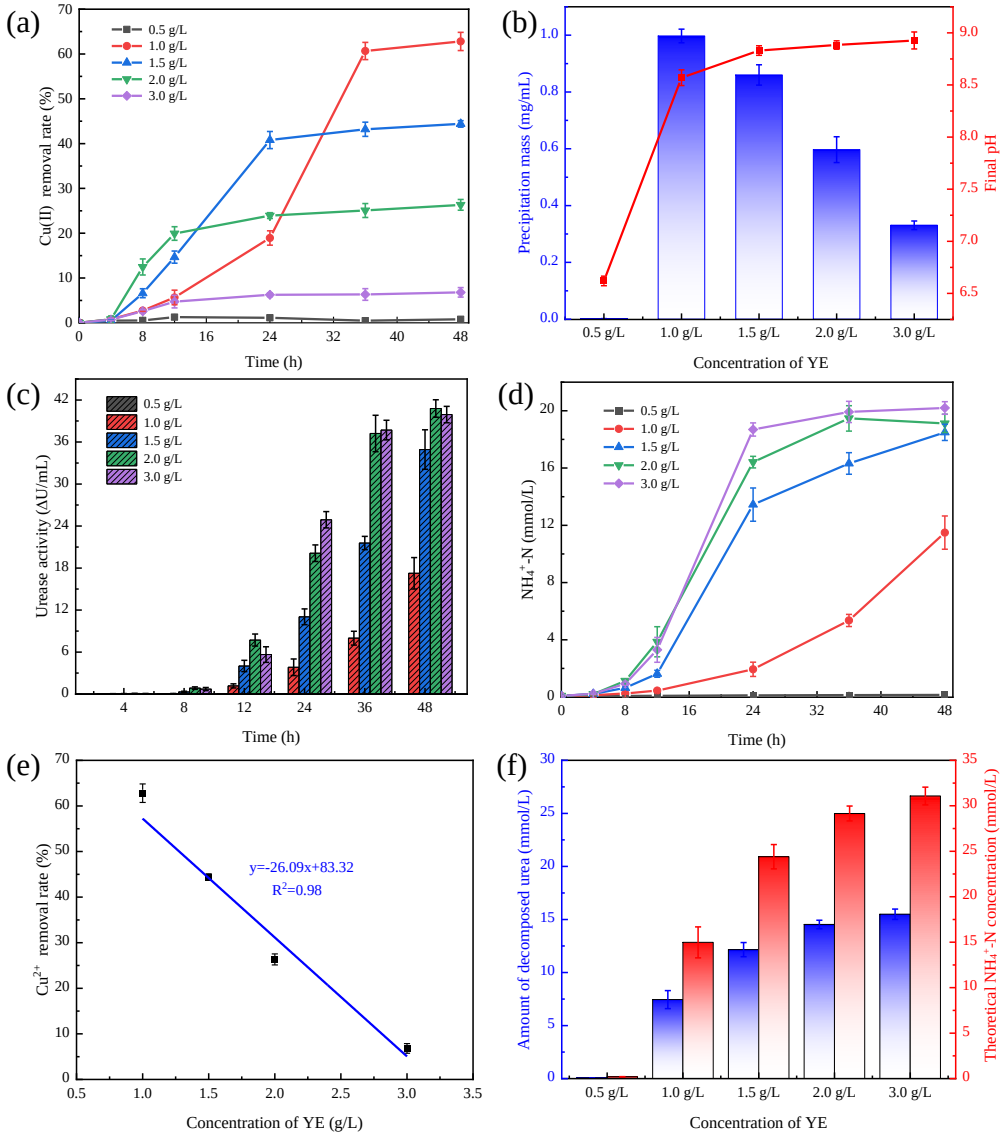

Figure 3.4 (a) The removal rate of Cu^{2+} under different YE concentrations; (b) Precipitation mass and pH after 48 h of treatment; (c) Urease activity versus treatment

time relationship; (d) NH4+-N concentration versus treatment time relationship; (e) The change in Cu^{2+} removal rate with YE concentration; (f) The amount of decomposed urea and theoretical NH4+-N concentration after 48 h of treatment. (Conditions: Initial Cu^{2+} concentration 5 mM, Initial solution pH = 6, 30 ± 2℃).

3.3.4 Characterization of mineralized precipitates

Since almost no precipitation is collected at 0.5 g/L YE, only mineralized precipitates in the 1.0-3.0 g/L YE concentration range were characterized. SEM-EDS results are shown in Figure 3.5 and 3.6. Figure 3.5 g shows that at a concentration of 3.0 g/L YE, only the SX1 strain can be observed, and its surface is relatively smooth, indicating that little or no mineralized precipitate was generated under these conditions. Figure 3.5 c and 3.5 e show that granular precipitation can be observed at YE concentrations of 1.5 g/L and 2.0 g/L, indicating the occurrence of a mineralization reaction under these conditions. Additionally, the precipitate generated by the SX1 strain was distributed around it, suggesting that the extracellular polymeric substances (EPS) and bacterial cells may serve as nucleation sites for mineralized precipitates [48, 49]. Furthermore, no SX1 strain was observed at a concentration of 1.0 g/L YE, possibly because SX1 was encapsulated in a significant volume of mineralized precipitates (Figure 3.5 a) [50]. Elemental mapping of mineralized precipitates shows that the main elements include C, N, O, P, Cu, and Au, which are uniformly distributed on the precipitation surface (Figure 3.5 b, 3.5 d, 3.5 f, and 3.5 h). Among them, the Au comes from the conductive coating added during the pretreatment process. The presence of N further indicates that some NH_4^+-N in the solution is absorbed by SX1 and removed along with the precipitate. Moreover, according to the corresponding EDS spectra (Figure 3.6), at concentrations of 1.0, 1.5, 2.0, and 3.0 g/L YE, the Cu atomic ratios in the precipitate were 10.75%, 7.95%, 5.47%, and 0.68%, respectively, which is consistent with the trend of Cu^{2+} removal rate.

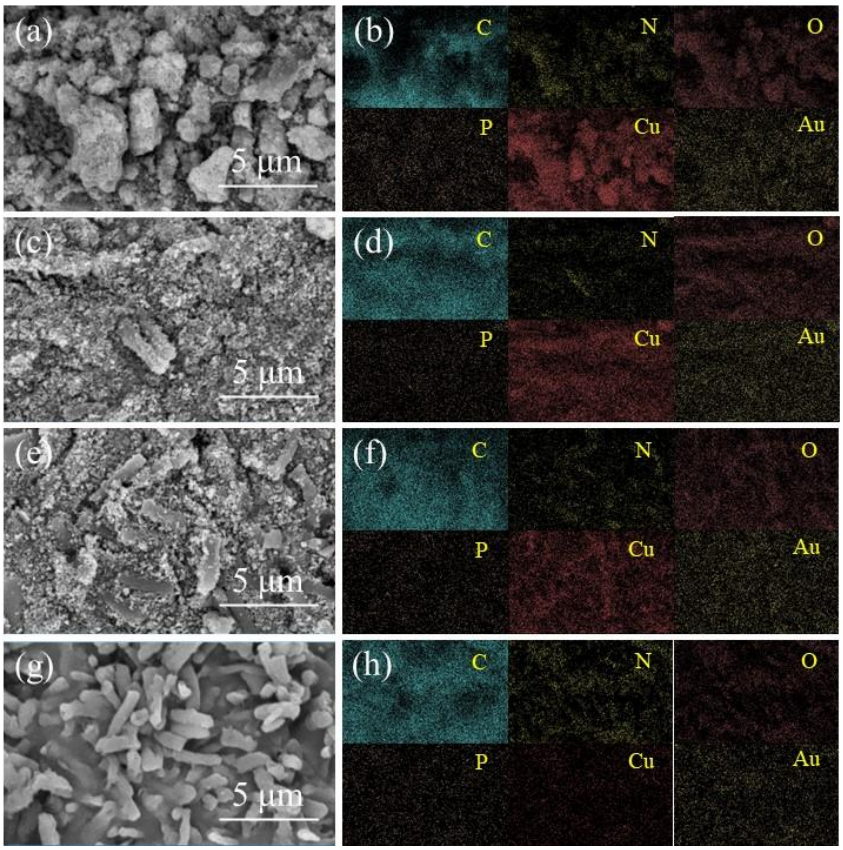

Figure 3.5 SEM images of mineralized precipitates at concentrations of (a) 1.0, (c) 1.5, (e) 2.0, and (g) 3.0 g/L YE; The elemental mapping of mineralized precipitates at concentrations of (b) 1.0, (d) 1.5, (f) 2.0, and (h) 3.0 g/L YE.

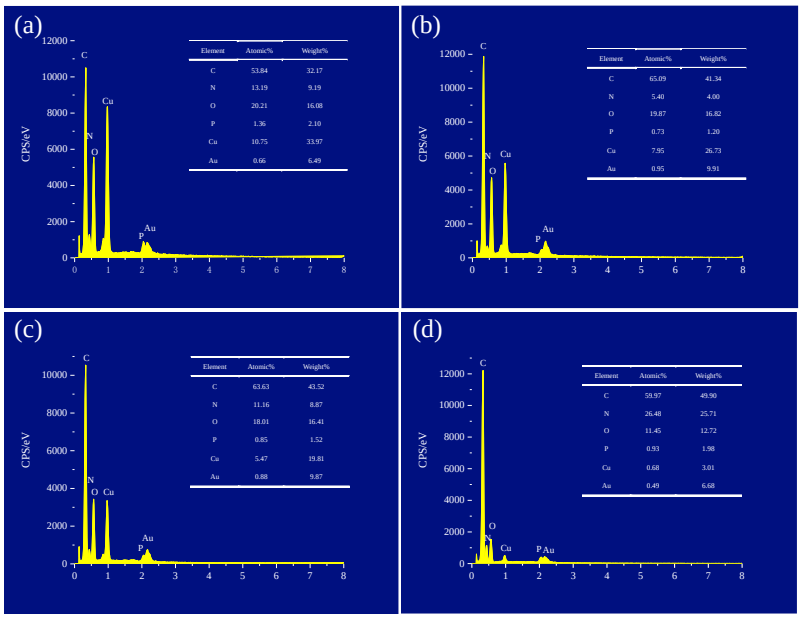

Figure 3.6 The corresponding EDS spectrum of (a) 1.0 g/L, (b) 1.5 g/L, (c) 2.0 g/L, (d) 3.0 g/L.

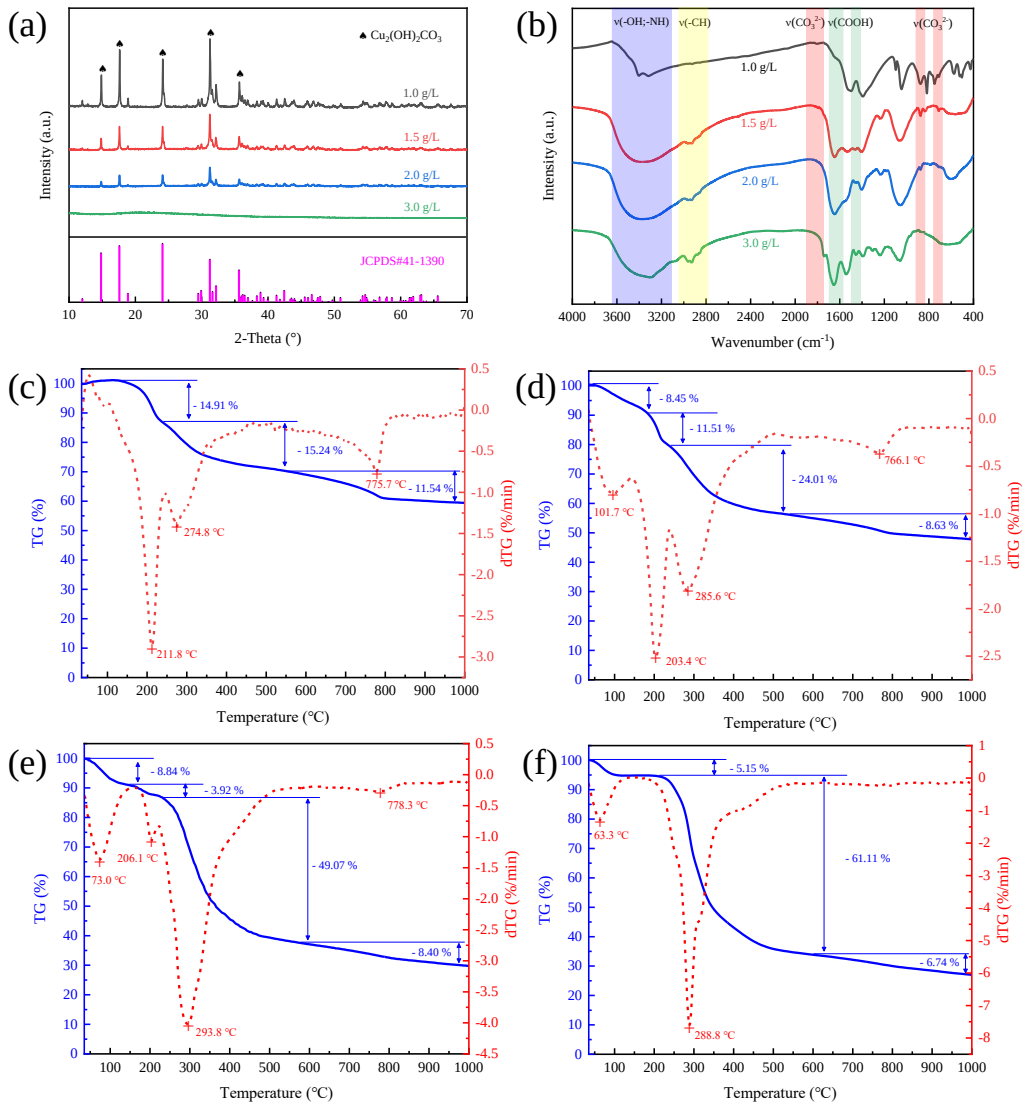

Figure 3.7 (a) XRD pattern and (b) FT-IR spectrum of mineralized precipitates; TG and dTG curves of mineralized precipitates under conditions of (c) 1.0, (d) 1.5, (e) 2.0, and (f) 3.0 g/L YE.

To further determine the crystal structure of mineralized precipitates, XRD was used for analysis. From Figure 3.7 a, it can be observed that the precipitates collected at 1.0, 1.5, and 2.0 g/L YE concentrations exhibit five characteristic peaks at 2θ = 14.8°, 17.5°, 24.1°, 31.3°, and 35.8°, which belong to the (020), (120), (220), (201), and (240) planes of $Cu_2(OH)_2CO_3$, respectively (JCPDS: 41-1390). This indicates that within the concentration range of 1.0-2.0 g/L YE, Cu^{2+} is mainly removed by carbonate precipitation ($Cu_2(OH)_2CO_3$). When the YE concentration reached 3.0 g/L, no significant characteristic peaks were observed. The reasons for this may be as follows: firstly, Cu^{2+} was mainly removed by adsorption rather than mineralization; secondly,

the number of mineralized products was below the detection limit of XRD or the mineralized products were amorphous structures. However, regardless of the above reasons, it indicates that the concentration of 3.0 g/L YE is not conducive to the removal of Cu^{2+} by MICP. The FT-IR spectrum of mineralized precipitates was shown in Figure 3.7 b. The broad peaks in the range of 3600-3200 cm^{-1} are attributed to the stretching vibration of hydroxyl (ν (-OH)) and amide (ν (-NH)) groups [51]. The characteristic peaks at 2929 cm^{-1} and 2876 cm^{-1} are attributed to the symmetric or asymmetric stretching vibrations of alkyl groups (ν ($-CH_2$) and ν ($-CH_3$)) in bacterial cells and extracellular polymers (EPS) [52]. The characteristic peaks at 1651 and 1455 cm^{-1} belong to the tensile vibrations of carboxyl groups (ν (COOH)) on the bacterial surface, which are reported to be the main binding sites for heavy metal ion adsorption and mineralization processes [15, 53]. As the YE concentration decreased (1.0-3.0 g/L), the characteristic peaks of alkyl and carboxyl groups belonging to EPS and SX1 bacterial cells gradually weakened and eventually disappeared, indicating that more mineralized precipitates are generated and occupy these nucleation sites at low YE concentrations. When the YE concentrations were 1.0, 1.5, and 2.0 g/L, the absorption peaks of the precipitate at 1809, 875, and 714 cm^{-1} suggest the presence of carbonate groups (ν (CO_3^{2-})) [54, 55]. In contrast, at a concentration of 3.0 g/L YE, there was no characteristic peak of carbonate groups, which is consistent with XRD results, further indicating that high YE concentrations limit Cu^{2+} removal by MICP.

The TG and dTG curves of mineralized precipitates are shown in Figure 3.7 c-f. The first weight loss was observed in the temperature range of 35-150 ℃, which corresponds to the removal of physically adsorbed water and low molecular weight hydrocarbons [56]. Near 210 ℃, weight loss was caused by the volatilization of carbon dioxide and water generated by the decomposition of $Cu_2(OH)_2CO_3$ (Eq. 13) [57]. It can be observed that at this stage, as the YE concentration increases (1.0-3.0 g/L), the weight loss gradually decreases (14.91%, 11.51%, 3.92%, and 0), further confirming that more $Cu_2(OH)_2CO_3$ precipitates can be obtained at low YE concentrations. The weight loss in the range of 250-500 ℃ was mainly attributed to the breakdown of proteins, lipids, and non-fibrous carbohydrates in bacterial cells and EPS [54]. When the temperature reaches 600 ℃, the weight loss mainly comes from two aspects: the slow further decomposition of microbial solid residues [56], and the deoxygenation reaction of CuO near 775 ℃ (Eq. 14) [58].

$$Cu_2(OH)_2CO_3 \rightarrow 2CuO + CO_2 \uparrow + H_2O \uparrow \quad (13)$$

$$4CuO \rightarrow 2Cu_2O + O_2 \uparrow \quad (14)$$

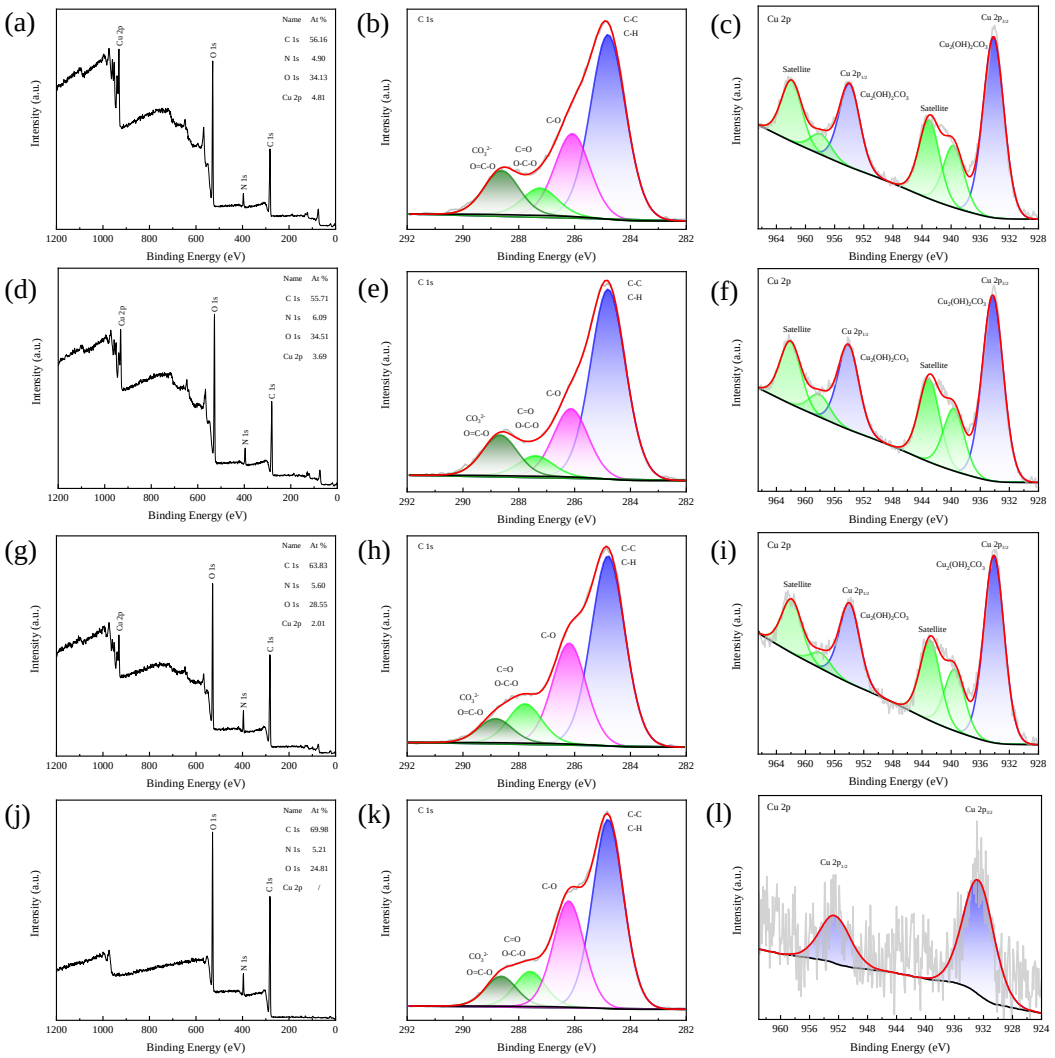

Figure 3.8 Extended XPS spectra of mineralization precipitation at different YE concentrations. (a) 1.0 - full spectrum, (b) 1.0 - C 1s, (c) 1.0 - Cu 2p, (d) 1.5 - full spectrum, (e) 1.5 - C 1s, (f) 1.5 - Cu 2p, (g) 2.0 - full spectrum, (h) 2.0 - C 1s, (i) 2.0 - Cu 2p, (j) 3.0 - full spectrum, (k) 3.0 - C 1s, and (l) 3.0 - Cu 2p.

The surface elemental chemical states of mineralized precipitates were analyzed using X-ray photoelectron spectroscopy (XPS). As can be seen from the full survey of XPS (Figure 3.8 a, d, g and j), the main elements of mineralized precipitates include C, O, N and Cu. At concentrations of 1.0-3.0 g/L YE, the atomic ratio of Cu showed a decreasing trend, which was consistent with the EDS results, further indicating that low YE concentrations were beneficial for Cu^{2+} removal. Deconvolution of the high-resolution C 1s spectrum revealed four distinct peaks at binding energies of 284.8 eV, 286.13 eV, 287.39 eV, and 288.67 eV (Figure 3.8 b, e, h and k). The peaks at 286.13 eV and 287.39 eV are assigned to C-O and C=O/O-C-O functional groups, respectively,

originating from organic constituents present in microbial cells and their extracellular polymeric substances [53]. The peak observed at 288.67 eV is primarily attributed to carbonate species (CO_3^{2-}) in $Cu_2(OH)_2CO_3$, since the carbon in carbonate (C^{4+}), being in a highly oxidized state, results in a significantly higher binding energy (~289 eV) due to strong electron binding compared to organic carbon. A minor contribution from O=C-O groups in carboxyl functionalities may also be present [59, 60]. Notably, as the YE concentration decreases, the relative area of the 288.67 eV peak increases, suggesting enhanced formation of carbonate precipitates under low-YE conditions. Within the concentration range of 1.0-2.0 g/L YE, the high-resolution spectrum of Cu 2p can be divided into six characteristic peaks (Figure 3.8 c, f and i). The binding energies of 939.66, 943.01, 957.91 and 961.91 eV belong to satellite peaks, which were caused by coupling between unpaired electrons in the atom or multi-electron excitation. The remaining two characteristic peaks (934.17 and 953.96 eV) correspond to Cu $2p_{3/2}$ and Cu $2p_{1/2}$ orbits of Cu^{2+} in $Cu_2(OH)_2CO_3$, respectively [61, 62]. Interestingly, when the YE concentration reaches 3.0 g/L, the high-resolution spectrum of Cu 2p can be decomposed into two weaker characteristic peaks (932.69 and 952.48 eV) corresponding to the Cu-O coordination bond, indicating that Cu^{2+} was mainly removed by adsorption under high YE concentration conditions [63]. The results of SEM-EDS, XRD, FT-IR, TG-dTG, and XPS indicate that Cu^{2+} was more easily removed by MICP pathway at low YE concentrations, forming $Cu_2(OH)_2CO_3$ precipitates.

3.3.5 Effect of YE on the speciation of Cu^{2+}

A UV-vis absorption spectrometer was used to conduct a full scan of YE with concentrations ranging from 0.5 to 3.0 g/L (Figure 3.9 a-b). It was observed that there was an obvious characteristic peak at 258 nm, which corresponded to the aromatic amino acids in proteins [64]. It is well - known that amino acids are typical organic ligands, which can form complexes with metal ions [65]. When a metal ion performs coordination with a ligand, the electron configuration of the metal ion's d orbital will be changed, resulting in color change. Therefore, the color change of solution can also be used as a means to judge the coordination [66]. It can be seen from Figure 3.9 c that in the concentration range of 0.1 to 8.0 mM, the individual Cu^{2+} have no absorption peak at 258 nm. Interestingly, when Cu^{2+} were added to YE solution, the absorption peak at 258 nm was significantly enhanced, and the color of the solution changed from yellow to blue-green, all of which indicated that Cu^{2+} had a coordination reaction with

YE (Figure 3.9 d-h). In addition, we used copper to titrate YE, and the increase in absorbance at 258 nm after titration was fitted. The results showed that high concentrations of YE tended to equilibrium later, indicating that as YE increased, the amount of complexed Cu^{2+} also increased (Figure 3.9 i).

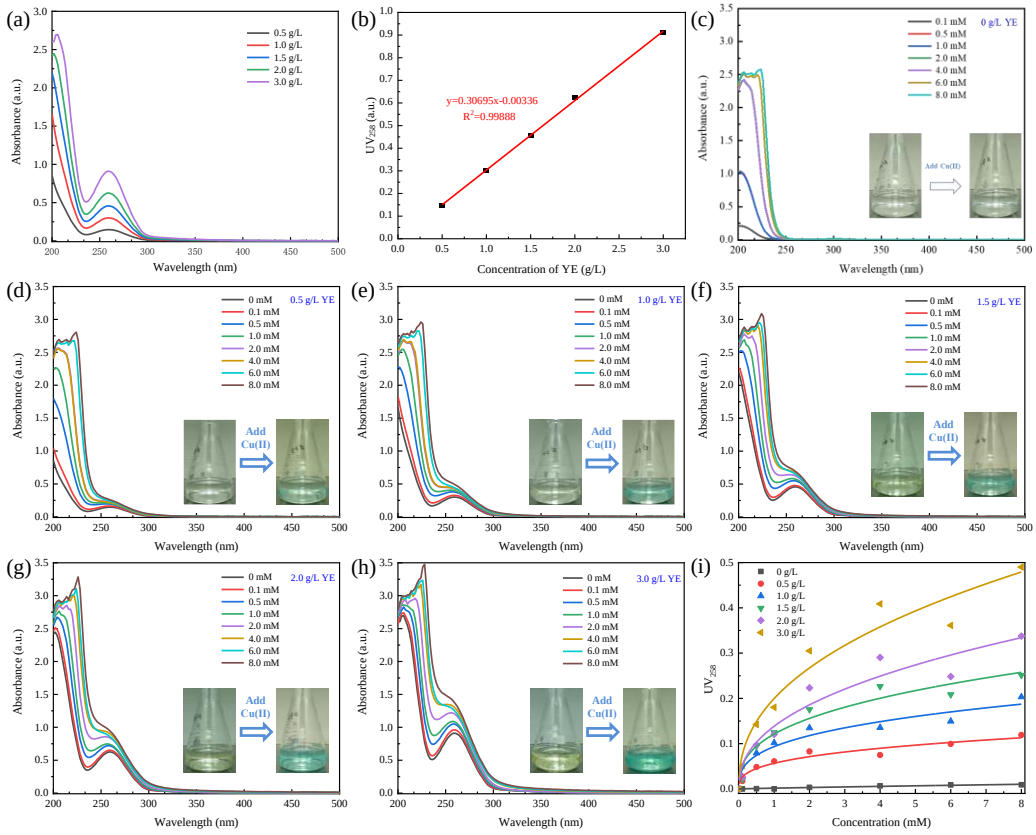

Figure 3.9 The (a) UV-vis absorbance of 0.5-3.0 g/L YE, and (b) the fitting of wavelength and YE concentration at 258nm. The Uv-vis absorbance of (c) 0, (d) 0.5, (e) 1.0, (f) 1.5, (g) 2.0, (h) 3.0 g/L YE reacting with different concentrations of Cu^{2+}, (i) The increase of absorbance at 258 nm after Cu^{2+} titration with different concentrations of YE.

To further determine the coordination strength of Cu^{2+} and YE, the competitive light exchange catalytic stripping voltammetry (CLE-ACSV) was used for analytical testing. As can be seen from Figure 3.10 a, the slope of copper titration curve decreases when YE is present, compared with the blank titration curve. And the higher the concentration of YE, the lower the slope, which indicates that YE and Cu^{2+} have a coordination reaction [32]. Next, we use the modified Langmuir equation (eq.11) to fit the titration data to estimate the conditional stability constant between copper and YE

[67]. The results are shown in Figure 3.10 b, and the corresponding parameters of the fitting equation are listed in Table 3.2. It can be found that with the increase of YE concentration, the number of ligands ($[YE]_T$) provided also increases. In addition, the conditional stability constant (K'_{CuYE}) of YE with Cu^{2+} reaches 1.2651×10^{10} - 1.78238×10^{10}, and it forms a very stable complex. This also explains why the presence of YE restricts the mineralization and precipitation of Cu^{2+}.

Table 3.2 Langmuir fitting equations and parameters for titration data.

Concentration of YE (g/L)	$[YE]_T$ (μM)	K'_{CuYE}	Regression curve	R^2
0.001	1.60389	1.60808×10^{10}	y=2.57918x/(1+1.60808x)	0.93523
0.002	3.61533	1.2651×10^{10}	y=4.57375x/(1+1.26510x)	0.96667
0.003	6.38260	1.78238×10^{10}	y=11.37622x/(1+1.78238x)	0.93058

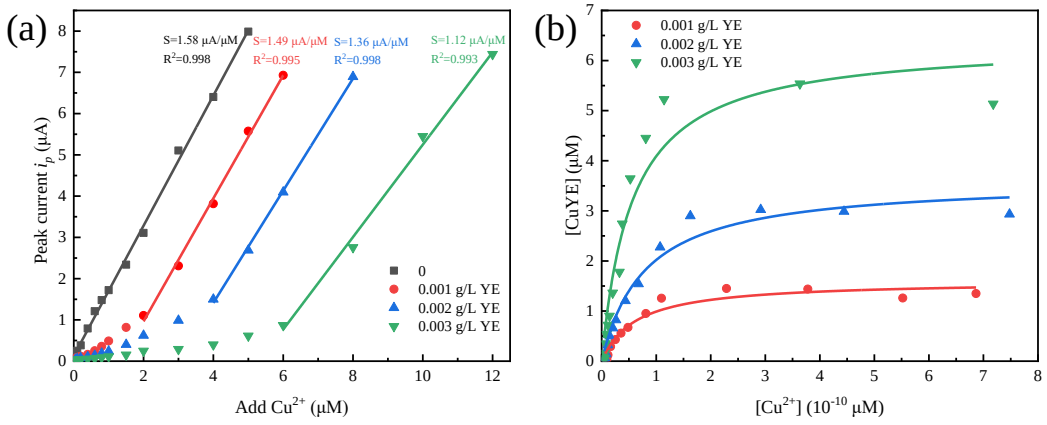

Figure 3.10 (a) Copper titration curves in the presence of different concentrations of YE (0-0.003 g/L) as indicated in the plot area, (b) Modified Langmuir fitting results of copper titration SA (50 μM).

3.4 Conclusions

In conclusion, this study investigated the role of yeast extract (YE) in the microbial induced carbonate precipitation (MICP) process for Cu^{2+} removal. The strain SX1, isolated from copper tailings and identified as *Lysinibacillus xylanilyticus*, showed high

copper tolerance and strong ureolytic activity. Results demonstrated that YE was crucial for SX1's growth and Cu^{2+} tolerance. At 0 - 2.0 g/L, SX1 biomass increased with YE concentration, while 3.0 g/L inhibited growth due to nutrient imbalance. YE also enhanced SX1's resistance to Cu^{2+} toxicity, with the IC_{50} of SX1 to Cu^{2+} rising as YE concentration increased. In the Cu^{2+} removal experiment, 0.5 g/L YE led to low growth and a Cu^{2+} removal rate < 1% due to copper toxicity. In the 1.0 - 3.0 g/L range, the removal rate declined from 62.8% at 1.0 g/L to 6.8% at 3.0 g/L. Analysis of mineralized products using SEM-EDS, XRD, FT-IR, TG-dTG, and XPS showed that at 1.0 - 2.0 g/L YE, Cu^{2+} was mainly removed by $Cu_2(OH)_2CO_3$ precipitation, but at 3.0 g/L, adsorption was dominant. UV-vis and CLE-ACSV analysis revealed a coordination reaction between YE and Cu^{2+}, with a high conditional stability constant ($K'_{CuYE} = 1.2651\times10^{10}$ - 1.78238×10^{10}), severely restricting copper ion mineralization and precipitation. These findings underscore the need to optimize organic nutrient levels in MICP applications. Future research should therefore explore alternative carbon/nitrogen sources with lower metal complexation capacity (e.g., glycerol or certain organic acids) and specific ligand competition strategies (e.g., pretreatment steps to remove complexing organics) to enhance the effectiveness of MICP in treating Cu^{2+}-contaminated environments.

References

[1] S. Meseldzija, J. Petrovic, A. Onjia, T. Volkov-Husovic, A. Nesic, N. Vukelic, Utilization of agro-industrial waste for removal of copper ions from aqueous solutions and mining-wastewater, J. Ind. Eng. Chem., 75 (2019) 246-252.

[2] Y. Xiao, L. Li, J.L. He, Y.X. Sun, Y. Lei, A metallurgical approach for separation and recovery of Cu, Cr, and Ni from electroplating sludge, Sci. Total Environ., 921 (2024).

[3] H. Ma, W. Xu, P. Wang, Y. Ding, S. Zhou, Adsorption of Cu (II) and Zn (II) in aqueous solution by modified bamboo charcoal, Environ. Geochem. Health, 46 (2024) 182.

[4] Z. Wang, J. Tan, C. Wu, L. Xia, S. Song, Improving soil properties and microbial communities in copper tailings using montmorillonite-based Chlorella gel beads, The Science of the total environment, 974 (2025) 179232.

[5] A.V. Waichman, G.S.D. Nunes, R. de Oliveira, I. López-Heras, A. Rico, Human health risks associated to trace elements and metals in commercial fish from the Brazilian Amazon, J. Environ. Sci., 148 (2025) 230-242.

[6] J.J. Hostynek, H.I. Maibach, Review: Skin irritation potential of copper compounds, Toxicol. Mech. Methods, 14 (2004) 205-213.
[7] L.R. Li, Y. Yi, X.W. Shu, J.H. Li, H. Kang, Y. Chang, The Correlation Between Serum Copper and Non-alcoholic Fatty Liver Disease in American Adults: an Analysis Based on NHANES 2011 to 2016, Biol. Trace Elem. Res., (2024).
[8] F.T. Kirk, D.E. Munk, E.S. Swenson, A.M. Quicquaro, M.H. Vendelbo, A. Larsen, M.L. Schilsky, P. Ott, T.D. Sandahl, Effects of tetrathiomolybdate on copper metabolism in healthy volunteers and in patients with Wilson disease, Journal of hepatology, 80 (2024) 586-595.
[9] G.J. Brewer, Risks of Copper and Iron Toxicity during Aging in Humans, Chem. Res. Toxicol., 23 (2010) 319-326.
[10] A. Azimi, A. Azari, M. Rezakazemi, M. Ansarpour, Removal of Heavy Metals from Industrial Wastewaters: A Review, ChemBioEng Rev., 4 (2017) 37-59.
[11] A.A.M. Alkhanjaf, S. Sharma, M. Sharma, R. Kumar, N.K. Arora, B. Kumar, A. Umar, S. Baskoutas, T.K. Mukherjee, Microbial strategies for copper pollution remediation: Mechanistic insights and recent advances, Environmental pollution (Barking, Essex : 1987), 346 (2024) 123588.
[12] Q.Y. Li, Y.F. Wang, Z. Chang, W. El Kolaly, F.L. Fan, M. Li, Progress in the treatment of copper(II)-containing wastewater and wastewater treatment systems based on combined technologies: A review, J. Water Process Eng., 58 (2024).
[13] M. Taharia, D. Dey, K. Das, U. Sukul, J.S. Chen, P. Banerjee, G. Dey, R.K. Sharma, P.Y. Lin, C.Y. Chen, Microbial induced carbonate precipitation for remediation of heavy metals, ions and radioactive elements: A comprehensive exploration of prospective applications in water and soil treatment, Ecotoxicology and Environmental Safety, 271 (2024).
[14] H. Lin, M.Y. Zhou, B. Li, Y.B. Dong, Mechanisms, application advances and future perspectives of microbial-induced heavy metal precipitation: A review, Int. Biodeterior. Biodegrad., 178 (2023).
[15] J.Q. Tan, H. Yi, Z.J. Zhang, D.L. Meng, Y.T. Li, L. Xia, S.X. Song, L. Wu, R.M.T. Sáncheze, M.E. Farías, Montmorillonite facilitated Pb(II) biomineralization by Chlorella sorokiniana FK in soil, J. Hazard. Mater., 423 (2022).
[16] C.Y. Lin, A.V. Turchyn, Z. Steiner, P. Bots, G.I. Lampronti, N.J. Tosca, The role of microbial sulfate reduction in calcium carbonate polymorph selection, Geochim. Cosmochim. Acta, 237 (2018) 184-204.

[17] W.B. Lin, W. Lin, X.H. Cheng, G.Z. Chen, Y.C. Ersan, Microbially Induced Desaturation and Carbonate Precipitation through Denitrification: A Review, Appl. Sci.-Basel, 11 (2021).

[18] Z. Wang, W.L. Xue, J.Q. Tan, F. Wang, J.H. Wang, L. Xia, X.H. Hu, S.X. Song, Sustainable remediation of Pb(II) from wastewater using gel bead of sodium alginate-living Chlorella sorokiniana FK-montmorillonite, International Journal of Biological Macromolecules, 317 (2025).

[19] X. Hu, C. Yu, X. Li, J. Zou, Y. Du, D.M. Paterson, Biomineralization of heavy metals based on urea transport and hydrolysis within a new bacterial isolate, B. intermedia TSBOI, J. Hazard. Mater., 469 (2024) 134049.

[20] L. Vaskevicius, V. Malunavicius, M. Jankunec, E. Lastauskiene, M. Talaikis, L. Mikoliunaite, A. Maneikis, R. Gudiukaite, Insights in MICP dynamics in urease-positive Staphylococcus sp. H6 and Sporosarcina pasteurii bacterium, Environ. Res., 234 (2023).

[21] M. Seifan, A. Berenjian, Microbially induced calcium carbonate precipitation: a widespread phenomenon in the biological world, Appl. Microbiol. Biotechnol., 103 (2019) 4693-4708.

[22] A.E. Torres-Aravena, C. Duarte-Nass, L. Azócar, R. Mella-Herrera, M. Rivas, D. Jeison, Can Microbially Induced Calcite Precipitation (MICP) through a Ureolytic Pathway Be Successfully Applied for Removing Heavy Metals from Wastewaters?, Crystals, 8 (2018).

[23] A. Kumar, H.W. Song, S. Mishra, W. Zhang, Y.L. Zhang, Q.R. Zhang, Z.G. Yu, Application of microbial-induced carbonate precipitation (MICP) techniques to remove heavy metal in the natural environment: A critical review, Chemosphere, 318 (2023).

[24] Y.-X. Xie, W.-C. Cheng, Z.-F. Xue, M.M. Rahman, L. Wang, Deterioration phenomenon of Pb-contaminated aqueous solution remediation and enhancement mechanism of nano-hydroxyapatite-assisted biomineralization, Journal of Hazardous Materials, 470 (2024).

[25] L. Wang, W.C. Cheng, Z.F. Xue, M.M. Rahman, Y.X. Xie, W.L. Hu, Immobilizing lead and copper in aqueous solution using microbial- and enzyme-induced carbonate precipitation, Front. Bioeng. Biotechnol., 11 (2023).

[26] S. Sepúlveda, C. Duarte-Nass, M. Rivas, L. Azócar, A. Ramírez, J. Toledo-Alarcón, L. Gutiérrez, D. Jeison, A. Torres-Aravena, Testing the Capacity of Staphylococcus equorum for Calcium and Copper Removal through MICP Process, Minerals, 11 (2021).

[27] M. Li, X.H. Cheng, H.X. Guo, Heavy metal removal by biomineralization of urease producing bacteria isolated from soil, Int. Biodeterior. Biodegrad., 76 (2013) 81-85.

[28] C. Duarte-Nass, K. Rebolledo, T. Valenzuela, M. Kopp, D. Jeison, M. Rivas, L. Azócar, A. Torres-Aravena, G. Ciudad, Application of microbe-induced carbonate precipitation for copper removal from copper-enriched waters: Challenges to future industrial application, J. Environ. Manage., 256 (2020).

[29] Z. Liu, X. Wu, T. Gao, M. Zhang, X. Min, W. Chen, C.-J. Tang, Rapid monitoring of heavy metal-ammonia complexes in solutions by UV-vis/ATR-FTIR spectroscopy and chemometric models, Chemical Engineering Journal, 481 (2024).

[30] X.X. Li, Y. Wang, J.J. Tang, K.K. Li, Removal Behavior of Heavy Metals from Aqueous Solutions via Microbially Induced Carbonate Precipitation Driven by Acclimatized Sporosarcina pasteurii, Appl. Sci.-Basel, 12 (2022).

[31] X.S. Huang, R.J. Zhang, Y.D. Xu, J.J. Zheng, Immobilization of Cd2+in an aqueous environment using a two-step microbial-induced carbonate precipitation method, J. Environ. Manage., 351 (2024).

[32] G. Gonzalez-Gil, S. Jansen, M.H. Zandvoort, H.P. van Leeuwen, Effect of yeast extract on speciation and bioavailability of nickel and cobalt in anaerobic bioreactors, Biotechnol. Bioeng., 82 (2003) 134-142.

[33] I.V.N. Rathnayake, M. Megharaj, G.S.R. Krishnamurti, N.S. Bolan, R. Naidu, Heavy metal toxicity to bacteria - Are the existing growth media accurate enough to determine heavy metal toxicity?, Chemosphere, 90 (2013) 1195-1200.

[34] M.M. Bagy, H.M. el-Sharouny, A.A. el-Shanawany, Effect of pH and organic matter on the toxicity of heavy metals to growth of some fungi, Folia Microbiol., 36 (1991) 367-374.

[35] S.Y. Qiao, G.Q. Zeng, X.T. Wang, C.G. Dai, M.P. Sheng, Q. Chen, F. Xu, H. Xu, Multiple heavy metals immobilization based on microbially induced carbonate precipitation by ureolytic bacteria and the precipitation patterns exploration, Chemosphere, 274 (2021).

[36] Y.-X. Xie, W.-C. Cheng, Z.-F. Xue, L. Wang, M.M. Rahman, Degradation of naphthalene in aqueous solution using a microbial symbiotic system founded by degrading and ureolytic bacteria, Environmental Research, 268 (2025).

[37] Y.-X. Xie, W.-C. Cheng, Z.-F. Xue, L. Wang, P.-F. Zhang, Removal of naphthalene from aqueous solution using bacteria-loaded carrier materials, Separation and Purification Technology, 377 (2025).

[38] V. Achal, A. Mukherjee, P.C. Basu, M.S. Reddy, Lactose mother liquor as an alternative nutrient source for microbial concrete production by Sporosarcina pasteurii, Journal of Industrial Microbiology & Biotechnology, 36 (2009) 433-438.

[39] Y.X. Zhao, R. Shi, X.A.N. Bian, C. Zhou, Y.F. Zhao, S. Zhang, F. Wu, G.I.N. Waterhouse, L.Z. Wu, C.H. Tung, T.R. Zhang, Ammonia Detection Methods in Photocatalytic and Electrocatalytic Experiments: How to Improve the Reliability of NH3 Production Rates?, Adv. Sci., 6 (2019).

[40] W.H.M. Abdelraheem, M.K.M. Rabia, N.M. Ismail, Evaluation of copper speciation in the extract of Eichhornia crassipes using reverse and forward/CLE voltammetric titrations, Arabian J. Chem., 9 (2016) S1670-S1678.

[41] R. Wang, C.L. Chakrabarti, Copper speciation by competing ligand exchange method using differential pulse anodic stripping voltammetry with ethylenediaminetetraacetic acid (EDTA) as competing ligand, Anal. Chim. Acta, 614 (2008) 153-160.

[42] H. Waska, A. Koschinsky, T. Dittmar, Fe- and Cu-Complex Formation with Artificial Ligands Investigated by Ultra-High Resolution Fourier-Transform ion Cyclotron Resonance Mass Spectrometry (FT-ICR-MS): Implications for Natura Metal-Organic Complex Studies, Front. Mar. Sci., 3 (2016).

[43] D. Huynh, S.R. Kaschabek, M. Schloemann, Effect of inoculum history, growth substrates and yeast extract addition on inhibition of Sulfobacillus thermosulfidooxidans by NaCl, Res. Microbiol., 171 (2020) 252-259.

[44] L. Hakobyan, L. Gabrielyan, A. Trchounian, Yeast extract as an effective nitrogen source stimulating cell growth and enhancing hydrogen photoproduction by Rhodobacter sphaeroides strains from mineral springs, Int. J. Hydrogen Energy, 37 (2012) 6519-6526.

[45] R.W. Brown, D.R. Chadwick, G.D. Bending, C.D. Collins, H.L. Whelton, E. Daulton, J.A. Covington, I.D. Bull, D.L. Jones, Nutrient (C, N and P) enrichment induces significant changes in the soil metabolite profile and microbial carbon partitioning, Soil Biology & Biochemistry, 172 (2022).

[46] A.J. Mugwar, M.J. Harbottle, Toxicity effects on metal sequestration by microbially-induced carbonate precipitation, J. Hazard. Mater., 314 (2016) 237-248.

[47] M. Ali, X. Song, D. Ding, Q. Wang, Z.X. Zhang, Z.W. Tang, Bioremediation of PAHs and heavy metals co-contaminated soils: Challenges and enhancement strategies, Environ. Pollut., 295 (2022).
[48] J. He, X.Y. Chen, Q.Z. Zhang, V. Achal, More effective immobilization of divalent lead than hexavalent chromium through carbonate mineralization by Staphylococcus epidermidis HJ2, Int. Biodeterior. Biodegrad., 140 (2019) 67-71.
[49] X.J. Zhu, W.L. Li, L. Zhan, M.S. Huang, Q.Z. Zhang, V. Achal, The large-scale process of microbial carbonate precipitation for nickel remediation from an industrial soil, Environ. Pollut., 219 (2016) 149-155.
[50] X.S. Hu, C.H. Yu, J.S. Shi, B.H. He, X.R. Wang, Z.Z. Ma, Biomineralization mechanism and remediation of Cu, Pb and Zn by indigenous ureolytic bacteria B. intermedia TSBOI, J. Cleaner Prod., 436 (2024).
[51] L. Zhang, W.J. Wang, C.L. Yue, Y.B. Si, Biogenic calcium improved Cd2+and Pb2+immobilization in soil using the ureolytic bacteria Bacillus pasteurii, Sci. Total Environ., 921 (2024).
[52] Y. Zeng, Z.Z. Chen, Y.L. Du, Q.Y. Lyu, Z.Y. Yang, Y. Liu, Z.Y. Yan, Microbiologically induced calcite precipitation technology for mineralizing lead and cadmium in landfill leachate, J. Environ. Manage., 296 (2021).
[53] Z.J. Zhang, K.Q. Zhou, J.V. Garcia-Meza, S.X. Song, L. Xia, Montmorillonite enhances the remediation of lead (II) by polyvinyl alcohol/sodium alginate/Chlorella sorokiniana FK microcapsules, Applied Clay Science, 273 (2025).
[54] Y. Zeng, Z.Z. Chen, Q.Y. Lyu, X.X. Wang, Y.L. Du, C.C. Huan, Y. Liu, Z.Y. Yan, Mechanism of microbiologically induced calcite precipitation for cadmium mineralization, Sci. Total Environ., 852 (2022).
[55] X.Y. Qian, C.L. Fang, M.S. Huang, V. Achal, Characterization of fungal-mediated carbonate precipitation in the biomineralization of chromate and lead from an aqueous solution and soil, J. Cleaner Prod., 164 (2017) 198-208.
[56] S. Ceylan, D. Kazan, Pyrolysis kinetics and thermal characteristics of microalgae Nannochloropsis oculata and Tetraselmis sp, Bioresour. Technol., 187 (2015) 1-5.
[57] Z. Cao, H. Jia, Y.F. Zhou, M. Li, P.C. Xu, X.X. Li, D. Zheng, MEMS Resonant Cantilevers for High-Performance Thermogravimetric Analysis of Chemical Decomposition, Sensors, 23 (2023).

[58] J. Qu, X.M. He, M. Chen, H.M. Hu, Q.W. Zhang, X.Z. Liu, Mechanochemical synthesis of Cu-Al and methyl orange intercalated Cu-Al layered double hydroxides, Mater. Chem. Phys., 191 (2017) 173-180.
[59] Z.J. Zhang, Z. Wang, J.Q. Tan, K.Q. Zhou, J.V. Garcia-Meza, S.X. Song, L. Xia, Yeast-derived biochar to load CoFe2O4: Degradation of tetracycline hydrochloride by heterogeneous activation of peroxymonosulfate, J. Environ. Chem. Eng., 11 (2023).
[60] R.Z. Liu, D.W. Liu, J.L. Li, J.M. Li, Z.C. Liu, X.D. Jia, S.W. Yang, J.L. Li, S. Ning, Sulfidization mechanism in malachite flotation: A heterogeneous solid-liquid reaction that yields CuxSy phases grown on malachite, Miner. Eng., 154 (2020).
[61] Z. Li, N.N. Xiong, G.Z. Gu, Fabrication of a full-spectrum-response Cu2(OH)2CO3/g-C3N4 heterojunction catalyst with outstanding photocatalytic H2O2 production performance via a self-sacrificial method, Dalton Trans., 48 (2019) 182-189.
[62] H. Xu, D.S. Dai, S.S. Li, L. Ge, Y.Q. Gao, In situ synthesis of novel Cu2CO3(OH)2 decorated 2D TiO2 nanosheets with efficient photocatalytic H2 evolution activity, Dalton Trans., 47 (2018) 348-356.
[63] Z.H. Liu, Z.J. Chen, D.J. Zhang, B.J. Ni, Carboxyl and polyamine groups functionalized polyacrylonitrile fibers for efficient recovery of copper ions from solution, Environ. Sci. Pollut. Res., (2023).
[64] B.B. Amadeo, J. Pollet, W.H. Chen, U. Strych, P.J. Hotez, B.M. Elena, A method to probe protein structure from UV absorbance spectra, Anal. Biochem., 587 (2019).
[65] R.N. Collins, Separation of low-molecular mass organic acid-metal complexes by high-performance liquid chromatography, J. Chromatogr. A, 1059 (2004) 1-12.
[66] J. Han, Y.S. Chi, Vibrational and Electronic Spectroscopic Characterizations of Amino Acid-Metal Complexes, Journal of the Korean Society for Applied Biological Chemistry, 53 (2010) 821-825.
[67] K.N. Buck, K.W. Bruland, Copper speciation in San Francisco Bay: A novel approach using multiple analytical windows, Mar. Chem., 96 (2005) 185-198.

Chapter IV. Enhancing Microbial-Induced Carbonate Precipitation of Heavy Metals using Montmorillonite-Composite Microcapsules

4.1 Introduction

The rapid development of industrialization has brought enormous benefits, but it has also brought fatal damage to the ecological environment [1]. Industries such as mining, smelting, and electroplating have led to a significant increase in heavy metals entering the ecosystem [2-4]. These heavy metals have spread across water bodies and soils worldwide, posing a threat to the ecological balance [5, 6]. Among the various heavy metals, lead stands out as one of the most prevalent and hazardous, capable of causing irreversible damage to vital organs like the brain, kidneys, and nervous system, even at low levels of exposure [7-9]. Therefore, it is paramount to address the issue of lead pollution. Currently, lead remediation strategies encompass solvent extraction, chemical precipitation, electrolysis, ion exchange, and membrane separation [10-12]. Yet, these approaches frequently present challenges like high operational expenses, significant use of chemicals, and sludge by-products [13]. In comparison to the aforementioned technologies, microbial remediation technology has emerged as a promising avenue for lead remediation due to its economical and clean alternative [14].

Microalgae, as autotrophic microorganisms in ecosystems, are abundant in resources, have short growth cycles, and exhibit strong tolerance to heavy metals, making them powerful candidates for bioremediation of lead pollutants [15-17]. Related studies have shown that the surface of microalgae is rich in functional groups such as carboxyl, hydroxyl, carbonyl, and phosphate groups, which can bind to lead ions through various mechanisms such as electrostatic attraction, surface complexation, ion exchange, and surface precipitation [18-20]. In addition, microalgae can produce carbonic anhydrase to catalyze the conversion of CO2 and HCO3- during photosynthesis, thereby inducing carbonate precipitation of lead ions [21]. However, adverse external environments, such as extreme pH and high concentrations of pollutants, greatly hinder the metabolic activity of microalgae [22, 23]. Immobilized microbial technology can effectively resolve this predicament [24-26]. Through entrapment of microorganisms within a defined area via a carrier, we can boost the cell

concentration, thus enhancing microbial metabolism [27]. Moreover, microorganisms in the carrier are relatively unaffected by external environment fluctuations, mitigating negative influences from adverse environments on microbial activity [28].

Finding an ideal immobilized carrier is key to enhancing microbial performance [29]. Polyvinyl alcohol (PVA) and sodium alginate (SA) enjoy popularity as they're economical, exhibit superb biocompatibility and offer simplicity in gelling [30, 31]. Though, reliance solely on PVA and SA as embedding materials may fall short in providing adequate mechanical strength and protection abilities. Studies have shown that adding clay minerals to PVA-SA capsules can play a supporting role, thereby improving its mass transfer efficiency and stability [32, 33]. Montmorillonite (MMT) is a common clay mineral widely used as a fixed carrier for microorganisms due to its good biocompatibility, large specific surface area, and high ion exchange ability [34-36]. Reportedly, exchangeable ions of MMT with high cation exchange capacity can form cationic bridging ligands between MMT and microorganisms, thereby reducing lead stress on microorganisms [37]. Concurrently, the presence of MMT can promote the formation of biofilms, which further enhances the resistance of microorganisms to heavy metals and improves the fixation effect of heavy metals [38, 39]. Therefore, the inclusion of MMT in PVA-SA-microbial microcapsules could theoretically improve the repair of heavy metals. However, there haven't been any reports on MMT augmented PVA-SA-microalgae composite microcapsules for heavy metal remediation.

In this study, MMT was introduced into PVA/SA/Chlorella sorokiniana FK microcapsules and used for remediation of lead contamination in water and soil. The main objectives were to: (i) investigate the effects of the addition of MMT on the formation and physicochemical properties of microcapsules; (ii) explore the effects of important operating parameters (microcapsules dosage, initial pH and heavy metal concentration) on the lead remediation effect of microcapsules; (iii) reveal the mechanism of lead passivation by microcapsules by using scanning Fourier infrared Spectroscopy (FT-IR), X-Ray Diffraction (XRD), X-ray Photoelectron Spectroscopy (XPS), Scanning Electron Microscope-Energy Dispersive Spectrometer (SEM-EDS), Confocal Laser Scanning Microscope (CLSM) and other analytical techniques; (iv) explore the remedial effect of microcapsules on lead in soil and its influence on microbial community structure and function.

4.2 Materials and methods

4.2.1 Culture of microalgae

We used *Chlorella sorokiniana* FK, a phototrophic microalga particularly tolerant to lead, from lead-zinc mine tailings (Fankou, Shaoguan City, Guangdong Province) in our research [21]. *Chlorella* was grown in BG11 medium, comprising (per liter): 0.050 μg $CoCl_2 \cdot 6\ H_2O$, 0.079 μg $CuSO_4 \cdot 5H_2O$, 0.222 μg $ZnSO_4 \cdot 7\ H_2O$, 0.39 μg $NaMoO_4 \cdot 5H_2O$, 1.81 μg $MnCl_4 \cdot H_2O$, 2.86 μg H_3BO_3, 1 mg EDTA, 36 mg $CaCl_2 \cdot 2H_2O$, 40 mg K_2HPO_4, 300 mg $NaNO_3$, 6 mg ammonium ferric citrate, and 6 mg ammonium citrate monohydrate. Culturing was conducted under controlled conditions: 25 ± 2 ℃, 200 μmol/(proton·m^2·s) illumination with a 14/10h light-dark cycle.

4.2.2 Purification and sodium conversion of MMT

The MMT raw ore used in this paper was taken from Inner Mongolia Chifeng Ningcheng Tianyu Bentonite Technology Co., Ltd. Purification and sodification are required before use: prepare a 5% mass concentration MMT suspension, mechanically stir at 800 r/min for 8 h to fully hydrate and disperse MMT, then centrifuge at 1000 r/min for 1 min to remove impurities such as quartz and obtain the purified MMT suspension. Next, add 5% mass concentration of NaCl to the suspension, mechanically stir at 800 r/min for 12 h at 60 ℃, and centrifuge at 10000 r/min for 10 min to collect sediment. Finally, freeze-drying precipitation was used to obtain sodium modified montmorillonite for subsequent experiments.

4.2.3 Preparation of microcapsules

Microcapsules were mainly prepared according to previous studies [40-42], and the preparation process is shown in Figure 4.1. The specific steps were as follows: a certain amount of high-temperature sterilized MMT (0, 0.5, 1, 1.5, 2, 4 g) was added to 50 mL of a concentrated *Chlorella sorokiniana* FK suspension (OD_{680} = 1), followed by incubation in a light rotating oscillator (GXZ-380B/CHN) at 25 ℃ and 300 r/min for 24 h for pre-fixation. PVA (w/v, 8%) and SA (w/v, 1%) were used as crosslinking solutions, which were fully mixed with equal volumes of *Chlorella sorokiniana* FK suspension with/without MMT, and then the mixture was dropped into a solution containing 2% $CaCl_2$ using a pipette (the inner diameter of 0.45 cm) to form microcapsules, named PSC, $PSMC_{0.5}$, $PSMC_1$, $PSMC_{1.5}$, $PSMC_2$ and $PSMC_4$, respectively. After a 4-hour solidification period, the resultant microcapsules were

collected, gently rinsed thrice with deionized water, and respectfully stored in 0.9% sterilized normal saline for future usage, all operations respecting the utmost aseptic standards.

The mechanical strength of the capsules is characterized by observing deformation and elastic recovery. Briefly, ten capsules are selected and pressed with a 10 Newton weight and a glass slide for 10 min. The number of capsules that fail to recover is then recorded, and the deformation ratio is quantified using a digital caliper. *Chlorella sorokiniana* FK growth in microcapsules was assessed by measuring chlorophyll a change. After 7 days of microcapsule culture, 10 microcapsules were added to 5 mL acetone ethanol solution (v: v=1: 1) and crushed by cell crusher for 10 min. After intense vortex mixing for 2 min, the sample was immersed in darkness at 4 ℃ for 24 h, and the mixing was reversed several times during the process. The extracts were centrifuged at 4000 rpm for 10 min. After centrifugation, supernatant absorption was measured at 645 nm and 663 nm using acetone ethanol solution (v: v=1: 1) as blank control. And the change in chlorophyll a content was calculated according to equation (1), where *Chla* represents the content of chlorophyll a (mg/L) [43].

$$Chla = 12.7A_{663} - 2.69A_{645} \quad (1)$$

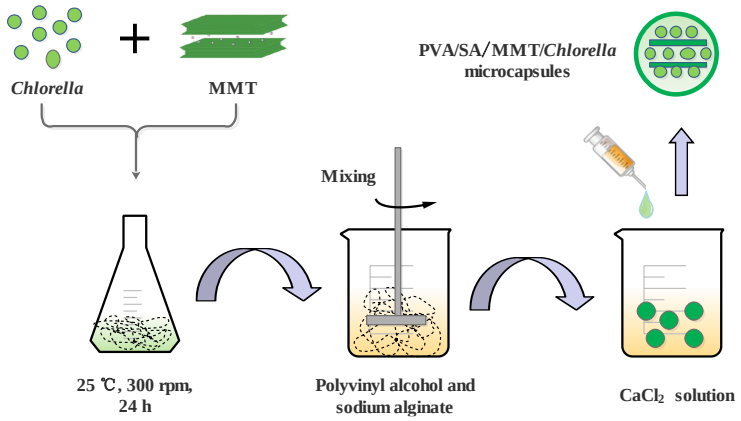

Figure 4.1 Preparation process of Chlorella microcapsules.

4.2.4 Removal of Pb(Ⅱ) by microcapsules

To evaluate the effect of MMT on the lead removal efficiency by microcapsules, a comparative experiment was carried out in a 250 mL sterilized conical flask with different amounts of MMT addition. The specific steps are: first add 100 mL of 200 mg/L lead solution in the conical flask, adjust the pH to 6, then add 2% microcapsules, and carry out the lead removal experiment in the light incubator. The pH of the solution

was measured after the reaction using a calibrated pH meter (METTLER TOLEDO/CH) to assess acidity changes. 72 h after the start of the experiment, the supernatant was taken and filtered by 0.22 μm filter head. Finally, the concentration of lead ions in the filtrate was determined by flame atomic absorption spectrometry (AAS, 240FS AA/USA).

To screen the optimal process conditions, diverse experimental parameters were examined with: initial pH of the solution: 2, 3, 4, 5, 6; Initial concentration of Pb(II): 50, 100, 200, 300, 400 mg/L; microcapsules dose: 0.5%, 1%, 1.5%, 2%, 3%. After the experiment began, samples were taken at fixed intervals (2, 4, 6, 8, 12, 24, 36, 48, 72 h), and the other steps were the same as described above. Each experiment was repeated three times. The pH of the solution was measured after the reaction using a calibrated pH meter (METTLER TOLEDO/CH) to assess acidity changes.

4.2.5 Characterization of microcapsules

Scanning Electron Microscope (SEM, TESCAN MIRA/CZ) equipped with Energy Dispersive Spectrometer (EDS) was introduced to analyze the microstructure and elemental distribution of samples. Prior to observation, a 5 nm gold layer was sputter-coated onto the samples to enhance conductivity, and the acceleration voltage was set to 15 kV during analysis. Each sample (PVA, SA, MMT, *Chlorella sorokiniana* FK, and microcapsules) was uniformly ground into a fine powder (particle size <45 μm) using an agate mortar and pestle to ensure homogeneity in particle size. The powdered samples were then loaded into a zero-background sample holder and gently compressed to create a smooth surface, which promoted random particle orientation [44]. Phase analysis was conducted using a powder X-ray diffractometer (XRD, D8 ADVANCE/GER) with Cu Kα radiation, with a scanning range of 2θ from 5° to 60°. Crystalline phases were identified by comparing the obtained diffraction patterns with reference data in the ICDD PDF-4 database. Fourier Transform Infrared Spectroscopy (FT-IR, NEXUS/USA) was utilized to identify functional groups of PVA, SA, MMT, *Chlorella sorokiniana* FK, and microcapsules. Surface zeta potential across varying pH was determined using a Malvern Zetasizer (Nano ZS90/UK). In order to understand the effect of lead exposure on the activity of algae inside microcapsules, we extracted algae cells from microcapsules using sterile syringes and observed them using confocal laser scanning microscopy (CLSM, Leica TCS SP5 II/CH) after staining with fluorescein diacetate and propidium iodide (FDA-PI). The changes in elemental chemical states of

microcapsules before and after reaction with lead were analyzed using X-ray photoelectron spectroscopy (XPS, ESCALAB 250Xi/USA).

4.2.6 Microcapsules remediation of simulated Pb-contaminated soil

The experimental soil was collected from an unpolluted site in Wuhan, Hubei. After air drying, the collected soil was crushed and sieved through a 2 mm sieve. Lead contaminated soil (500 mg/kg) was prepared with lead nitrate solution and placed in a constant temperature incubator at 28 ℃. Water was replenished on time to ensure a soil moisture content of about 20%. The soil was regularly turned over to ensure even distribution of lead, and aged for 3 months. Four experiments were performed in pot containing 200 g of lead-contaminated soil: (i) CK (control group), (ii) FC (free *Chlorella sorokiniana* FK, equivalent to the amount of immobilized *Chlorella sorokiniana* FK in $PSMC_2$ microcapsules), (iii) PSC (PSC microcapsules, 0.05 g/g soil), and (iv) $PSMC_2$ ($PSMC_2$ microcapsules, 0.05 g/g soil), all groups were added 1 mL/g inorganic salt medium, and 60% field water content was maintained. The occurrence form of lead was determined by the European Communities Bureau of Reference (BCR) fractionation extraction at 7 and 30 days after remediation [45].

4.2.7 Microbial community analysis

After 30 days of incubation, 3 soil samples were taken from each group for microbial community analysis. The specific steps are as follows: First, BSC48L1E-G (Bioer Technology/CHN) was used to extract soil microbial DNA. Then primers 806R (3'-GGACTACHVGGGTWTCTAAT-5') and 515F (3'-GTGCCAGCMGCCGGTAA-5') were used to amplify the hypervariable region (V4) of bacterial 16s rDNA gene. Finally, the amplicon was sequenced by PE250 (Illumina Nova 6000/USA).

4.3 Results and discussion

4.3.1 Effect of MMT content on microcapsules performance

A representative micrograph of the fabricated microcapsules is shown in Figure4.2. The microcapsules changed from translucent pale green (control group without MMT) to opaque yellowish-green (experimental group with MMT), which confirmed the successful incorporation of MMT. In addition, microcapsules without MMT showed considerable tailing phenomenon (Figure 4.2 a), whereas microcapsules containing MMT exhibited a uniform spherical shape (Figure 4.2 b-f), indicating that the

introduction of MMT was capable of stabilizing the microcapsule structure. Table 4.1 shows the performance differences of microcapsules with different MMT content. The inclusion of MMT significantly increased the compressive strength of microcapsules, mainly due to its capable support function which reduced the chain mobility of polymers [46, 47]. However, at elevated MMT concentrations (>4 g), predominant clay-clay interactions overshadowed polymer-clay interactions, causing aggregation and dispersion decline, which consequently diminished mechanical support [48]. The activity of *Chlorella sorokiniana* FK is directly related to the efficiency of its fixation of heavy metals [49]. Therefore, we evaluated the activity of *Chlorella sorokiniana* FK by measuring the change of chlorophyll a in microcapsules after 7 days of culture. It can be seen that when the dosage of MMT is 0.5-2 g, there is no significant change in chlorophyll a, indicating that MMT has good biocompatibility and will not inhibit microalgae growth. When the dosage of MMT was 4 g, the chlorophyll a of *Chlorella sorokiniana* FK decreased significantly, because a large amount of MMT on the one hand reduced the light transmittance of microcapsules, on the other hand blocked the pores of microcapsules, increased the mass transfer resistance of nutrients, and then affected the metabolic activity of *Chlorella sorokiniana* FK. In addition, the introduction of MMT significantly improved the lead removal efficiency of microcapsules, which was mainly attributed to the good adsorption performance of MMT for lead. When the addition of MMT was 2 g, the removal efficiency was the highest (89.66%), so $PSMC_2$ was selected for the subsequent test based on treatment cost and removal performance.

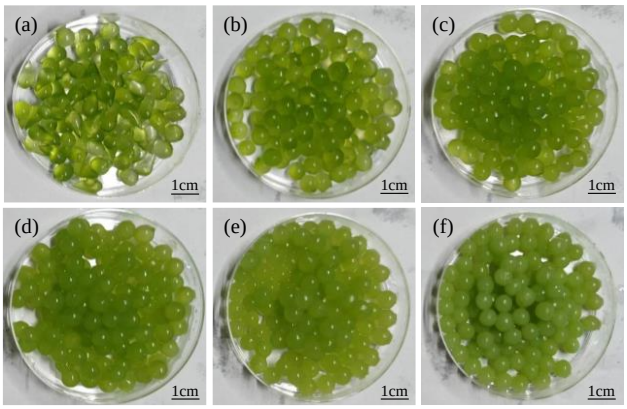

Figure 4.2 Appearance and morphology of Chlorella sorokiniana FK microcapsules with different MMT content. (a) PSC, (b) PSMC0.5, (c) PSMC1, (d) PSMC1.5, (e) PSMC2, (f) PSMC4.

Table 4.1 Comparison of microcapsule characteristics under different MMT content.

Microcapsules	Mechanical strength	Chlorophyll a (mg/L)	Removal rate of Pb(II) (%)
PSC	+	3.44	60.72
$PSMC_{0.5}$	++	3.31	63.25
$PSMC_1$	+++	3.58	76.83
$PSMC_{1.5}$	+++	3.25	80.17
$PSMC_2$	+++++	3.12	89.66
$PSMC_4$	++++	1.98	84.81

The micro-morphological characteristics of PSC and $PSMC_2$ are shown in Figure 4.3. The surface of PSC is smooth, whereas the addition of MMT to $PSMC_2$ gives it a rougher surface (Figure 4.3 a, c), which increases the specific surface area of the microcapsule wall, providing more adsorption sites for Pb(II) removal [25]. Moreover, the integrity of *Chlorella sorokiniana* FK cells within both microcapsules signifies remarkable biocompatibility of PVA, SA, and MMT (Figure 4.3 b, d), devoid of toxicity to *Chlorella sorokiniana* FK.

The FT-IR spectra of the raw materials and prepared microcapsules are shown in Figure 4.4 a. For *Chlorella sorokiniana* FK, the peaks of 1743 cm^{-1}, 1655 cm^{-1}, and 1076 cm^{-1} correspond to the absorption peaks of C=O for lipids, C=C stretching for amide-I peptides, and P=O stretching vibrations for phospholipids, respectively [50, 51]. The peaks at 2942 cm^{-1} in PVA belong to the typical C-H tensile vibration, and the peaks at 1420 cm^{-1} and 1614 cm^{-1} in SA correspond to the symmetric and antisymmetric tensile vibration of -COO-, respectively [52]. For MMT, the 3624 cm^{-1} peak is attributed to the tensile vibration of Al-OH. The peaks at 3443 cm^{-1} and 1639 cm^{-1} correspond to the tensile and bending vibrations of -OH within MMT layers. Moreover, a peak of 1035 cm^{-1} corresponds to the Si-O-Si tensile vibration [53]. The FT-IR spectra of PSC contain characteristic peaks of SA, PVA and *Chlorella sorokiniana* FK at the same time, confirming the successful formation of composite microcapsules. Compared to PSC, $PSMC_2$ exhibits MMT absorption peaks in the FT-IR spectra, and the -OH characteristic peaks widened and shifted in the range of 3000-3700 cm^{-1}, indicating MMT had hydrogen bonding interaction with SA, PVA and *Chlorella sorokiniana* FK [42, 54].

The crystal structures of the raw materials and prepared microcapsules were

further analyzed by XRD (Figure 4.4 b). *Chlorella sorokiniana* FK displayed a broad diffuse maximum centered at ~20° (2θ), indicative of amorphous biological material with no distinct crystalline phases. Pure PVA exhibits weak diffraction peaks at 2θ = 11.5°, 20.3°, 22.7°, and 40.5°, corresponding to the (100), (101), (200), and (220) crystallographic planes of PVA, respectively [55]. The SA molecule appears two peaks at 13.6° and 21.5°, which are caused by intramolecular hydrogen bonding [56, 57]. The diffraction peaks of pure MMT at 2θ = 7.1°, 19.8°, 28.7°, and 35.2° are attributed to reflections of (001), (020), (003), and (130), respectively [53]. In PSC, the characteristic peaks of PVA and SA disappeared, indicating that the interaction between SA and PVA molecules disrupted molecular orientation and hydrogen bonding, leading to a transition from a semi-crystalline to an amorphous structure [58]. $PSMC_2$ and MMT have similar characteristic peaks, indicating the successful introduction of MMT. In addition, the (001) peak reflecting the MMT layer spacing shifted from 7.1° to 5.8°, indicating that polymer chains intercalated into the interlayer space of MMT, expanding the d-spacing of the (001) plane. Based on these results, a mechanism for $PSMC_2$ formation is proposed, as shown in Figure 4.4 c, Ca^{2+} rapidly replaces Na^{+} in SA and binds to other SA molecules to form capsules, while MMT enhances the stability of the capsule by forming hydrogen bonds with adjacent hydroxyl groups on different SA and PVA chains.

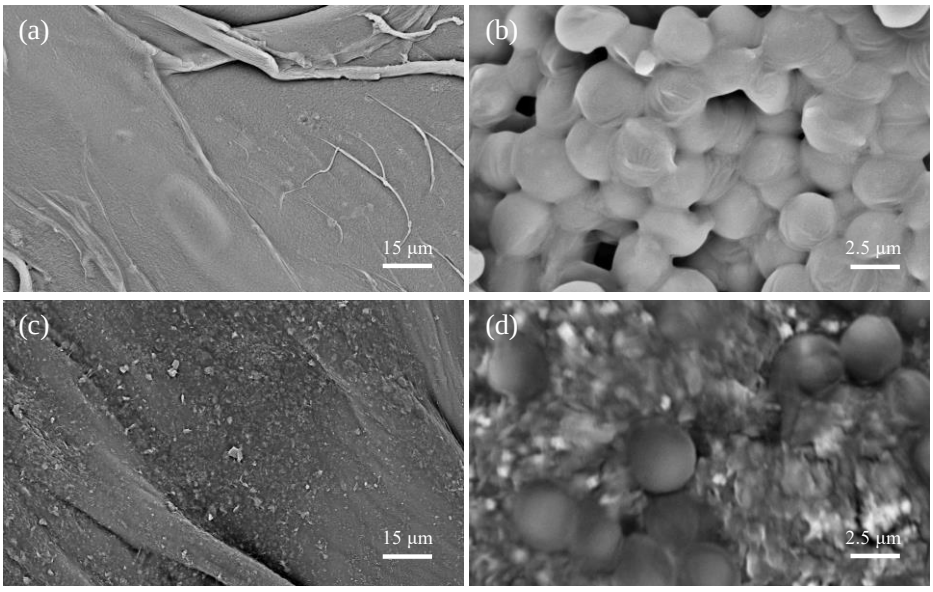

Figure 4.3 SEM images of PSC (a: surface, b: inner) and PSMC2 (c: surface, d: inner) microcapsules.

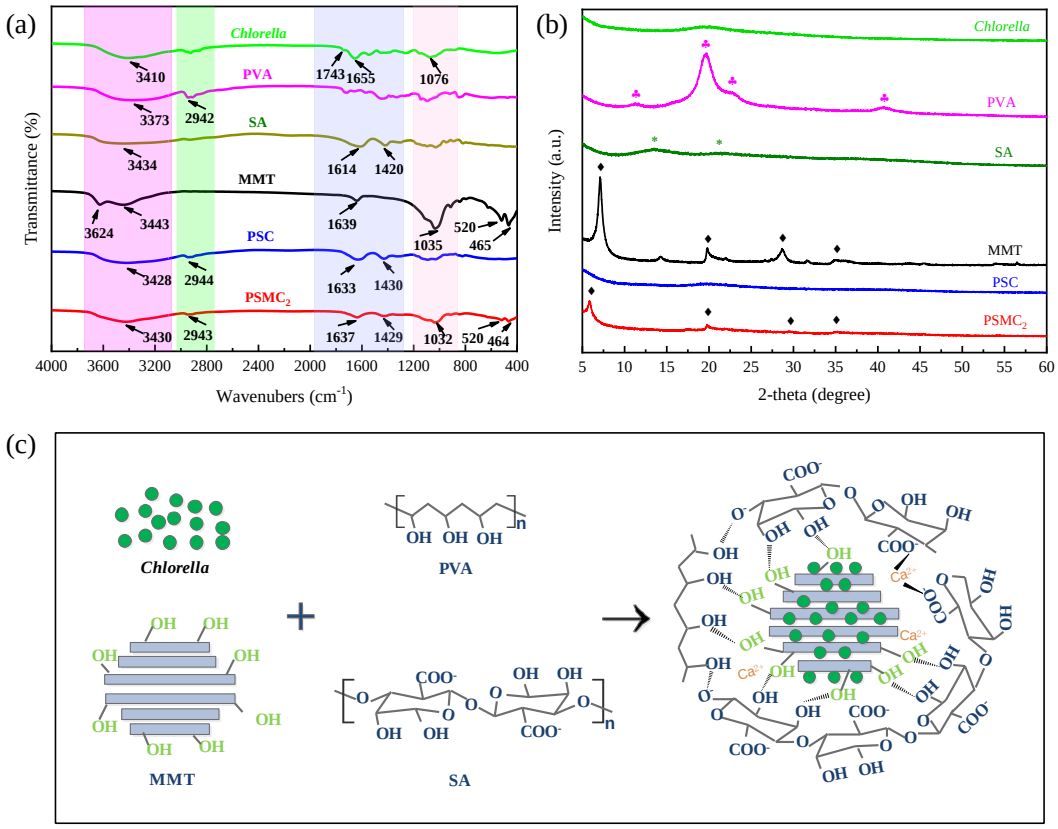

Figure 4.4 (a) FT-IR spectra and (b) XRD patterns of PVA, SA, MMT, Chlorella sorokiniana FK, PSC, and PSMC2. (c) Synthesis mechanism of PSMC2 microcapsules.

4.3.2 Effect of different factors on Pb(Ⅱ) removal

To comprehend the impact of varied factors on lead removal efficiency, we modified the initial solution pH, initial Pb(II) concentration, and microcapsules dosage for batch experiments. Considering that Pb(II) will form $Pb(OH)_2$ precipitation at pH > 6, which will affect experimental results, in order to ensure more rigorous and scientific experiments, we chose the initial solution pH range of 2 - 6 for exploration [59]. As shown in Figure 4.5 a, when the pH value increased from 2 to 6, the removal rate of Pb(II) by $PSMC_2$ microcapsules increased from 58.71% to 89.66%, indicating that the pH value of the solution had a significant impact on the removal of Pb(II). The influence of pH on the removability of Pb(II) can be elucidated in the following ways: Firstly, there is competitive adsorption between H^+ and Pb^{2+} under acidic environmental conditions [60, 61]. Consequently, as pH rises, there is a notable decrease in the concentration of competing protons, thus increasing the removal ability of Pb(II). Secondly, pH significantly affects the surface charge of $PSMC_2$ microcapsules and the morphology of Pb(II) in solution [62]. As shown in Figure 4.5 b, the surface charges of

$PSMC_2$ microcapsules at pH values of 2, 3, 4, 5, and 6, are -2.52, -6.81, -22.19, -29.78, and -32.02mV, respectively. On the other hand, according to the aqueous speciation analysis using Visual MINTEQ 4.0, under the pH conditions explored, the main species in Pb(II) solution is Pb^{2+} (Figure 4.6). Therefore, with the increase of pH, a strong electrostatic attraction occurs between the negatively charged $PSMC_2$ microcapsules and Pb^{2+}, thus increasing the removal rate of Pb(II). Considering the removal effect of Pb(II), further studies were carried out at pH 6.

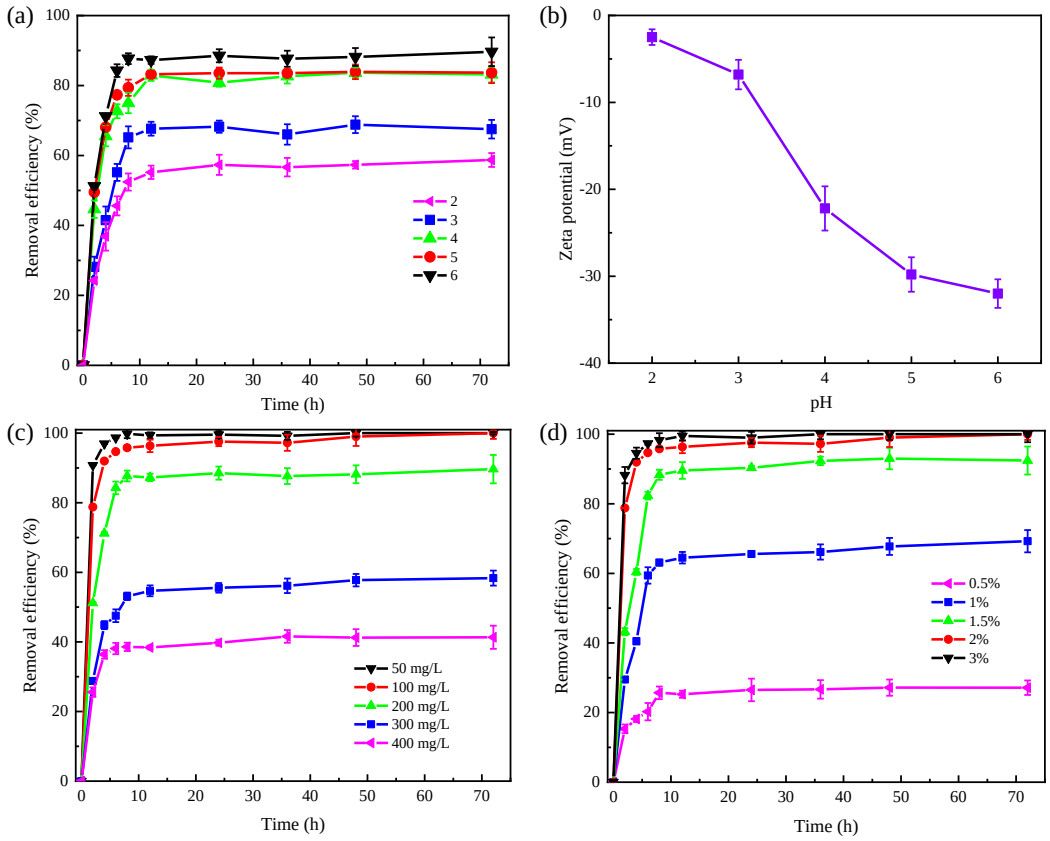

Figure 4.5 Removal efficiency of Pb(II) with the different (a) initial solution pH (Initial Pb(II) concentration 200 mg/L, solution pH range 2.0 to 6.0, microcapsules dosage 2%, 25 ± 2°C), (b) Zeta potential of PSMC2 microcapsules, (c) initial Pb(II) concentration (Initial Pb(II) concentration ranging from 50 to 400 mg/L, solution pH = 6, microcapsules dosage 2%, 25 ± 2°C) and (d) microcapsules dosage (Initial Pb(II) concentration 100 mg/L, solution pH = 6, microcapsules dosage ranging from 0.5% to 3%, 25 ± 2°C).

As shown in Figure 4.5 c, the removal efficiency was evaluated at different initial concentrations of Pb(II) from 50 mg/L to 400 mg/L. It can be observed that at lower

Pb(II) concentrations (<100 mg/L), the Pb(II) removal rate of $PSMC_2$ microcapsules remained at 100%. However, as the Pb(II) concentration increased, the removal efficiency of the microcapsules declined significantly. There are several possible explanations for this trend. Firstly, the adsorption site inside the $PSMC_2$ microcapsules is limited, and once the Pb(II) concentration surpasses a certain threshold, the microcapsules cannot entirely remove Pb(II). Secondly, it is also possible that the elevated concentration of Pb(II) suppresses the metabolic activity of microalgae, which then hampers their ability to bind and capture Pb(II). Based on the removal effect, the initial Pb(II) concentration of 100 mg/L was selected to continue the subsequent experiment.

The effect of $PSMC_2$ microcapsule dose on Pb(II) removal rate is shown in Figure 4.5 d. It is noteworthy that as the $PSMC_2$ microcapsule dose escalates, the removal rate of Pb(II) notably improves, as more microcapsules can provide more adsorption sites for lead. When the dose increased from 0.5% to 2%, the Pb(II) removal rate rose from 26.74% to 100%. In summary, when the initial pH value is 6, the initial Pb(II) concentration is 100 mg/L, and the microcapsule dose is 2%, the $PSMC_2$ microcapsules achieve a removal rate of 100% for Pb(II).

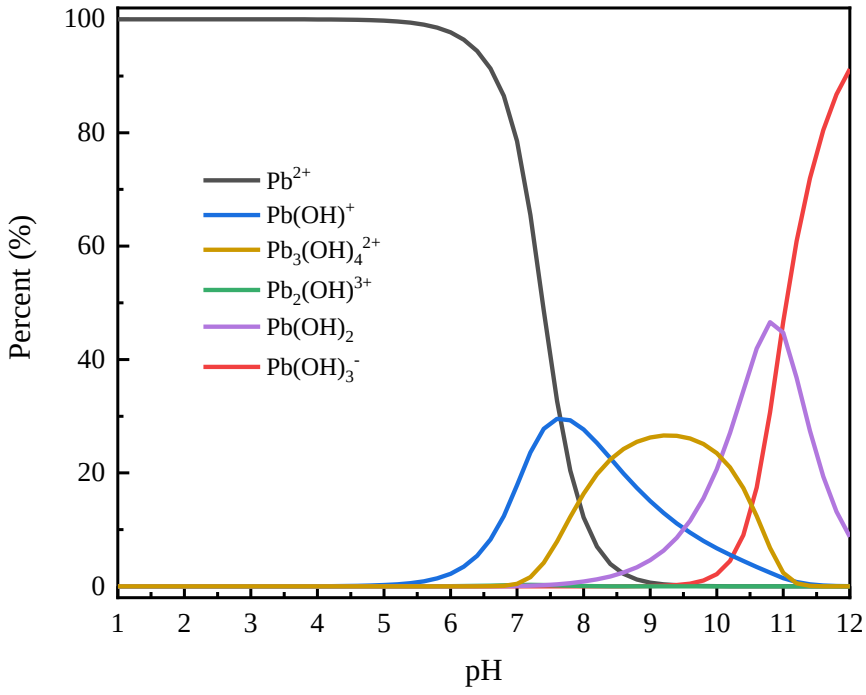

Figure 4.6 The existence form of Pb under different pH values calculated by Visual MINTEQ 4.0.

4.3.3 Mechanism of Pb(Ⅱ) removal by microcapsules

The surface and inner microstructure of microcapsules after reaction with Pb(II) were observed using SEM. Figure 4.7 a and e show the wall surface of PSC and $PSMC_2$ microcapsules after reaction with Pb(II), respectively. It can be seen that the wall structure morphology of PSC and $PSMC_2$ microcapsules has not changed significantly compared to that before reaction (Figure 4.3 a and c), indicating that both have excellent stability. Figure 4.7 b and 6f show the elemental composition mapping of PSC and $PSMC_2$ microcapsule walls after reacting with Pb(II), respectively. It can be seen that the main elements include C, O, Ca, and Pb, with the lead element uniformly dispersed on its surface, indicating that the outer wall of the microcapsule can play a role in adsorbing lead. Figure 4.7 c shows the inner morphology of PSC microcapsule after reaction with Pb(II). It can be observed that microalgae cells are surrounded by crystalline precipitates, and their cell structure is obviously deformed and broken. Combined with the corresponding EDS spectra (Figure 4.7 d), it can be seen that the crystalline precipitates are lead-bearing minerals, indicating that Pb(II) can pass through the outer wall of the PSC microcapsule and react with the microalgae inside to generate mineralized precipitates. In contrast, although some Pb(II) formed mineralization precipitation inside the $PSMC_2$ microcapsule through the outer wall (Figure 4.7 h), the microalgae inside the microcapsule still maintained a complete and regular spherical structure (Figure 4.7 g), indicating that the introduction of montmorillonite can effectively enhance the protective effect of microcapsules and reduce lead toxicity to microalgae.

To further determine whether PSC and $PSMC_2$ microcapsules can help microalgae resist the toxicity of Pb(II), microalgae inside microcapsules before and after the reaction with Pb(II) were stained, subsequently the activity of microalgae was observed under confocal laser scanning microscope (Figure 4.8). Figure 4.8 a-b show microalgae activity in PSC microcapsules before and after reaction with lead containing medium. It can be seen that after the reaction with lead, microalgae cells clustered and the fluorescence color changed from green to red, which means that a large number of microalgae died [63, 64]. In contrast, microalgae inside $PSMC_2$ microcapsules remained active and multiplied (Figure 4.8 c-d). This result is consistent with SEM observations, indicating that $PSMC_2$ microcapsules introduced with montmorillonite can better protect the internal microalgae.

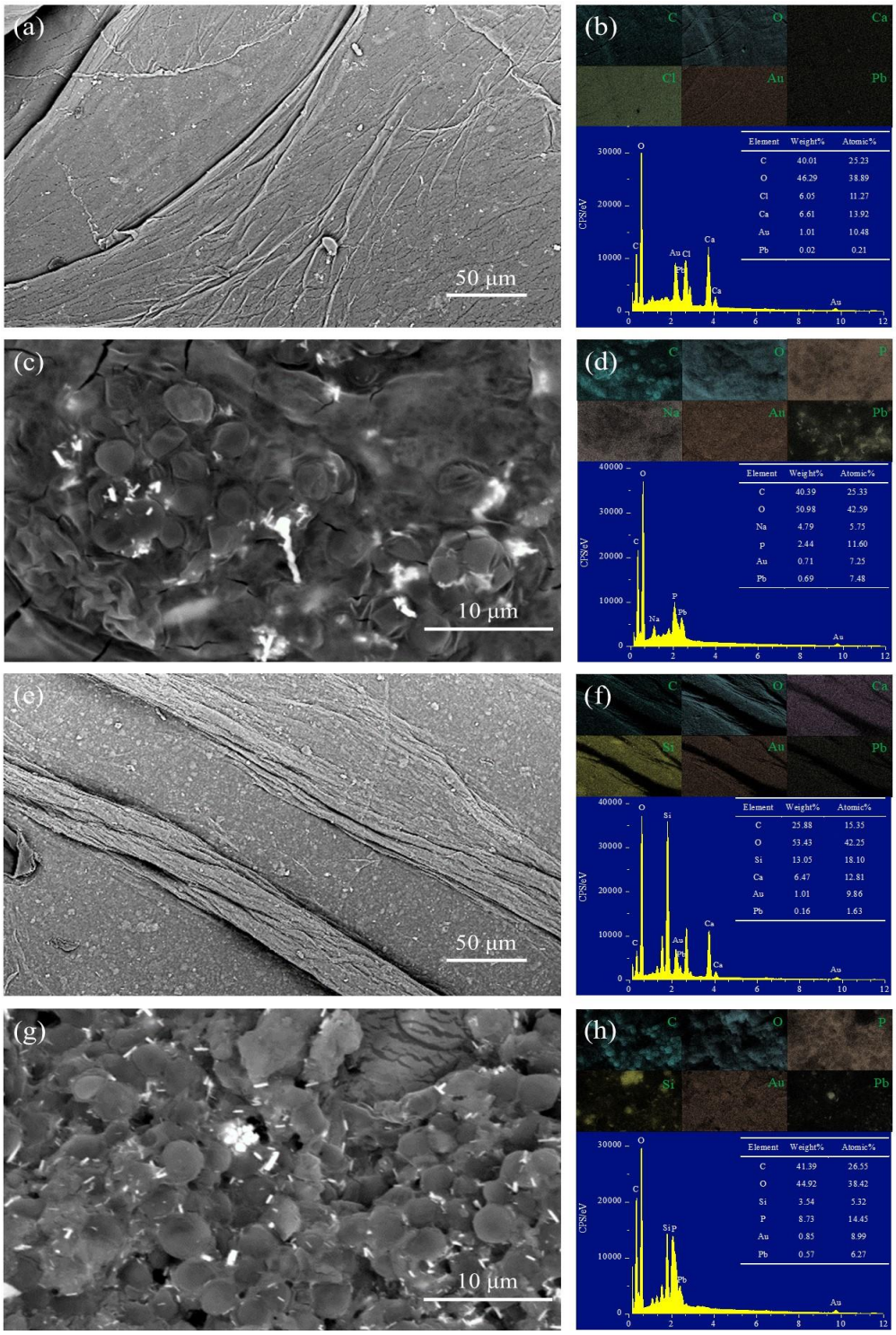

Figure 4.7 SEM images of (a) surface and (c) inner of PSC microcapsules after reaction with Pb(II), (b) surface and (c) inner EDS spectra of PSC microcapsules after reaction with Pb(II); SEM images of (e) surface and (f) inner of PSMC2 microcapsules after reaction with Pb(II), (g) surface and (h) inner EDS spectra of PSMC2 microcapsules after reaction with Pb(II).

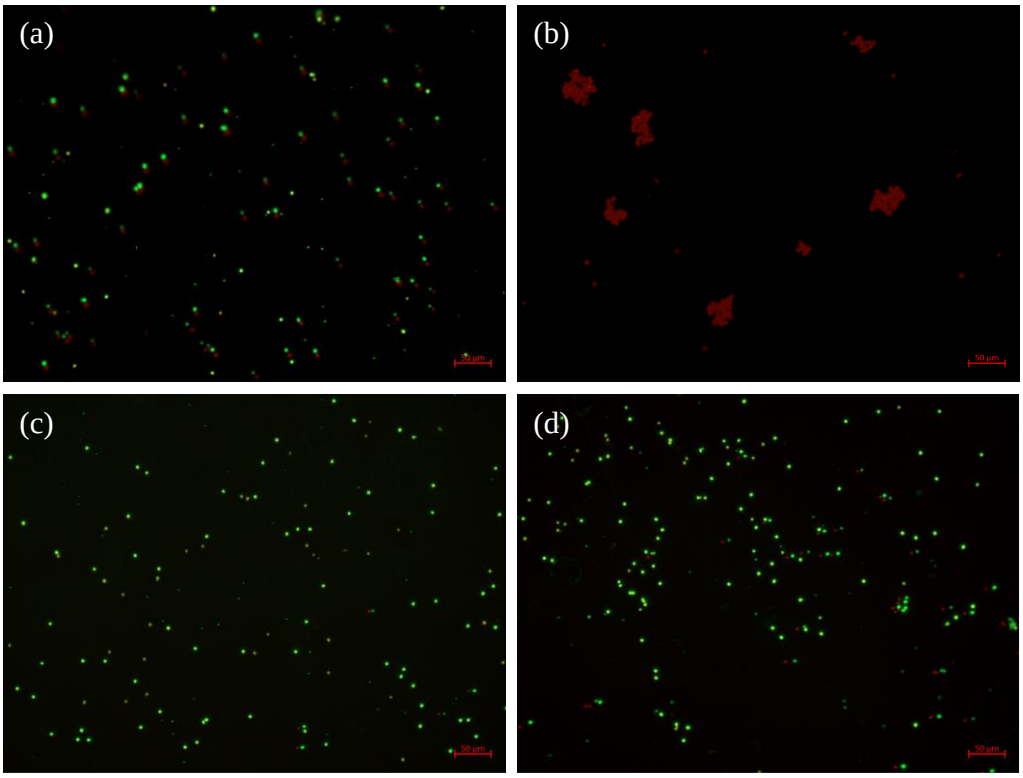

Figure 4.8 Internal CLSM images of PSC microcapsules (a) before and (b) after reaction with Pb(II); Internal CLSM images inside PSMC2 microcapsules (c) before and (d) after reaction with Pb(II).

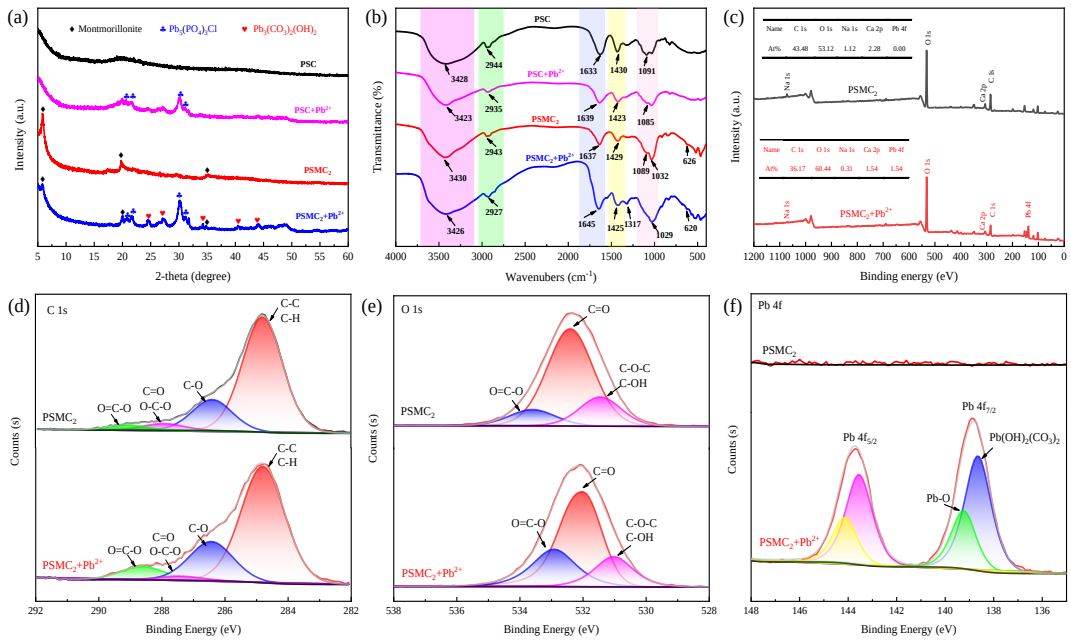

Figure 4.9 (a) FT-IR spectra and (b) XRD patterns of PSC and PSMC2 microcapsules before and after reaction with Pb(II); XPS spectra of PSMC2 microcapsules before and after reaction with Pb(II): (c) full spectrum, (d) C 1s, (e) O 1s, (f) Pb 4f.

To determine the types of lead containing precipitate produced by the reaction, PSC and $PSMC_2$ microcapsules before and after the reaction with Pb(II) were characterized by XRD. From Figure 4.9 a, it can be seen that after the reaction between PSC microcapsules and Pb(II), diffraction peaks of pyromorphite ($Pb_5(PO_4)_3Cl$) were observed at 2θ = 20.6°, 21.7°, 30.0°, and 31.1° [65], which may be attributed to the presence of abundant phosphate groups on the surface of microalgae, facilitating their surface precipitation with Pb^{2+} and generating stable phosphate precipitates [20, 66]. Similar to PSC microcapsules, $PSMC_2$ microcapsules also showed characteristic peaks of $Pb_5(PO_4)_3Cl$ after reacting with Pb(II). Interestingly, the $PSMC_2$ microcapsules exhibited distinctive spectral peaks at 2θ = 24.7°, 27.1°, 34.5°, 40.5°, and 44.1°, corresponding to hydrocerussite ($Pb_3(CO_3)_2(OH)_2$) [67]. This may be caused by the following reactions: Active microalgae employing carbonic anhydrase (CA) to catalyze the hydrolysis of carbon dioxide into bicarbonate (Eq. 2); subsequently, this bicarbonate could react with the complexed lead adhering to the microcapsule's surface, leading to the formation of a stable carbonate mineralization precipitate (Eq. 3) [68, 69]. Although mineralization reaction generates $4H^+$ (Eq. 3), the final solution pH only decreased slightly to 5.8 ± 0.2 (initial pH of 6.0), primarily due to the combined effects of the microcapsule matrix's buffering capacity and the photosynthetic activity of microalgae [21]. Montmorillonite in the matrix neutralizes localized H^+ through its cation exchange capacity and hydroxyl groups, while *Chlorella sorokiniana* FK consumes H^+ during the photosynthetic fixation of CO_2 (Eq. 2), driving the formation of HCO_3^- and promoting the precipitation of Pb^{2+} carbonates. This creates a feedback loop: photosynthesis supplies HCO_3^- for mineralization, and the resulting H^+ is buffered or recycled, maintaining a stable weakly acidic pH (5.8 ± 0.2). The synergy between the chemical buffering of montmorillonite and the biological H^+ utilization by microalgae highlights the critical role of pH and CO_2 dynamics in mediating efficient Pb^{2+} mineralization within the microcapsules.

$$CO_2(aq) + H_2O \leftrightharpoons HCO_3^- + H^+ \quad (2)$$

$$3Pb^{2+} + 2HCO_3^- + 2H_2O \rightarrow Pb_3(CO_3)_2(OH)_2 \downarrow + 4H^+ \quad (3)$$

FT-IR characterization technology can analyze the changes of functional groups on the surface of microcapsules, and help elucidate the immobilization and mineralization mechanism of Pb(II) on microcapsules. Figure 4.9 b shows the FT-IR spectra of PSC and $PSMC_2$ microcapsules before and after reaction with Pb(II). The wide peak at 3428 cm^{-1} of PSC microcapsules was attributed to the stretching vibration

of -OH, and the characteristic peak shifted to 3423 cm^{-1} after reacting with Pb(II), indicating that the hydroxyl group participated in the adsorption of Pb(II) [70]. The stretching vibration peaks attributed to -CH, C═C/C═O and -COO shift from 2944 cm^{-1}, 1633 cm^{-1} and 1430 cm^{-1} to 2935 cm^{-1}, 1643 cm^{-1} and 1423 cm^{-1}, respectively, indicating that -CH, C═C/C═O and -COO functional groups play an important role in the bonding interaction with Pb(II) [71, 72]. In addition, the characteristic peak representing the $-PO_4^{3-}$ functional group shifted from 1091 cm^{-1} to 1085 cm^{-1}, and the intensity decreased significantly, indicating that phosphate groups are also involved in Pb(II) binding [73, 74]. Compared with PSC microcapsules, the alterations in -OH, -CH, C=C/C=O, -COO and $-PO_4^{3-}$ functional groups before and after the reaction of $PSMC_2$ microcapsules with Pb(II) are similar. This indicates that these functional groups within $PSMC_2$ microcapsules play an instrumental role in the interaction with Pb(II). In addition, the characteristic peaks of Si-O-Si stretching at 1032 cm^{-1} and 626 cm^{-1} shifted to 1029 cm^{-1} and 620 cm^{-1}, suggesting that montmorillonite in $PSMC_2$ microcapsules interacts with Pb(II) through Si-OH functional groups [21]. It is worth noting that after reacting with Pb(II), a new characteristic peak appeared in the $PSMC_2$ microcapsules around 1317 cm^{-1}, attributed to the stretching of CO_3^{2-}, which is consistent with the conclusion of the formation of lead containing carbonate minerals in XRD [75]. In summary, these findings illustrate that the functional groups such as hydroxyl, carbonyl, carboxyl and phosphate within the microcapsule were all significantly involved in the binding of Pb^{2+}.

To further elucidate the mineralization mechanism of Pb(II), we investigated the XPS spectra of $PSMC_2$ microcapsules before and after reaction with Pb^{2+} (Figure 4.9 c-f). As can be seen from the full survey of XPS (Figure 4.9 c), the main elements of $PSMC_2$ microcapsules are C, O, Na and Ca. After the reaction with Pb(II), the characteristic peak of Pb 4f appears, while the atomic ratio (At%) of sodium and calcium decreases, indicating that calcium and sodium ions in the microcapsules have ion exchange with Pb(II). Figure 4.9 d shows the high-resolution spectrum of C 1s, with four peaks located near 284.8, 286.4, 287.9, and 289.1 eV after deconvolution, respectively assigned to the C atoms in the C-C/C-H, C-O, C=O/O-C-O, and O=C-O groups [76, 77]. After reacting with Pb(II), the characteristic peaks of the C=O/O-C-O and O=C-O groups shifted to 287.4 and 288.6 eV, respectively. This decrease in binding energy is a manifestation of electron migration to Pb(II), indicating that these functional groups are very important for Pb(II) binding [78]. Figure 4.9 e shows the three sub-

peaks of O 1s, which belong to C-O-C/C-OH (531.4eV), C=O (532.4eV) and O=C-O (533.6eV) [79]. After reacting with Pb(II), all three characteristic peaks shift in the direction of low binding energy (C-O-C/C-OH (531.1 eV), C=O (532.1 eV), and O=C-O (533.0 eV)), which indicates an increase in electron density around the oxygen atom and an increase in the coordination between the oxygen-containing group and Pb(II) [80]. Finally, as shown in Figure 4.9 f, lead on the surface of $PSMC_2$ microcapsules after reacting with Pb(II) exists in the form of Pb-O (139.2 eV) and $Pb_3(CO_3)_2(OH)_2$ (138.7 eV) [81]. The XPS results further support the XRD and FT-IR findings, confirming that both O-donor and C-donor functional groups are involved in binding Pb(II), thus promoting Pb(II) adsorption/precipitation.

Based on the above results, the mechanism of Pb(II) removal by $PSMC_2$ microcapsules can be proposed (Figure 4.10). The Pb(II) removal process mainly includes the following aspects: First, the negatively charged $PSMC_2$ microcapsules can enrich the positively charged Pb(II) on the surface of the microcapsules through electrostatic attraction. Then, a large number of functional groups (-COOH, -OH, -CH, -P=O, etc.) in microcapsules can be used as adsorption sites for surface complexation of Pb(II). At the same time, calcium and sodium ions in microcapsules also contribute to the fixation of Pb(II) through ion exchange. Finally, active microalgae fixed in microcapsules convert Pb^{2+} into mineralized precipitates through surface phosphate precipitation and carbonic anhydrase induced carbonate precipitation.

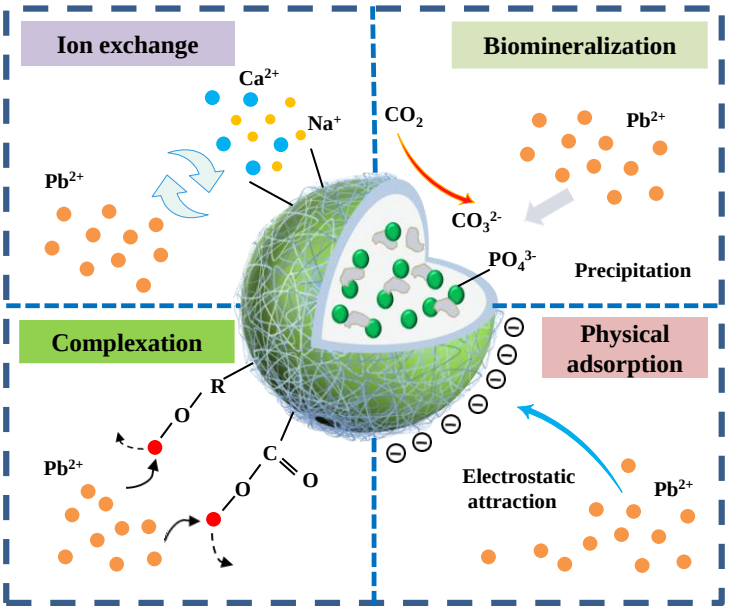

Figure 4.10 Mechanism diagram of Pb(II) removal by PSMC2 microcapsules.

4.3.4 Microcapsules remediation of simulated Pb-contaminated soil

The feasibility of using $PSMC_2$ microcapsules to remediate simulated lead-contaminated soil was evaluated by controlled testing. It is well known that the toxicity of heavy metals is directly related to its occurrence form [82, 83], so the BCR method was used to analyze the changes in Pb fractions (acid soluble, reducible, oxidizable and residual fractions) after remediation, and the results were shown in Figure 4.11. After 7 days of remediation, there was no significant change in the FC group compared with the CK group, while the percentage of acid-soluble and reducible components in the PSC and $PSMC_2$ microcapsule groups was significantly reduced, and the percentage of residual components was significantly increased, indicating that microcapsules can effectively reduce the bioavailability of lead in soil (Figure 4.11 a). Interestingly, the residual lead fraction in $PSMC_2$ microcapsules increased further (16% to 19%) as the remediation time increased to 30 days (Figure 4.11 b), suggesting that introducing montmorillonite into microcapsules could better protect internal microalgae and sustain long-term remediation of Pb-contaminated soil.

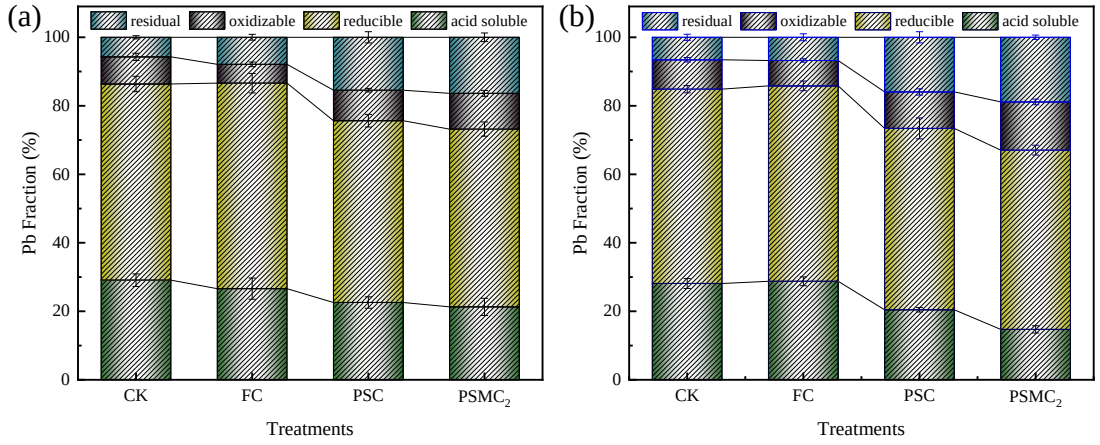

Figure 4.11 Lead fraction in simulated contaminated soil after (a) 7 and (b) 30 days of different remediation treatments.

Chao1, ACE, Shannon and Simpson indices can be used to evaluate the richness and diversity of microbial communities in soil after remediation [84]. The diversity and richness indices of soil microbial communities after different restoration treatments are shown in Table 4.2. It can be seen that ACE and Chao1 index of FC, PSC and $PSMC_2$ groups have increased compared with CK group, and the increase of $PSMC_2$ group is the most obvious, indicating that soil bacterial community richness after $PSMC_2$

microcapsules remediation has been well improved [85]. In addition, the Shannon index of PSC and $PSMC_2$ groups was significantly changed compared with CK group ($P < 0.05$), indicating that soil bacterial community diversity was optimized [86]. The results of principal component analysis (PCA) are shown in Figure 4.12. It can be seen that the first two principal components (PC1 and PC2) together explain 27.82% of the rate of change, indicating that $PSMC_2$ microcapsules alter microbial communities in lead-contaminated soil [87].

Table 4.2 Diversity and Abundance Indices of Species of samples.

Treatment	Community richness		Community diversity	
	Chao1	ACE	Shannon	Simpson
CK	1440.33 ± 67.65c	1485.27 ± 52.34c	7.52 ± 1.04b	0.9566 ± 0.05a
FC	1620.00 ± 13.86bc	1687.26 ± 33.25b	8.08 ± 0.46ab	0.9815 ± 0.01a
PSC	1794.00 ± 139.65ab	1824.13 ± 126.58a	8.89 ± 0.03a	0.9906 ± 0.00a
$PSMC_2$	1870.67 ± 72.39a	1894.38 ± 65.28a	8.86 ± 0.23a	0.9913 ± 0.00a

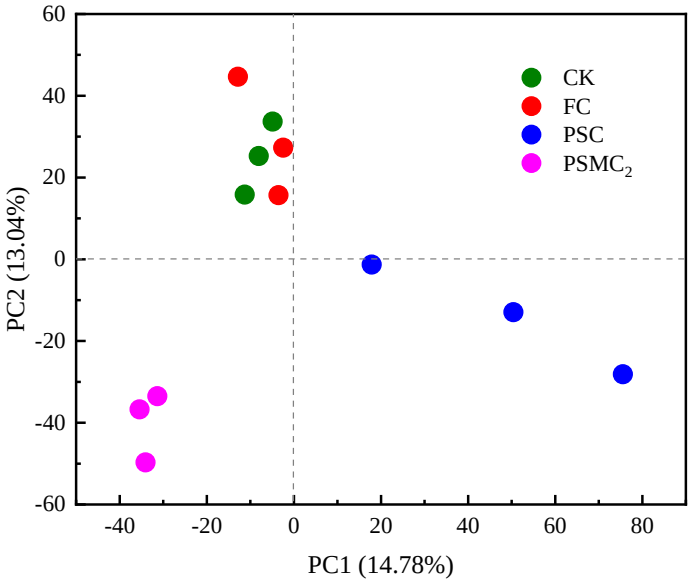

Figure 4.12 Principal component analysis of bacterial community structure in soil after remediation.

Further analysis of the composition of dominant bacterial communities at the phylum level is shown in Figure 4.13 a. The dominant microbial communities of all groups (CK, FC, PSC, and $PSMC_2$) are *Proteobacteria*, *Bacteroidota*, *Actinobacteriota*,

Acidobacteriota, *Chloroflexi*, and *Gemmatimonadota*, indicating that using microalgae microcapsules to remediate soil will not affect the main structure of microbial communities. Numerous studies have shown that highly toxic heavy metals inhibit the proliferation of functional microorganisms such as *Firmicutes* and *Actinobacteriota*, and increase the abundance of heavy metal tolerant bacteria such as *Proteobacteria* [88-90]. Compared with CK, the relative abundance of *Actinobacteriota*, *Acidobacteriota*, and *Gemmatimonadota* increased in the $PSMC_2$ group, while the abundance of *Proteobacteria* decreased. This indicates that $PSMC_2$ microcapsules can reduce lead toxicity in soil and promote the proliferation of beneficial microorganisms. PICRUSt2 was used to predict the function of microbial communities in soil of each group, and the results were shown in Figure 4.13 b. It can be seen that compared with CK, the beneficial functional abundance of Amino acid metabolism, Carbohydrate metabolism, Energy metabolism, Transcription, and Translation in the $PSMC_2$ group was significantly improved. This finding further indicates that $PSMC_2$ microcapsules remediation can help improve soil microbial community function.

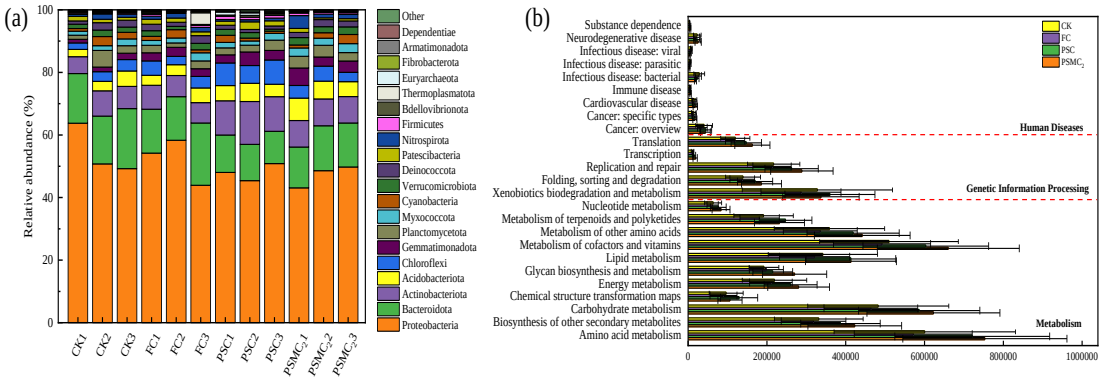

Figure 4.13 (a) Percentage of microbial community abundance at gate level; (b) Functional composition of microbial communities.

4.4 Conclusions

In this study, high-strength PVA/SA/MMT/*Chlorella sorokiniana* FK microcapsules were successfully synthesized by introducing montmorillonite as skeletons. Adsorption experiments have shown that $PSMC_2$ microcapsules (2g MMT) can achieve as high as 100% Pb(II) removal under optimal conditions (initial pH=6, initial Pb(II) concentration of 100 mg/L, microcapsules dosage of 2%). The characterization results showed that $PSMC_2$ microcapsules can enrich Pb(II) from the solution to the surface through electrostatic attraction, surface complexation, and ion

exchange, and then transform them into stable $Pb_5(PO_4)_3Cl$ and $Pb_3(CO_3)_2(OH)_2$ precipitations through surface precipitation and induced carbonate precipitation by active microalgal cells. In addition, soil pot experiments have shown that the application of $PSMC_2$ microcapsules can effectively convert acid soluble lead fractions into low toxicity residue fractions, and stimulate the abundance of beneficial microorganisms such as *Actinobacteriota*, *Acidobacteriota*, and *Gemmatimonadota*, improving soil microbial community structure and ecology function. Therefore, the novel $PSMC_2$ microcapsules can be regarded as an effective material for remediation of lead pollution.

References

[1] X. Ma, Z. Sha, Y. Li, R. Si, A. Tang, A. Fangmeier, X. Liu, Temporal-spatial characteristics and sources of heavy metals in bulk deposition across China, Sci. Total Environ., 926 (2024) 171903.

[2] L.J. Xu, J.Y. Wang, K. Zhang, Response of Heavy Metals to Microseism in Coal Mining Subsidence Water of Huainan, China, Water, 15 (2023).

[3] X.H. Luo, C. Wu, Y.C. Lin, W.C. Li, M. Deng, J.Q. Tan, S.G. Xue, Soil heavy metal pollution from Pb/Zn smelting regions in China and the remediation potential of biomineralization, J. Environ. Sci., 125 (2023) 662-677.

[4] H. Fang, X.J. Wang, D. Xia, J.T. Zhu, W.D. Yu, Y.M. Su, J.W. Zeng, Y.L. Zhang, X.J. Lin, Y.T. Lei, J.R. Qiu, Improvement of Ecological Risk Considering Heavy Metal in Soil and Groundwater Surrounding Electroplating Factories, Processes, 10 (2022).

[5] D. Archundia, B. Prado-Pano, F. Molina-Freaner, Potentially toxic elements in soil-plant-water-animal continuum in a mining area from Northwestern Mexico: animal exposure pathways and health risks for children, Environ. Geochem. Health, 46 (2024).

[6] S. Huang, L.Y. Wang, Y. Zhao, Ecological risk assessment from the perspective of soil heavy metal accumulations in Xiamen city, China, Int. J. Sustainable Dev. World Ecol., 25 (2018) 411-419.

[7] J. Ahn, M.Y. Park, M.Y. Kang, I.S. Shin, S. An, H.R. Kim, Occupational Lead Exposure and Brain Tumors: Systematic Review and Meta-Analysis, Int. J. Environ. Res. Public Health, 17 (2020).

[8] E.V. Arkhipov, R.V. Garipova, L.A. Strizhakov, I.N. Bobkova, N.A. Tairova, Kidney damage caused by lead exposure: historical aspects, Terapevticheskii Arkhiv, 94 (2022) 777-780.

[9] Z.Q. Mei, G.F. Liu, B. Zhao, Z.S. He, S.Y. Gu, Emerging roles of epigenetics in lead-induced neurotoxicity, Environ. Int., 181 (2023).
[10] B. Moavenian, M.H. Hosseini, M. Arabieh, M.R. Pourjavid, M.R. Sohrabi, Extraction of Lead from Water Using Homogeneous Liquid-Liquid Microextraction via Flotation Assistance Method and UV-Vis Spectrophotometric Determination, J. Water Chem. Technol., 40 (2018) 291-296.
[11] Q.Y. Chen, Y. Yao, X.Y. Li, J. Lu, J. Zhou, Z.L. Huang, Comparison of heavy metal removals from aqueous solutions by chemical precipitation and characteristics of precipitates, J. Water Process Eng., 26 (2018) 289-300.
[12] N.A.A. Qasem, R.H. Mohammed, D.U. Lawal, Removal of heavy metal ions from wastewater: a comprehensive and critical review, npj Clean Water, 4 (2021).
[13] R. Shrestha, S. Ban, S. Devkota, S. Sharma, R. Joshi, A.P. Tiwari, H.Y. Kim, M.K. Joshi, Technological trends in heavy metals removal from industrial wastewater: A review, J. Environ. Chem. Eng., 9 (2021).
[14] V. Kumar, S.K. Dwivedi, S. Oh, A review on microbial-integrated techniques as promising cleaner option for removal of chromium, cadmium and lead from industrial wastewater, J. Water Process Eng., 47 (2022).
[15] M. Chakravorty, M. Nanda, B. Bisht, R. Sharma, S. Kumar, A. Mishra, M.S. Vlaskin, P.K. Chauhan, V. Kumar, Heavy metal tolerance in microalgae: Detoxification mechanisms and applications, Aquat. Toxicol., 260 (2023).
[16] Y. Ran, D.X. Sun, X. Liu, L. Zhang, Z.Y. Niu, T.Y. Chai, Z.L. Hu, K. Qiao, Chlorella pyrenoidosa as a potential bioremediator: Its tolerance and molecular responses to cadmium and lead, Sci. Total Environ., 912 (2024).
[17] Z.J. Lu, H.S. Wang, Z.X. Wang, J.Z. Liu, Y.T. Li, L. Xia, S.X. Song, Critical steps in the restoration of coal mine soils: Microbial-accelerated soil reconstruction, Journal of Environmental Management, 368 (2024).
[18] A. Manikandan, P.S. Babu, S. Shyamalagowri, M. Kamaraj, P. Muthukumaran, J. Aravind, Emerging role of microalgae in heavy metal bioremediation, J. Basic Microbiol., 62 (2022) 330-347.
[19] Y.T. Li, S.X. Song, L. Xia, H.Q. Yin, J.V.G. Meza, W.M. Ju, Enhanced Pb(II) removal by algal-based biosorbent cultivated in high-phosphorus cultures, Chem. Eng. J., 361 (2019) 167-179.
[20] L. Xia, J.Q. Tan, R. Huang, Z.J. Zhang, K.Q. Zhou, Y.X. Hu, S.X. Song, L. Xu, M.E. Farías, R.M.T. Sánchez, Enhanced Cd(II) biomineralization induced by

microalgae after cultivating modification in high-phosphorus culture, J. Hazard. Mater., 443 (2023).

[21] J.Q. Tan, H. Yi, Z.J. Zhang, D.L. Meng, Y.T. Li, L. Xia, S.X. Song, L. Wu, R.M.T. Sáncheze, M.E. Farías, Montmorillonite facilitated Pb(II) biomineralization by Chlorella sorokiniana FK in soil, J. Hazard. Mater., 423 (2022).

[22] S. Carfagna, N. Lanza, G. Salbitani, A. Basile, S. Sorbo, V. Vona, Physiological and morphological responses of Lead or Cadmium exposed Chlorella sorokiniana 211-8K (Chlorophyceae), Springerplus, 2 (2013).

[23] N. Expósito, V. Kumar, J. Sierra, M. Schuhmacher, G.G. Papiol, Performance of Raphidocelis subcapitata exposed to heavy metal mixtures, Sci. Total Environ., 601 (2017) 865-873.

[24] J. He, W. Zhang, X.H. Ren, L.F. Xing, S.Q. Chen, C. Wang, Preparation of Different Activated Sludge Immobilized Carriers and Their Organic Wastewater Treatment Performance by Microbial Community, Environ. Eng. Sci., 36 (2019) 604-613.

[25] K.Y. Zhang, Z.D. Teng, W. Shao, Y. Wang, M. Li, S.S. Lam, Effective passivation of lead by phosphate solubilizing bacteria capsules containing tricalcium phosphate, J. Hazard. Mater., 397 (2020).

[26] L.B. Soares, J.M. da Silveira, L.E. Biazi, L. Longo, D. de Oliveira, A. Furigo, Jr., J.L. Ienczak, An overview on fermentation strategies to overcome lignocellulosic inhibitors in second-generation ethanol production using cell immobilization, Crit. Rev. Biotechnol., 43 (2023) 1150-1171.

[27] M. Mollaei, S. Abdollahpour, S. Atashgahi, H. Abbasi, F. Masoomi, I. Rad, A.S. Lotfi, H.S. Zahiri, H. Vali, K.A. Noghabi, Enhanced phenol degradation by Pseudomonas sp SA01: Gaining insight into the, J. Hazard. Mater., 175 (2010) 284-292.

[28] Z.D. Teng, W. Shao, K.Y. Zhang, F.L. Yu, Y.Q. Huo, M. Li, Enhanced passivation of lead with immobilized phosphate solubilizing bacteria beads loaded with biochar/ nanoscale zero valent iron composite, J. Hazard. Mater., 384 (2020).

[29] Y.Z. Gong, Q.Y. Niu, Y.G. Liu, J. Dong, M.M. Xia, Development of multifarious carrier materials and impact conditions of immobilised microbial technology for environmental remediation: A review, Environ. Pollut., 314 (2022).

[30] L. Lv, J. Chen, Z. Wei, P. Hao, P. Wang, X. Liu, W. Gao, L. Sun, J. Liang, Z. Ren, G. Zhang, W. Li, A new strategy for accelerating recovery of anaerobic granular sludge

after low-temperature shock: In situ regulation of quorum sensing microorganisms embedded in polyvinyl alcohol sodium alginate, Bioresour. Technol., (2024) 130709.
[31] C. Zhao, H.W. Chen, Y.F. Song, L. Zhu, T.C. Ai, X.X. Wang, Z. Liu, X. Wei, Electricity production performance enhancement of microbial fuel cells with double-layer sodium alginate hydrogel bioanodes driven by high-salinity waste leachate, Water Res., 242 (2023).
[32] A. Hattali, O. Bouras, S. Hanini, Removal of cadmium from aqueous solution by hybrid reinforced porous gelled beads based on SA/PVA/Al-Mt and CaCO3, Desalin. Water Treat., 279 (2022) 48-54.
[33] A.S. Purnomo, F.W. Hairunnisa, Misdar, V.P. Maria, A.A. Rohmah, S.R. Putra, H.S. Putro, H.D. Rizqi, Anionic dye removal by immobilized bacteria into alginate-polyvinyl alcohol-bentonite matrix, Heliyon, 10 (2024) e27871.
[34] Y. Shi, S.T. Zhong, X. Wang, C.P. Feng, A review of the removal of heavy metal ions in wastewater by modified montmorillonite, Water Policy, 24 (2022) 1590-1609.
[35] B. Biswas, L.N. Warr, E.F. Hilder, N. Goswami, M.M. Rahman, J.G. Churchman, K. Vasilev, G. Pan, R. Naidu, Biocompatible functionalisation of nanoclays for improved environmental remediation, Chem. Soc. Rev., 48 (2019) 3740-3770.
[36] L.Y. Liu, C.L. Kong, H.Y. Zhao, F.Q. Lu, Elucidating the enhancement of kaolinite flotation by iron content through density functional theory: A study on sodium oleate adsorption efficiency, International Journal of Mining Science and Technology, 34 (2024) 855-866.
[37] M. Su, F.Y. Han, M.X. Wang, J.X. Ma, X.W. Wang, Z.J. Wang, S.J. Hu, Z. Li, Clay-assisted protection of Enterobacter sp. from Pb (II) stress, Ecotoxicology and Environmental Safety, 208 (2021).
[38] Y.H. Xing, X.S. Luo, S. Liu, W.J. Wan, Q.Y. Huang, W.L. Chen, Synergistic effect of biofilm growth and cadmium adsorption via compositional changes of extracellular matrix in montmorillonite system, Bioresour. Technol., 315 (2020).
[39] Z. Jiang, N. An, Y.X. Chu, B. Cao, F.X. Wu, Y. Zhang, Y.X. Zhang, Y. Li, Y. Zhang, Growth, biofilm formation and atrazine degrading gene (trzN) expression of Arthrobacter sp. DNS10 cultured with montmorillonite, kaolinite and goethite, Chemosphere, 307 (2022).
[40] Y. Jin, D. Liu, W. Xiong, Z. Wu, G. Xiao, S. Wang, H. Su, Enhancing Nitrogen Removal Performance Using Immobilized Aerobic Denitrifying Bacteria by Modified Polyvinyl Alcohol/Sodium Alginate (PVA/SA), Chemosphere, (2024) 141954.

[41] L.C. Xie, Z.C. Zhang, Y.C. He, Antibacterial Effect of Polyvinyl Alcohol/Biochar-Nano Silver/Sodium Alginate Gel Beads, Processes, 11 (2023).
[42] Z.W. Jiang, Z.J. Zheng, J.N. Wu, X.R. Liu, H. Yu, J.Y.H. Shen, Synthesis, characterization and performance of microorganism-embedded biocomposites of LDH-modified PVA/SA hydrogel beads for enhanced biological nitrogen removal process, Process Biochem., 121 (2022) 542-552.
[43] J. Fabrowska, B. Messyasz, J. Szyling, J. Walkowiak, B. Leska, Isolation of chlorophylls and carotenoids from freshwater algae using different extraction methods, Phycol. Res., 66 (2018) 52-57.
[44] D.M. Moore, R. Reynolds, Jr, X-ray Diffraction and the Identification and Analysis of Clay Minerals, 1989.
[45] G. Rauret, J.F. Lopez-Sanchez, A. Sahuquillo, R. Rubio, C. Davidson, A. Ure, P. Quevauviller, Improvement of the BCR three step sequential extraction procedure prior to the certification of new sediment and soil reference materials, Journal of environmental monitoring : JEM, 1 (1999) 57-61.
[46] X.G. Wang, X.Z. Zhang, F.B. Zou, J.L. Zhu, Self-healing microcapsules modified by montmorillonite for modulating slow-release properties, Mater. Chem. Phys., 291 (2022).
[47] M.T. Musa, N. Shaari, N.F. Raduwan, S.K. Kamarudin, W.Y. Wong, Alginate/PVA Polymer Electrolyte Membrane Modified by Hydrophilic Montmorillonite for Structure and Selectivity Enhancement for DMFC Application, Polymers, 15 (2023).
[48] K. Essifi, M. Brahmi, A. Ed-Daoui, A. Boussetta, M. Benelmostafa, M. Dahmani, S. Salhi, A. Moubarik, A. El Bachiri, A. Tahani, Investigating the effect of clay content and type on the mechanical performance of calcium alginate-based hybrid bio-capsules, Int. J. Biol. Macromol., 242 (2023).
[49] X.Y. Liu, Y. Hong, M. Liang, Q.Y. Zhai, Bioremediation of zinc and manganese in swine wastewater by living microalgae: Performance, mechanism, and algal biomass utilization, Bioresour. Technol., 385 (2023).
[50] M. Kavisri, M. Abraham, M. Moovendhan, Effective removal of fluoride ions from aqueous solution by marine microalgae as natural biosorbent, Chemosphere, 313 (2023).
[51] Z.X. Wang, Z.J. Zhang, L. Xia, M.E. Farias, R.M.T. Sanchez, C. Belfiore, M.L. Montes, X. Tian, J.H. Chen, S.X. Song, Sulfate induced surface modification of Chlorella for enhanced mercury immobilization, J. Environ. Chem. Eng., 10 (2022).

[52] W. Zhang, Q. Deng, Q.L. He, J.Y. Song, S.L. Zhang, H.Y. Wang, J.P. Zhou, H.N. Zhang, A facile synthesis of core-shell/bead-like poly (vinyl alcohol)/alginate@PAM with good adsorption capacity, high adaptability and stability towards Cu(II) removal, Chem. Eng. J., 351 (2018) 462-472.

[53] W. Wang, Y.L. Zhao, H. Yi, T.X. Chen, S.C. Kang, T.T. Zhang, F. Rao, S.X. Song, Pb(II) removal from water using porous hydrogel of chitosan-2D montmorillonite, Int. J. Biol. Macromol., 128 (2019) 85-93.

[54] C. Paluszkiewicz, E. Stodolak, M. Hasik, M. Blazewicz, FT-IR study of montmorillonite-chitosan nanocomposite materials, Spectrochimica Acta Part a-Molecular and Biomolecular Spectroscopy, 79 (2011) 784-788.

[55] C.X. Xiang, Q. Zhang, Z.J. Guo, Z.H. Wang, W.Y. Chen, X.N. Li, X.C. Wei, P.C. Li, Facile preparation and properties of porous poly(vinyl alcohol)/trehalose/ nano-clay hydrogels with high mechanical strength for potential application in bone tissue engineering, Eur. Polym. J., 197 (2023).

[56] X.L. Qiao, L.B. Niu, H.L. Zhang, X. Wen, Y.Y. Cao, G.Y. Bai, Controllable fabrication of a novel porous Ni-alginate hybrid material for hydrogenation, Applied Catalysis B-Environmental, 218 (2017) 721-730.

[57] Y.Y. Wang, X.Y. Wang, J. Shi, R. Zhu, J.H. Zhang, Z.R. Zhang, D.W. Ma, Y.J. Hou, F. Lin, J. Yang, M. Mizuno, A Biomimetic Silk Fibroin/Sodium Alginate Composite Scaffold for Soft Tissue Engineering, Sci. Rep., 6 (2016).

[58] S.B. Hua, H.Z. Ma, X. Li, H.X. Yang, A. Wang, pH-sensitive sodium alginate/poly(vinyl alcohol) hydrogel beads prepared by combined Ca2+ crosslinking and freeze-thawing cycles for controlled release of diclofenac sodium, Int. J. Biol. Macromol., 46 (2010) 517-523.

[59] R.L. Gao, L. Xiang, H.Q. Hu, Q.L. Fu, J. Zhu, Y.H. Liu, G.Y. Huang, High-efficiency removal capacities and quantitative sorption mechanisms of Pb by oxidized rape straw biochars, Sci. Total Environ., 699 (2020).

[60] X.Q. Wu, Y.T. Song, P. Yin, Q. Xu, Z.L. Yang, Y.B. Xu, X.G. Liu, Y. Wang, W.J. Sun, H.L. Cai, Fabrication of the composite sepiolite@polyethyleneimine/sodium alginate and its excellent adsorption performance for heavy metal ions, Appl. Clay Sci., 228 (2022).

[61] Z.H. Wang, P.S. Huang, Y.H. Yan, Y. Tao, W. Lei, M.Z. Xia, F.Y. Wang, Effective removal of Pb(II) and Congo red by polyrhodanine-modified sepiolite, J. Water Process Eng., 54 (2023).

[62] Y. Gao, L.F. Yao, S.Z. Zhang, Q.Y. Yue, W.Y. Yin, Versatile crosslinking synthesis of an EDTA-modified UiO-66-NH2/cotton fabric composite for simultaneous capture of heavy metals and dyes and efficient degradation of organophosphate, Environ. Pollut., 316 (2023).
[63] Y.V. Nancharaiah, M. Rajadurai, V.P. Venugopalan, Single cell level microalgal ecotoxicity assessment by confocal microscopy and digital image analysis, Environ. Sci. Technol., 41 (2007) 2617-2621.
[64] D.Y. Wang, F.L. de los Reyes, III, J.J. Ducoste, Microplate-Based Cell Viability Assay as a Cost-Effective Alternative to Flow Cytometry for Microalgae Analysis, Environ. Sci. Technol., 57 (2023) 21200-21211.
[65] P. Zhang, Y.M. Ding, T.L. Zhao, Y.H. Wang, Q.Z. Yao, S.Q. Fu, G.T. Zhou, Can phosphobacteria simultaneously achieve phosphorus recovery and Pb2+removal from wastewater by biomineralization?, Chem. Eng. J., 455 (2023).
[66] Z.X. Wang, L. Xia, S.X. Song, M.E. Farías, Y.T. Li, C.Y. Tang, Cadmium removal from diluted wastewater by using high-phosphorus-culture modified microalgae, Chem. Phys. Lett., 771 (2021).
[67] X.Y. He, J.R. Lu, H. Wei, B.X. Liu, Macroporous honeycomb-like magnesium oxide fabricated as long-life and outstanding Pb(II) adsorbents combined with mechanism insight, Environ. Sci. Pollut. Res., 30 (2023) 38380-38393.
[68] H.M. Hao, Y.H. Bi, N.N. Wei, P.C. Lin, S.H. Mei, Z.G. Zhou, Expression of a periplasmic β-carbonic anhydrase (CA) gene is positively correlated with HCO3- utilization by the gametophytes of Saccharina japonica (Phaeophyceae, Ochrophyta), J. Appl. Phycol., 35 (2023) 3021-3040.
[69] C. Schwaner, M. Barbosa, E.P. Espinosa, B. Allam, Probing the role of carbonic anhydrase in shell repair mechanisms in the eastern oyster Crassostrea virginica under experimental acidification stress, J. Exp. Mar. Biol. Ecol., 572 (2024).
[70] S.B. He, B.B. Ruan, Y.P. Zheng, X.B. Zhou, X.P. Xu, Immobilization of chlorine dioxide modified cells for uranium absorption, J. Environ. Radioact., 137 (2014) 46-51.
[71] X.L. Li, Y.X. Qi, Y.F. Li, Y. Zhang, X.H. He, Y.H. Wang, Novel magnetic beads based on sodium alginate gel crosslinked by zirconium(IV) and their effective removal for Pb2+ in aqueous solutions by using a batch and continuous systems, Bioresour. Technol., 142 (2013) 611-619.

[72] J.P. Li, R. Bai, W. Chen, C.Y. Ren, F. Yang, X.C. Tian, X.F. Xiao, F. Zhao, Efficient lead immobilization by bio-beads containing Pseudomonas rhodesiae and bone char, J. Hazard. Mater., 447 (2023).
[73] K.J. Zhang, Y.W. Xue, J.Q. Zhang, X.L. Hu, Removal of lead from acidic wastewater by bio-mineralized bacteria with pH self-regulation, Chemosphere, 241 (2020).
[74] J. Xiao, R. Hu, G.C. Chen, Micro-nano-engineered nitrogenous bone biochar developed with a ball-milling technique for high-efficiency removal of aquatic Cd(II), Cu(II) and Pb(II), J. Hazard. Mater., 387 (2020).
[75] T.H. Chen, H.W. Li, H.L. Wang, X.H. Zou, H.B. Liu, D. Chen, Y.F. Zhou, Removal of Pb(II) from Aqueous Solutions by Periclase/Calcite Nanocomposites, Water Air and Soil Pollution, 230 (2019).
[76] Z.J. Zhang, Z. Wang, J.Q. Tan, K.Q. Zhou, J.V. Garcia-Meza, S.X. Song, L. Xia, Yeast-derived biochar to load CoFe2O4: Degradation of tetracycline hydrochloride by heterogeneous activation of peroxymonosulfate, J. Environ. Chem. Eng., 11 (2023).
[77] H. Liu, P. Dai, J. Zhang, C.L. Zhang, N. Bao, C. Cheng, L. Ren, Preparation and evaluation of activated carbons from lotus stalk with trimethyl phosphate and tributyl phosphate activation for lead removal, Chem. Eng. J., 228 (2013) 425-434.
[78] G. Liu, B. Liao, T. Lu, H.X. Wang, L.S. Xu, Z.K. Li, C.W. Ye, Insight into immobilization of Pb2+ in aqueous solution and contaminated soil using hydroxyapatite/attapulgite composite, Colloids and Surfaces a-Physicochemical and Engineering Aspects, 603 (2020).
[79] N. Hao, J.N. Cao, J.S. Ye, C. Zhang, C. Li, B. Bate, Content and morphology of lead remediated by activated carbon and biochar: A spectral induced polarization study, J. Hazard. Mater., 411 (2021).
[80] L.H. Dong, W.J. Liu, R.F. Jiang, Z.S. Wang, Study on the adsorption mechanism of activated carbon removing low concentrations of heavy metals, Desalin. Water Treat., 57 (2016) 7812-7822.
[81] E.J. Kim, J.E. Herrera, Characteristics of Lead Corrosion Scales Formed during Drinking Water Distribution and Their Potential Influence on the Release of Lead and Other Contaminants, Environ. Sci. Technol., 44 (2010) 6054-6061.
[82] Z.B. Shang, Y.J. Xu, P.X. Wu, Z. Ahmed, W.C. Niu, J.Y. Wu, Q.R. Feng, N.W. Zhu, Mixed solvent fabrication of tobermorite and the fixation of heavy metals in water and soil, J. Environ. Manage., 345 (2023).

[83] H.Z. Yuan, H.B. Yin, Z. Yang, J.H. Yu, E.F. Liu, Q. Li, Z.Q. Tai, Y.W. Cai, Diffusion kinetic process of heavy metals in lacustrine sediment assessed under different redox conditions by DGT and DIFS model, Sci. Total Environ., 741 (2020).
[84] D.F. Huang, Y.B. Xu, F.D. Lei, X.Q. Yu, Z.Z. Ouyang, Y.H. Chen, H.Z. Jia, X.T. Guo, Degradation of polyethylene plastic in soil and effects on microbial community composition, J. Hazard. Mater., 416 (2021).
[85] Z. Zhou, L. Xia, X.Z. Wang, C.Y. Wu, J.Z. Liu, J.B. Li, Z.J. Lu, S.X. Song, J. Zhu, M.L. Montes, M. Benzaazoua, Coal slime as a good modifier for the restoration of copper tailings with improved soil properties and microbial function, Environ. Sci. Pollut. Res., 30 (2023) 109266-109282.
[86] H.C. Sha, J. Li, L.Q. Wang, H.D. Nong, G.H. Wang, T.T. Zeng, Preparation of phosphorus-modified biochar for the immobilization of heavy metals in typical lead-zinc contaminated mining soil: Performance, mechanism and microbial community, Environ. Res., 218 (2023).
[87] Y. Hong, D. Li, C. Xie, X.X. Zheng, J. Yin, Z.D. Li, K.L. Zhang, Y.Q. Jiao, B.J. Wang, Y.M. Hu, Z.Q. Zhu, Combined apatite, biochar, and organic fertilizer application for heavy metal co-contaminated soil remediation reduces heavy metal transport and alters soil microbial community structure, Sci. Total Environ., 851 (2022).
[88] Y. Chen, F.F. Chen, M.D. Xie, Q.Q. Jiang, W.Q. Chen, T.Q. Ao, The impact of stabilizing amendments on the microbial community and metabolism in cadmium-contaminated paddy soils, Chem. Eng. J., 395 (2020).
[89] J.H. Li, C.G. Xia, R. Cheng, J.R. Lan, F.Y. Chen, X.L. Li, S.Y. Li, J. Chen, T.Y. Zeng, H.B. Hou, Passivation of multiple heavy metals in lead-zinc tailings facilitated by straw biochar-loaded N-doped carbon aerogel nanoparticles: Mechanisms and microbial community evolution, Sci. Total Environ., 803 (2022).
[90] J.X. Zhang, L.M. Dai, J.H. Li, Q.Y. Zeng, M. Zhou, H.B. Hou, Phosphate tailings-based slow-release heavy metal passivation materials: Mechanism, environmental risk, and microbial community evolution, J. Cleaner Prod., 434 (2024).

Chapter V. From Pollutant to Partner: Functional Roles of Polystyrene Nanoplastics in Microbial Carbonate Mineralization and Copper Remediation

5.1 Introduction

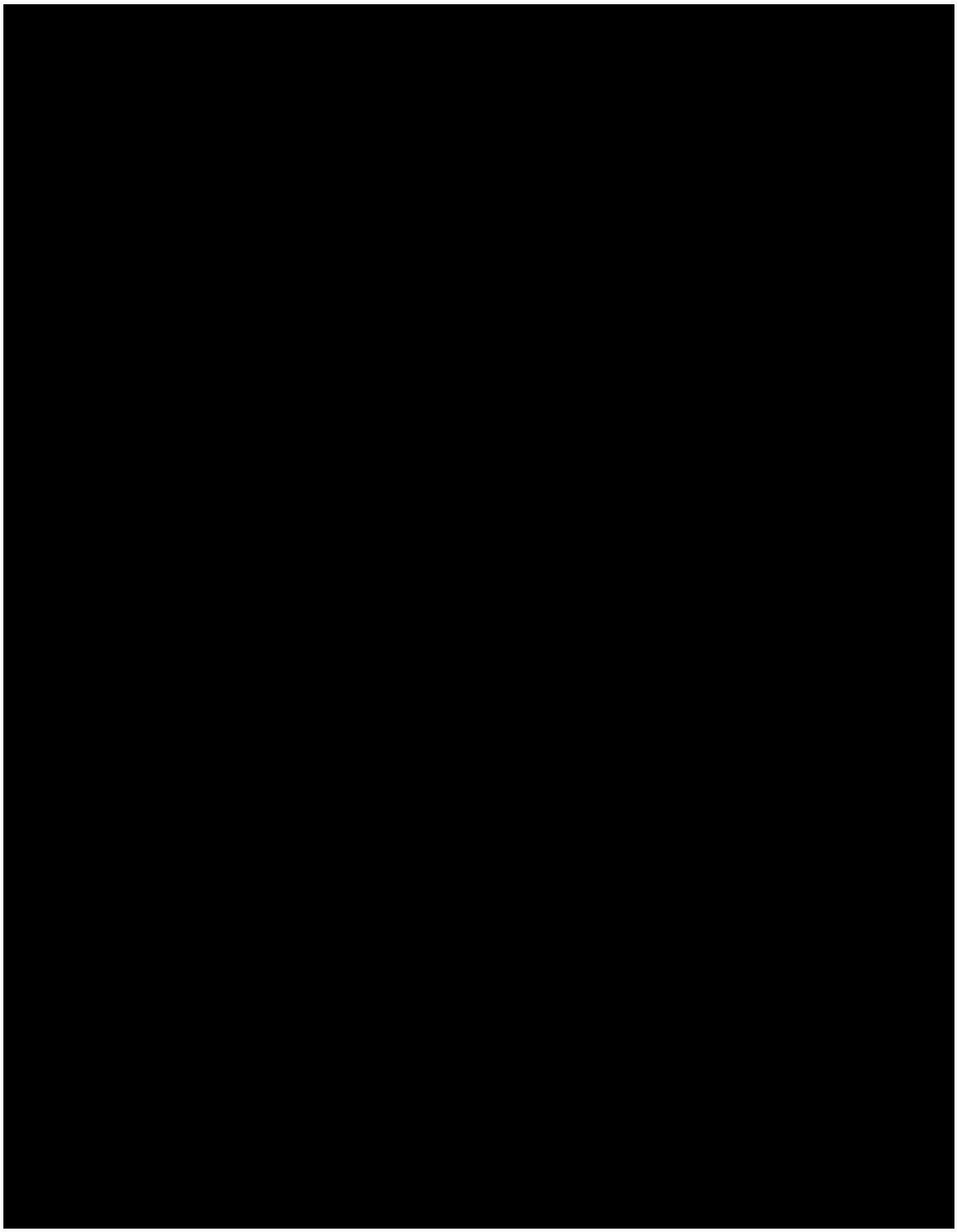

Chapter VI. Synergistic Effects of Peat and MICP for Copper Tailings Remediation: Metal Immobilization, Nutrient Retention, and Microbial Regulation

6.1 Introduction

Global copper demand has surged in recent decades due to its critical role in industrial upgrades and renewable energy infrastructure, such as photovoltaic panels and electric vehicle batteries [1, 2]. This growth has intensified copper mining, generating massive amounts of copper tailings—fine-grained residues stored in open-air impoundments or dams [3]. These tailings pose severe environmental and health risks: they leach heavy metals like copper into water systems, contaminating the food chain and causing health issues including kidney damage, developmental disorders, and cancer [4-6]. Ecologically, the tailings create barren, nutrient-poor, and toxic environments that prevent natural ecosystem recovery [7, 8]. Conventional cleanup methods are often costly, slow, or risk causing secondary pollution, underscoring the need for innovative technologies that can effectively detoxify metals and restore ecological functions [9, 10].

Microbially induced carbonate precipitation (MICP) is a promising biotech solution for copper tailings rehabilitation [11, 12]. This process uses ureolytic bacteria to hydrolyze urea into ammonium (NH_4^+) and carbonate (CO_3^{2-}) ions; the latter reacts with exogenous/endogenous calcium (Ca^{2+}) to form biogenic calcium carbonate ($CaCO_3$) precipitates [13, 14]. These precipitates immobilize heavy metals via surface adsorption, lattice substitution, and physical encapsulation, solving the core issue of metal bioavailability [15-17]. However, practical MICP application faces critical bottlenecks that hinder its ecological sustainability: (1) The harsh tailings environment limits the growth and activity of MICP engineering bacteria, further reducing the process's stability and efficiency [18, 19]. (2) Though effective at immobilizing heavy metals, MICP hardly improves tailings' nutrient poverty—a major constraint on microbial metabolism and establishing a self-sustaining ecosystem [20, 21]. (3) High concentrations of MICP reagents and the resulting alkaline microenvironment reduce indigenous microbial diversity, disrupting key biogeochemical cycles (e.g., nitrogen, carbon) essential for long-term ecosystem recovery [22-24]. These limitations indicate

that conventional MICP primarily addresses metal immobilization, while largely neglecting nutrient restoration and microbial ecological regulation, which are essential for sustainable tailings rehabilitation.

Certain additives have been introduced to improve MICP performance, yet their functions remain relatively single-dimensional [25-27]. For example, biochar-assisted MICP primarily enhances heavy metal adsorption and provides microbial microhabitats, oyster shell-based MICP mainly supplies Ca^{2+} and buffers pH, and multi-walled carbon nanotubes-enhanced MICP reduces heavy metal leaching [28-30]. However, these approaches largely focus on individual limiting factors and fail to simultaneously regulate metal speciation, nutrient availability, and microbial ecological stability. Unlike these additive-assisted MICP systems, peat—a carbon-rich organic substrate formed through long-term anaerobic decomposition—provides a uniquely multifunctional platform for MICP enhancement. Its high cation exchange capacity and abundant oxygen-containing functional groups (-COOH, -OH) promote heavy metal adsorption and complexation, enhancing Cu stabilization [31]. Meanwhile, humic substances and readily degradable organic carbon serve as a long-term nutrient reservoir, supporting ureolytic bacterial metabolism and improving soil fertility [32, 33]. More importantly, peat harbors diverse indigenous microbial consortia that act as "ecological engineers" facilitating the recovery of native communities suppressed by MICP-induced alkalinity [34, 35]. Nevertheless, compared with existing composite MICP strategies, the coupled mechanisms linking metal speciation transformation, nutrient cycling, and microbial succession within peat-assisted MICP systems remain insufficiently understood.

This study developed an integrated peat-ureolytic bacteria system to address the coupled challenges of copper immobilization and ecological restoration in tailings environments. Specific objectives are: (1) elucidate peat's regulation of copper speciation transformation and long-term stability during MICP; (2) quantify peat-MICP synergies in improving tailing nutrients and biogeochemical cycling enzyme activities; (3) clarify peat's role in regulating microbial community structure, keystone taxa, and functional pathways during MICP; (4) validate practical applicability via field tests in real tailings, assessing resistance to natural environmental fluctuations and long-term efficacy. Through multi-scale analyses (geochemical speciation, biochemical assays, microbial profiling, field monitoring), this study aims to establish a comprehensive peat-MICP remediation framework co-optimizing contaminant sequestration and

ecological recovery, providing a sustainable strategy for rehabilitating heavy metal-contaminated mine tailings.

6.2 Materials and methods

6.2.1 Experimental Tailings

The copper tailings used in this study were collected from a tailing's reservoir in Daye City, Hubei Province, China, at a depth of 0-20 cm. After removing visible impurities, the tailings were air-dried for subsequent experiments. Laser particle size analysis (Malvern Mastersizer 3000) showed a predominant particle size distribution of 20-50 μm with a median diameter (D_{50}) of 23.15 μm (Figure 6.1), classifying them as fine-grained tailings and informing subsequent remediation strategy selection. Comprehensive characterization through XRF, ICP-OES, and physicochemical analyses revealed distinctive properties (Table 6.1-6.3): elemental composition showed lower Si and Al but higher Ca and Fe compared to typical silicate tailings. Copper was identified as the primary contaminant at 482 mg/kg, exceeding China's agricultural soil risk control standard (GB 15618-2018) [36]; physicochemical parameters included alkaline pH (7.92), low organic matter (OM, 2.33 g/kg), deficient available phosphorus (AP, 3.11 mg/kg), along with unfavorable physical properties including high bulk density (BD, 1.69 g/cm³) and low porosity (POR, 43.11%). These characteristics collectively demonstrate significant ecological barrenness necessitating remediation intervention.

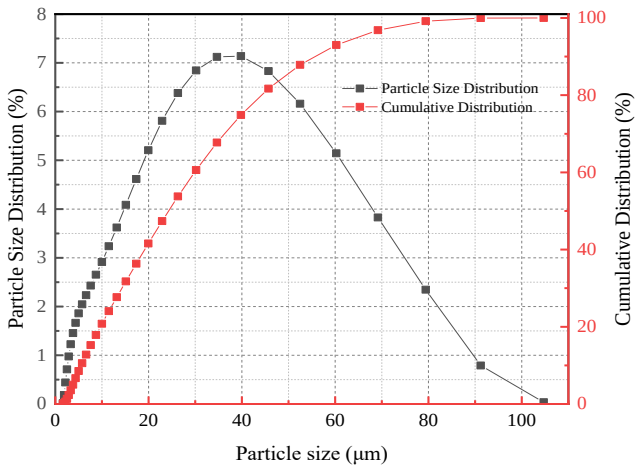

Figure 6.1 Particle Size Distribution and Cumulative Distribution Curve of Copper Tailings.

Table 6.1 Major element contents of raw copper tailings via X-ray fluorescence (XRF) analysis.

Elements	O	Ca	Si	Al	Fe	Mg	P
Content (%)	28.78	18.25	9.47	3.14	12.42	1.7	0.03
Elements	S	K	Na	Cu	Zn	Loss	Total
Content (%)	0.7	0.64	0.2	0.06	0.02	24.59	100

Table 6.2 Major heavy metal contents of raw copper tailings via ICP-OES analysis.

Elements	Cu	Zn	Pb	Co	Ni	Cd	Mo
Content(mg/kg）	482.5	176.4	5.6	12.3	7.2	0.3	5.2

Table 6.3 Major physicochemical properties of raw copper tailings.

pH	OM (g/kg)	CEC (cmol/kg)	AN (mg/kg)	AP (mg/kg)	Ak (mg/kg)	BD (g/cm^3)	POR (%)
7.92	2.33	6.57	23.38	3.11	32.57	1.69	43.11

6.2.2 Bacterial Strain and Peat Preparation

The peat used in this study was a commercially available, untreated natural product sourced from Liaoning Shengyuan Peat Development and Utilization Co., Ltd., China. The peat was not subjected to chemical activation or sterilization prior to use, ensuring the preservation of its natural organic structure. The peat exhibited typical physicochemical characteristics of natural peat, including an organic matter content of 95 ± 2.3%, a pH of 5.2 ± 0.2, and a total humic acid content of 62 ± 1.8%, indicating a moderately humified peat material. These properties are representative of peat commonly applied in ecological restoration studies and provide a stable organic matrix for incubation experiments. The urease-producing strain SX1, used for MICP, was isolated from the copper tailings and identified as *Lysinibacillus* sp. via 16S rDNA sequencing (Illumina MiSeq, primers 515F/907R), as detailed previously [37]. In this experiment, the strain was first pre-cultured in LB medium (containing 10 g/L tryptone, 5 g/L yeast extract, and 10 g/L NaCl, pH 7.0) at 30 °C with shaking at 180 rpm for 24 hours. The cells were then collected by centrifugation, washed three times with sterile saline, and resuspended to an OD_{600} of 1.0 (approximately 10^8 CFU/mL) to serve as the

inoculum.

6.2.3 Experiment Setup

A laboratory incubation experiment was conducted to evaluate the synergistic effects of peat and microbially induced carbonate precipitation (MICP) on copper immobilization in tailings. Four treatments—control (CK), peat amendment (PEAT), MICP, and combined peat-MICP (PMICP)—were set up in triplicate, each using 200 g of air-dried tailings in 500 mL plastic incubation boxes. Samples were incubated in an artificial climate chamber (Shanghai Boxun RXZ-500C, China) at 25°C under a 12 h light/12 h dark cycle for 3 months, with moisture maintained at 60% of maximum water-holding capacity by replenishing deionized water every 3 days using the weighing method. CK consisted of raw tailings; PEAT was amended with 3% (w/w) peat, a dosage selected based on commonly reported application ranges in peat-assisted tailings reclamation studies to ensure adequate nutrient input while maintaining system stability [38]; MICP was inoculated with 10% (v/w) SX1 bacterial suspension (OD_{600} = 1.0, approximately 10^8 CFU/mL), resulting in a final cell density of approximately 10^7 CFU per gram of tailings, and sprayed with 100 mL of curing solution (containing 1.0 mol/L urea and 1.0 mol/L $CaCl_2$); PMICP combined 3% (w/w) peat with the same MICP inoculation and curing procedure. After incubation, one portion of each sample was air-dried for physicochemical and copper speciation analysis, while the rest were stored at -4°C (Haier HYC-326, China) for enzyme assays and at -80°C (Thermo Scientific 905, USA) for microbial community analysis.

6.2.4 Determination Indicators and Methods

Copper (Cu) speciation was determined using a modified Tessier sequential extraction procedure, separating Cu into exchangeable, carbonate-bound, Fe-Mn oxide-bound, organic matter-bound, and residual fractions [39]. Cu bioavailability and leaching risk were further assessed via single extractions with 0.01 M calcium chloride ($CaCl_2$), diethylenetriaminepentaacetic acid (DTPA), and the toxicity characteristic leaching procedure (TCLP) [40, 41] , with Cu concentrations quantified by flame atomic absorption spectrometry (FAAS).

Major elements in raw tailings were analyzed by X-ray fluorescence (XRF, Bruker S8 Tiger, Germany), and total heavy metals by inductively coupled plasma optical emission spectrometry (ICP-OES, PerkinElmer Optima 8300, USA). Basic

physicochemical properties—including pH, organic matter (OM), total nitrogen (TN), available phosphorus (AP), and available potassium (AK), and carbon pool components (total organic carbon (TOC), dissolved organic carbon (DOC)) were measured by standard soil methods: pH with a pH meter (Leici PHS-3C, China), organic matter via potassium dichromate oxidation (Metrohm 888, China), and TOC/DOC with a total organic carbon analyzer (Shimadzu TOC-L, USA) [42]. Nitrogen forms and enzyme activities (urease, dehydrogenase, etc.) were determined by KCl leaching-colorimetry and substrate culture-colorimetry using a UV-visible spectrophotometer (Shimadzu UV-2600, Japan) [43].

Dissolved organic matter (DOM) composition was characterized by three-dimensional excitation-emission matrix (3D-EEM) fluorescence spectroscopy (Hitachi F-7100, Japan) with fluorescence indices [44]. Mineralogical characteristics and surface elemental states of incubated samples were examined by X-ray diffraction (XRD, Bruker D8 Advance, Germany), scanning electron microscopy-energy dispersive spectroscopy (SEM-EDS, Zeiss Sigma 300, Germany), Fourier transform infrared spectroscopy (FT-IR, Nicolet iS50, USA), and X-ray photoelectron spectroscopy (XPS, Thermo Scientific K-Alpha, USA).

6.2.5 Microbial Community Analysis

Microbial community analysis was performed with three replicates per treatment. Total genomic DNA was extracted from frozen tailings using a cetyltrimethylammonium bromide (CTAB)-based soil DNA extraction kit. The V4-V5 region of the 16S ribosomal ribonucleic acid (16S rRNA) gene was amplified using primers 515F/907R and sequenced on the Illumina MiSeq PE300 platform. Sequence processing and quality control were conducted in R using DADA2 and phyloseq, with operational taxonomic units (OTUs) clustered at 97% similarity. Alpha diversity (α-diversity) was evaluated using standard diversity indices, while beta diversity (β-diversity) was assessed by principal coordinate analysis (PCoA) based on Bray-Curtis distances with permutational multivariate analysis of variance (PERMANOVA). Community-environment relationships were examined by redundancy analysis (RDA). Differential abundance analysis was performed with DESeq2, co-occurrence networks were constructed using igraph and visualized in Cytoscape, and microbial functional potential was predicted using both functional annotation of prokaryotic taxa (FAPROTAX) and phylogenetic investigation of communities by reconstruction of

unobserved states (PICRUSt2).

6.2.6 Field-scale validation experiment

A field-scale validation experiment was conducted at the Sanxin copper tailings reservoir in Daye City, Hubei Province, China, from July 2024 to June 2025 (monthly temperature and precipitation are provided in Table 6.4). The tailings surface (0-20 cm) was homogenized by ploughing before treatment application. Four treatments—control (CK), peat amendment (PEAT), microbially induced carbonate precipitation (MICP), and combined peat-MICP (PMICP)—were applied in randomly arranged 2 m × 2 m plots, using the same amendment types, dosages, and procedures as in the laboratory incubation. After three months, ryegrass (*Lolium perenne*) was sown at 30 g/m². Plant growth, physiological parameters, and copper accumulation were measured five months after sowing following established protocols [45, 46]. To assess the temporal stability of copper immobilization, soil samples were collected at 3, 5, and 12 months for Cu speciation analysis using the modified Tessier sequential extraction procedure.

Table 6.4 Temperature and rainfall data (2024/07-2025/06).

2024/07-2024/12	July	August	September	October	November	December
Temperature (℃)	23~39	23~40	16~39	9~30	1~28	-5~23
Rainfall (mm)	49.5	0.3	4.7	12	25.8	20.9
2025/01-2025/06	January	February	March	April	May	June
Temperature (℃)	-4~21	-4~24	2~37	8~33	11~35	18~36
Rainfall (mm)	70.8	21.1	14.5	31.1	17.2	811.2

6.3 Results and discussion

6.3.1 Immobilization of Cu in tailings

Cu chemical speciation across treatments is presented in Figure 6.2 a. The CK

group had the highest exchangeable Cu (55.07 ± 2.14 mg/kg), posing substantial environmental risks. PEAT reduced exchangeable Cu by 26.5% via humic substance complexation (with a 78.2% increase in organic-bound Cu), confirming organic matter's ability to immobilize labile Cu [33]. In contrast, MICP decreased exchangeable Cu by 62.5% and increased carbonate-bound Cu by 35.2%, validating the stabilization effect of microbially induced carbonate precipitation [30, 47]. Notably, the PMICP exhibited a clear synergistic effect, achieving an 86% decrease in exchangeable Cu and increasing the residual fraction to 43.8%. This synergistic enhancement likely involves initial Cu immobilization by peat through surface complexation, reducing its mobility, followed by the formation of stable organo-mineral associations during MICP-induced carbonate precipitation. Compared with other integrated MICP systems (e.g., CaO-MICP, which reduces exchangeable Cu by 71.2% via calcite lattice substitution and particle cementation), PMICP exhibits superior labile Cu immobilization efficiency [48].

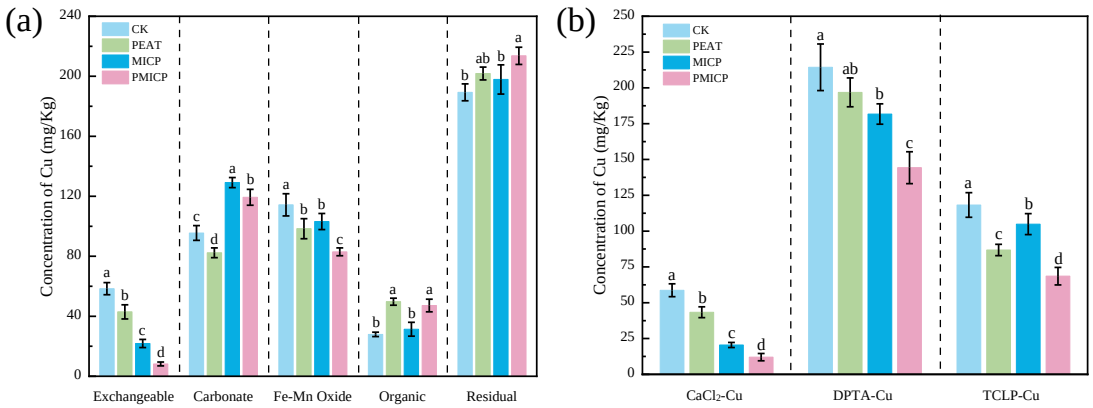

Figure 6.2 Characterization of copper in tailings from different treatment groups: (a) Chemical speciation distribution of Cu; (b) Extractable Cu concentrations by $CaCl_2$, DTPA, and TCLP methods.

The impacts of treatments on Cu bioavailability and acid leaching risks are illustrated in Figure 6.2 b. The CK group showed high levels of short-term bioavailability ($CaCl_2$-Cu: 58.69 ± 4.50 mg/kg), mid-to-long-term bioavailability (DTPA-Cu: 214.37 ± 16.28 mg/kg), and acid leaching risk (TCLP-Cu: 118.23 ± 8.60 mg/kg). PEAT treatment reduced $CaCl_2$-Cu and TCLP-Cu by 26.1% and 26.6%, respectively, but exhibited limited inhibitory effects on DTPA-Cu with a reduction of 8.2%, suggesting that organic-bound Cu remains partially extractable by strong chelators. MICP treatment reduced $CaCl_2$-Cu by 65.0% via carbonate coprecipitation,

yet its TCLP-Cu decreased only 11.3%, reflecting the instability of carbonate minerals under acidic conditions. In contrast, the PMICP treatment reduced $CaCl_2$-Cu, DTPA-Cu, and TCLP-Cu by 79.5%, 32.7%, and 42.0%, respectively. This combined approach integrates mineral-phase protection (inhibiting acidic dissolution) with organic-phase shielding (blocking chelator extraction), achieving long-term stabilization of Cu through synergistic interactions. These results demonstrate that the peat-MICP coupling strategy facilitates directional speciation transformation of Cu, enhances environmental resistance, and provides an innovative approach to mitigate risks in heavy metal-contaminated sites.

6.3.2 Changes in soil enzyme activity and nutrient cycling

The availability of nutrients and the composition of carbon pools varied significantly among treatments (Figure 6.3 a-b). Compared to CK, the MICP treatment reduced available phosphorus (AP) by 34.7% (to 2.05 ± 0.20 mg/kg), a decrease attributed to phosphate co-precipitation with carbonates. In contrast, the PMICP treatment mitigated this phosphorus fixation, showing only a 21.97% reduction in AP (2.45 ± 0.09 mg/kg). This alleviation is likely due to the chelation of metal ions by peat-derived organic acids, which inhibits phosphate precipitation [49]. Both PEAT and PMICP treatments increased available potassium (AK to 36.11 ± 0.85 and 35.28 ± 0.52 mg/kg, respectively), facilitated by peat organic acids that promote the release of mineral K [50].

Crucially, the PMICP treatment uniquely enhanced the overall carbon pools, overcoming the one-sided limitations of single amendments (Figure 6.3 c-i). While MICP solely increased the total inorganic carbon (TIC: 39.30 ± 0.97 g/kg) via carbonate precipitation, and peat (PEAT) primarily elevated organic carbon fractions (total organic carbon, TOC: 9.71 ± 0.16 g/kg; particulate organic carbon, POC: 2643.63 ± 78.42 mg/kg), PMICP synergistically combined these benefits. It significantly increased both TIC (39.11 ± 0.80 g/kg) and TOC (9.45 ± 0.21 g/kg) while maintaining a moderate level of POC (1004.74 ± 93.68 mg/kg). More importantly, PMICP promoted the formation of stable organo-mineral composites, yielding the highest mineral-associated organic carbon (MOC: 8441.92 ± 212.20 mg/kg, ~8.8-fold higher than CK) [51, 52]. Furthermore, it significantly boosted labile carbon substrates for microbial metabolism, as reflected in the 14.6-fold and 7.4-fold increases in dissolved organic carbon (DOC) and readily oxidizable organic carbon (LOC), respectively.

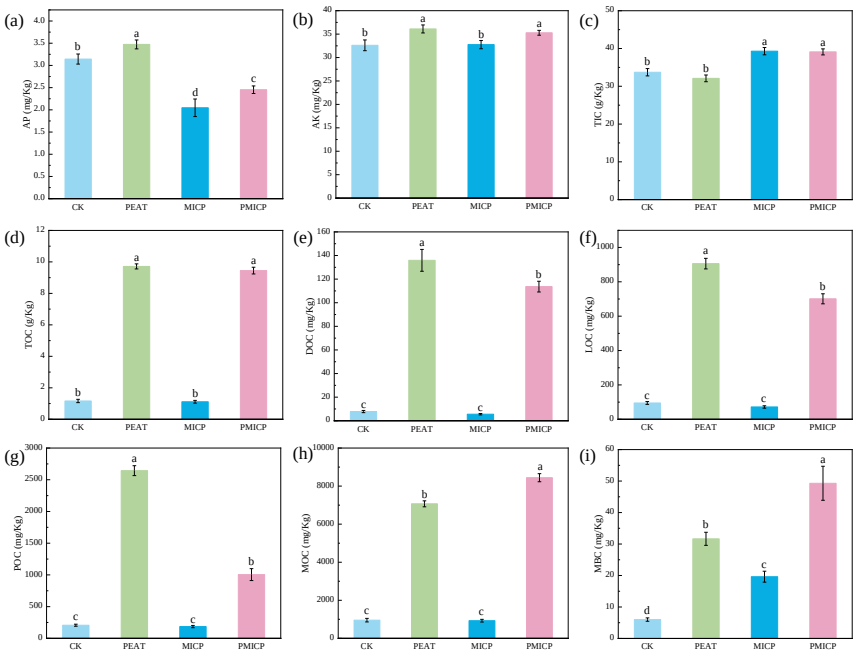

Figure 6.3 The effects of different treatments on (a) AP, (b) AK, (c) TIC, (d) TOC, (e) DOC, (f) LOC, (g) POC, (h) MOC, and (i) MBC.

This carbon enhancement was paralleled by a dramatic improvement in nitrogen retention (Figure 6.4). The total nitrogen (TN) content under PMICP reached 898.10 ± 32.91 mg/kg, an ~8-fold increase over CK and 84% higher than sole MICP. This synergy stems from peat's dual role: its functional groups (-COOH/-OH) adsorb ammonium (NH_4^+), and its buffering capacity moderates system pH to ~8.29 (vs. ~8.85 in MICP), mitigating ammonia volatilization [53]. The optimized habitat drove a 13-fold increase in microbial biomass nitrogen (MBN) and stimulated key enzyme activities (e.g., dehydrogenase +86%), enhancing nitrification and leading to 1.7-times higher nitrate (NO_3^--N) accumulation than in MICP [54]. Furthermore, the interaction of MICP-generated carbonates with peat organics elevated organic nitrogen (ON) immobilization by 189%, ensuring long-term stabilization [55]. Notably, the scale of fertility restoration achieved by PMICP (~8-fold increases in TN and TOC) greatly exceeds that reported for other composite MICP systems. For instance, a biochar-artificial humic acid-assisted MICP system achieved only 9.0-78.2% and 43.8-48.8% rises in TN and TOC, respectively [56]. This marked contrast underscores peat's outstanding ability to simultaneously enrich both nitrogen and carbon pools in highly impoverished tailings. The stable, balanced nutrient reservoir established by PMICP ensures long-term supply, fundamentally preventing the decline in remediation efficiency typically caused by nutrient depletion in such systems [27].

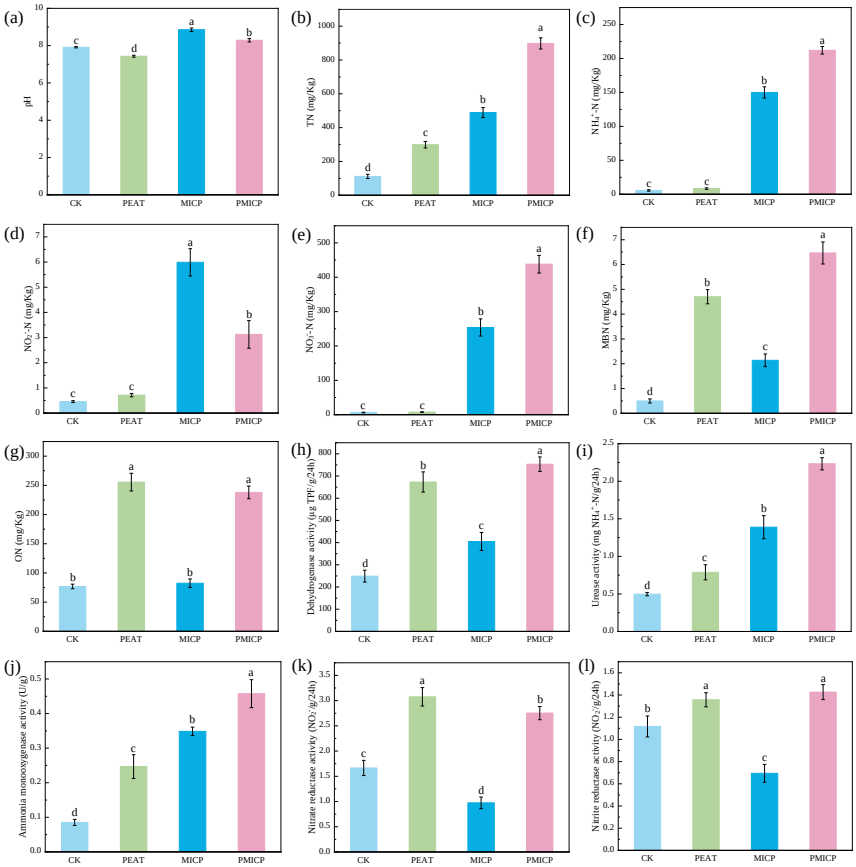

Figure 6.4 The effects of different treatments on (a) pH, (b) TN, (c)NH4+-N, (d) NO2--N, (e) NO3--N, (f) MBN, (g) ON, (h) Dehydrogenase activity, (i) Urease activity, (j) Ammonia monooxygenase activity, (k) Nitrate reductase activity, (l) Nitrite reductase activity.

Changes in carbon pools were accompanied by distinct shifts in dissolved organic matter (DOM) composition and sources, as revealed by 3D-EEM fluorescence spectroscopy and related indices (Figure 6.5, Table 6.5). In the CK, DOM exhibited low humification (Humification index, HIX = 1.32) and biological activity (Biological index, BIX = 0.55), primarily derived from recalcitrant mineral weathering residues and microbial debris, reflecting the inherent barrenness of the tailings environment [57]. In the PEAT, DOM is dominated by terrestrial humic substances (HIX = 2.52, Fluorescence index, FI = 1.26), and this type of DOM can immobilize Cu^{2+} through ion exchange and complexation [58]. In contrast, the MICP treatment was characterized by the proliferation of ureolytic bacteria, and its DOM pool showed high bioactivity (BIX = 0.78, FI = 1.92, Freshness index, FrI = 1.25), a signature of microbial-derived DOM produced by the metabolic activities of ureolytic bacteria [59, 60]. Notably, PMICP

created a dual-source DOM: peat humics (HIX = 2.13) provided Cu-binding sites, while bacterial bioactive fractions (FI = 1.48, BIX = 0.60) supplied labile carbon [33, 56]. This coupled Cu immobilization with microbial nutrition, underpinning PMICP's superior performance.

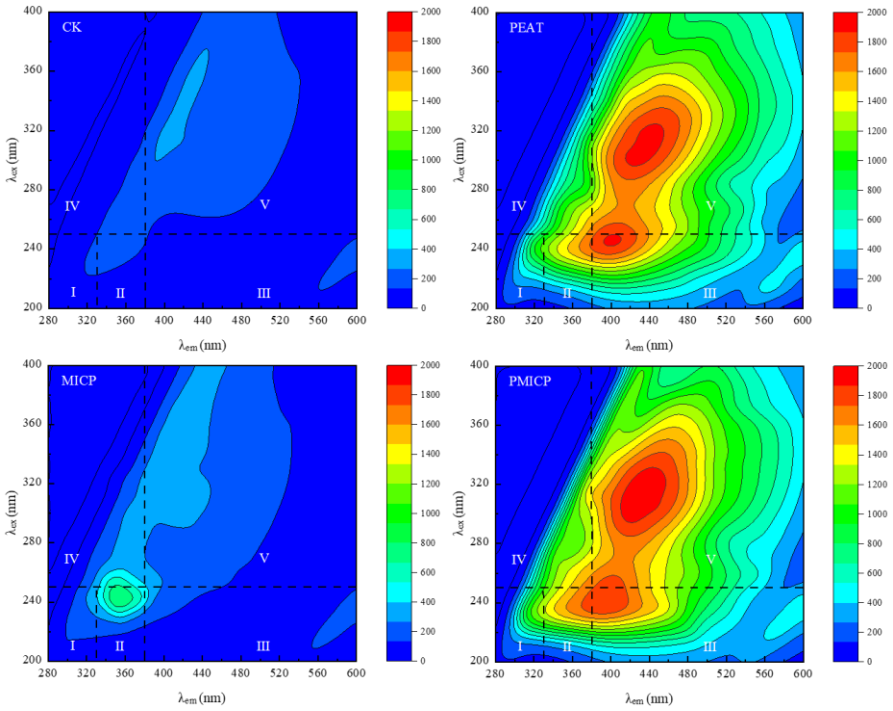

Figure 6.5 Three-dimensional excitation-emission matrix (3D-EEM) fluorescence spectroscopy of dissolved organic matter in tailings from different treatment groups: (a) CK, (b) PEAT, (c) MICP, (d) PMICP.

Table 6.5 Major three-dimensional fluorescence indices of dissolved organic matter (DOM).

Groups	FI	HIX	BIX	FrI
CK	1.31	1.32	0.55	0.59
PEAT	1.26	2.52	0.50	0.57
MICP	1.92	1.08	0.78	1.25
PMICP	1.48	2.13	0.60	0.69

To quantitatively examine the carbon-nitrogen coupling mechanism, redundancy analysis (RDA) and Pearson correlation analysis were performed (Figure 6.6-6.7). The first two RDA axes explained 94.9% of the constrained variance, with PMICP samples

clustering along vectors representing high levels of TN, NH_4^+-N, NO_3^--N, and enzyme activities—reflecting the synchronous optimization of nitrogen retention and microbial metabolism under moderated pH and ample organic carbon. Pearson correlation analysis further delineated key relationships within the carbon-nitrogen network: microbial biomass carbon (MBC) correlated strongly with TN ($r = 0.86$, $p < 0.001$) and NO_3^--N ($r = 0.69$, $p < 0.05$), while labile carbon fractions (DOC, LOC) were closely linked to microbial biomass nitrogen ($r = 0.87$-0.91, $p < 0.001$), supporting the role of peat-derived carbon in promoting microbial nitrogen assimilation. Moreover, key enzyme activities (urease, ammonia monooxygenase, dehydrogenase) showed tight associations with nitrogen species (TN, NH_4^+-N, NO_3^--N; $r = 0.69$-0.98, $p < 0.001$), indicating that carbon-enhanced microbial metabolism regulates nitrogen transformation through enzymatic pathways. Collectively, these results demonstrate that PMICP establishes an integrated "carbon supply-microbial activity-enzyme function" system that effectively enhances nitrogen retention and transformation.

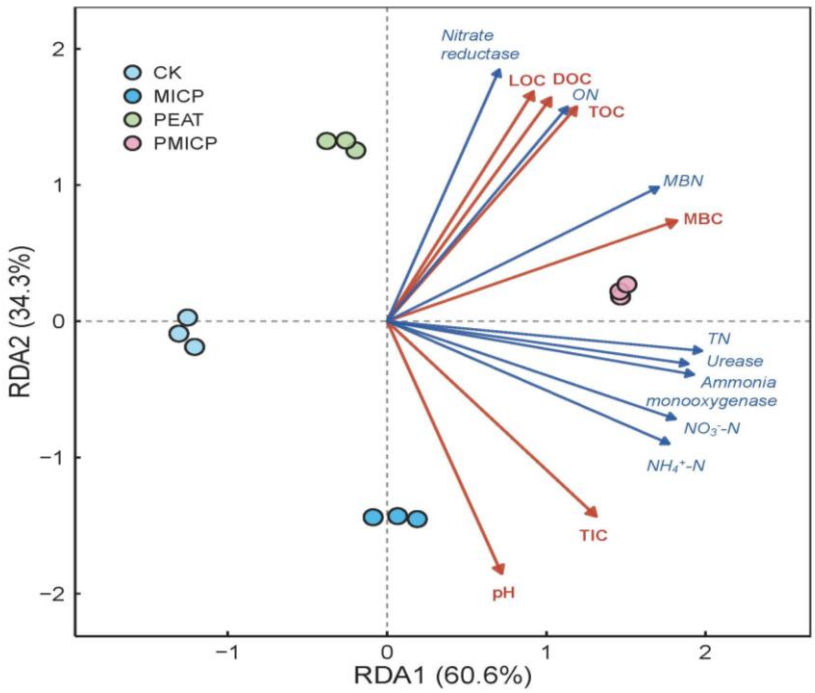

Figure 6.6 Redundancy analysis (RDA) showing the relationships among carbon pool components, enzyme activities, and nitrogen species under different remediation treatments.

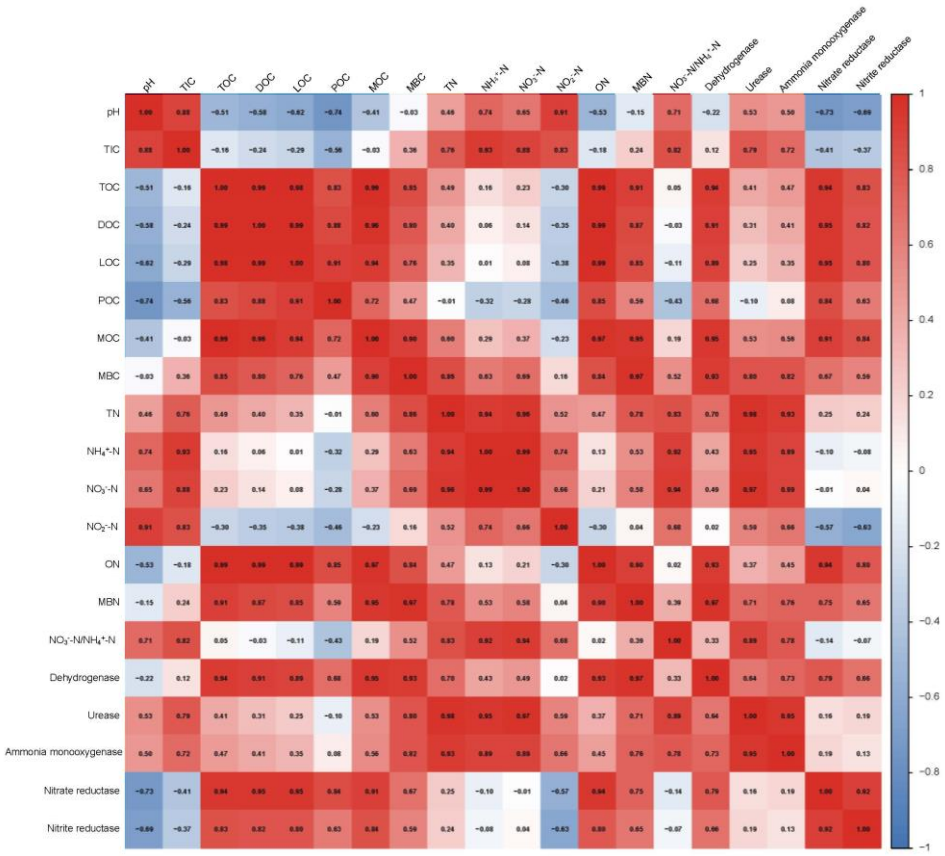

Figure 6.7 Pearson correlation heatmap illustrating the coupling between carbon fractions, microbial biomass, nitrogen forms, and enzyme activities.

6.3.3 Characterization of mineralized precipitates

SEM-EDS analyses revealed that different treatments significantly altered the microstructural and elemental distribution characteristics of the tailings (Figure 6.8). The CK group exhibited smooth-surfaced tailings particles with no cementation structure, along with dispersed and homogeneous Cu signals, reflecting its inherently unstable native structure and high Cu migration risk. In the PEAT group, partial decomposition and edge rounding of particles occurred due to the weak acidity of peat, with peat fibers filling interparticle gaps. Localized enrichment of Cu was observed, indicating that functional groups of peat organic matter facilitated Cu immobilization through adsorption and complexation. The MICP treatment resulted in the formation of abundant, yet discrete and dispersed carbonate precipitates. Although Cu signals remained relatively uniform, their overall intensity decreased, demonstrating that fixation was primarily achieved through co-precipitation with carbonates or lattice substitution [55]. Most importantly, the PMICP treatment facilitated the growth of large, cohesive organo-carbonate clusters. EDS mapping clearly demonstrated that Cu was

strongly enriched and co-localized with C and Ca specifically within these clusters, providing direct visual evidence of Cu sequestration via the “organic-mineral dual encapsulation” mechanism. Semi-quantitative elemental analysis (Figure 6.9) further supported this conclusion: the PMICP group exhibited significantly higher C and N content compared to the MICP group, while the Cu content was the lowest, fully validating its dual advantages of simultaneously enhancing nutrient retention and strengthening heavy metal immobilization. In summary, the PMICP technique combines peat organic matter with MICP-induced carbonate cementation to construct a stable composite system that integrates nutrient preservation and Cu immobilization, providing an effective technological approach for the ecological remediation of tailings reservoirs.

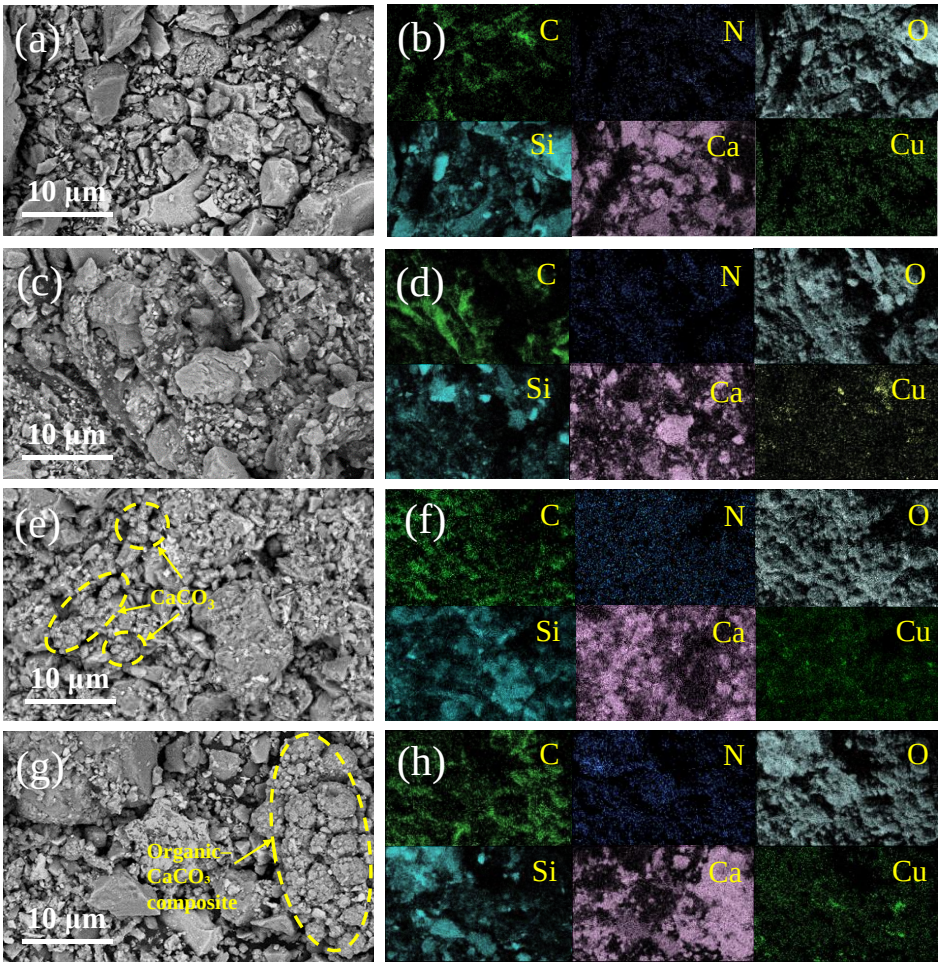

Figure 6.8 SEM images of mineralized precipitates from the (a) CK, (c) PEAT, (e) MICP, and (g) PMICP groups; The corresponding elemental mapping for the (b) CK, (d) PEAT, (f) MICP, and (h) PMICP groups.

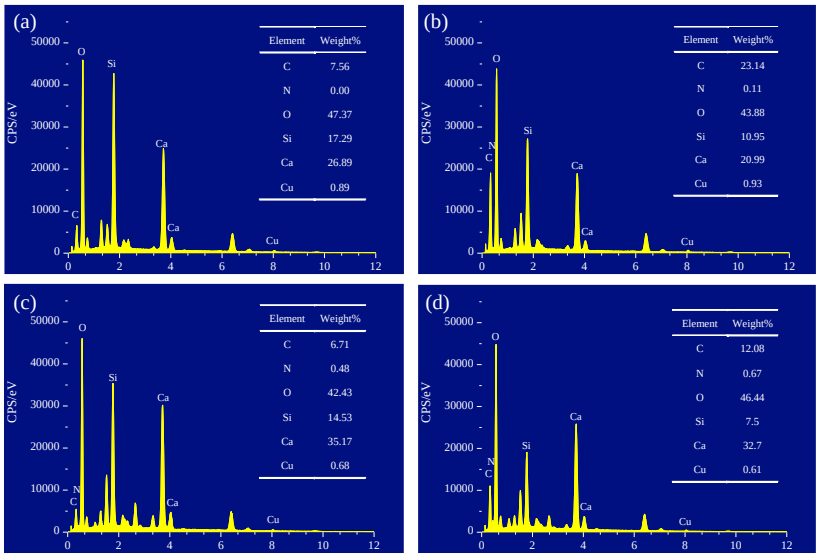

Figure 6.9 The corresponding EDS spectra of the (a) CK, (b) PEAT, (c) MICP, and (d) PMICP groups.

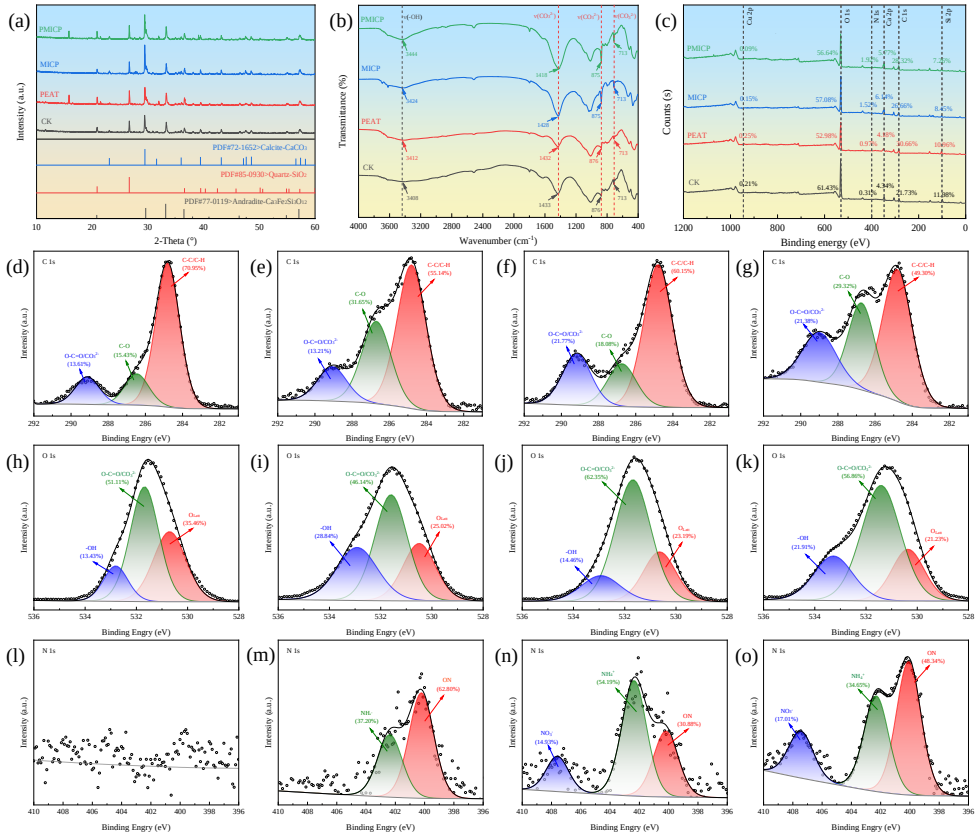

Figure 6.10 Mineralogical and surface chemical characterization of mineralized precipitates from different treatments. (a) X-ray diffraction (XRD) patterns and (b) Fourier transform infrared (FT-IR) spectra. (c) X-ray photoelectron spectroscopy (XPS) survey spectra. High-resolution XPS spectra of (d-g) C 1s, (h-k) O 1s, and (l-o) N 1s for CK, PEAT, MICP, and PMICP treatments, respectively.

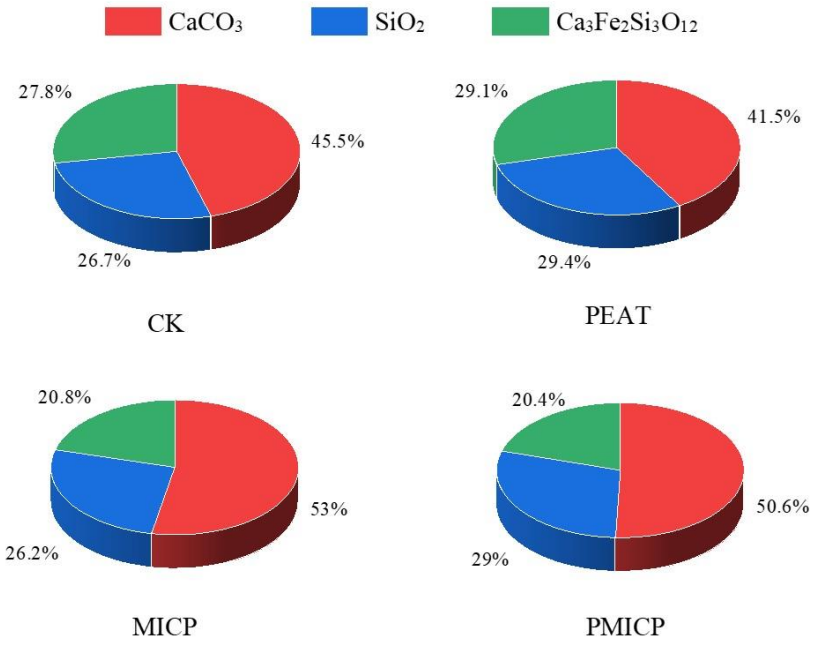

Figure 6.11 Semi-quantitative phase abundance analysis of quartz, andradite, and calcite in copper tailings from different treatment groups based on XRD Rietveld refinement.

Table 6.6 Calcite structural parameters (a, c, unit cell volume V) and discrepancy factor (R).

Groups	a (Å)	c (Å)	V (Å³)	R (%)
CK	4.9886(17)	17.0547(67)	367.86(51)	8.48
PEAT	4.9856(18)	17.0565(75)	367.69(56)	10.22
MICP	4.9876(15)	17.0614(61)	368.04(46)	10.59
PMICP	4.9875(16)	17.0574(63)	367.81(48)	10.76

XRD analysis (Figure 6.10 a) revealed clear differences in mineral composition among treatments. Raw tailings (CK) were mainly composed of quartz, andradite, and calcite. Compared with CK, both MICP and PMICP treatments showed a pronounced enhancement of the calcite diffraction peak at ~29.4° (2θ), indicating effective microbially induced calcium carbonate precipitation. Semi-quantitative analysis (Figure 6.11) showed calcite contents of 45.5% (CK), 41.5% (PEAT), 53.0% (MICP), and 50.6% (PMICP). The reduced calcite content in the PEAT group is attributable to the weak acidity of peat organic matter, whereas the slightly lower calcite content in PMICP relative to MICP may reflect the regulatory influence of peat-derived organic

matter. Previous studies indicate that carboxyl and phenolic hydroxyl groups can complex Ca^{2+}, reducing calcium availability, while organic adsorption on crystal surfaces inhibits ordered calcite growth and promotes partially amorphous precipitate formation [61]. Refinement of the calcite lattice parameters (Table 6.6) demonstrated high structural stability across all treatments, with unit cell dimensions (*a*, *c*) and volume (V) varying by less than 0.1%, indicating that Cu immobilization does not occur primarily through lattice substitution.

FT-IR spectroscopy (Figure 6.10 b) provided molecular-level evidence supporting the XRD observations. Compared with CK, the PEAT group showed attenuated carbonate-related bands at 1432 cm^{-1} (asymmetric stretching of CO_3^{2-}), 876 cm^{-1} (out-of-plane bending), and 713 cm^{-1} (in-plane bending), consistent with its reduced crystalline calcite content [62-64]. In contrast, the MICP group exhibited intensified peaks at these characteristic wavenumbers, in agreement with the formation of well-crystallized calcite (53.0%). Notably, the PMICP group displayed the strongest carbonate-related absorptions, despite a slightly lower crystalline calcite proportion than MICP, suggesting the presence of additional amorphous or poorly crystalline carbonate phases within organo-mineral composites. Further support is provided by the broadened and shifted O-H stretching band at 3444 cm^{-1} in PMICP, indicating enhanced hydrogen bonding between peat-derived organic functional groups and carbonate minerals [65, 66].

To gain deeper insights into the surface chemical state of elements and fine-scale molecular interactions underpinning organo-mineral composite formation, XPS analysis was conducted (Figure 6.10 c-o). Survey scans (Figure 6.10 c) confirmed that PMICP significantly increased surface C (21.73 at%→28.32 at%) and N (0.31 at%→1.92 at%) relative to CK—verifying peat organic matter introduction and nitrogen retention from MICP substrates and microbial metabolism—while reducing surface Cu to the lowest level (0.09 at%), confirming effective encapsulation. High-resolution XPS spectra (Figure 6.10 d-o) revealed distinct chemical states among treatments. In the C 1s region, peaks corresponding to C-C/C-H (~284.8 eV), C-O (~286.5-286.8 eV), and O-C=O/CO_3^{2-} (~288.9-289.2 eV) were identified. CK was dominated by inert C-C/C-H (70.95 at%). The PEAT treatment enriched oxygenated C-O (31.65 at%), reflecting peat-derived organic functional groups but with limited carbonate-related carbon. In contrast, MICP markedly increased O-C=O/CO_3^{2-} (21.77 at%) due to carbonate precipitation. Notably, PMICP exhibited a more balanced carbon distribution, with

reduced C-C/C-H (49.3 at%) together with concurrently high C-O (29.32 at%) and O-C=O/CO_3^{2-} (21.38 at%), directly reflecting the coupling of peat organic components with MICP-derived carbonates [67, 68]. Consistently, O 1s spectra showed that CK was dominated by lattice oxygen (Olatt), indicative of exposed mineral surfaces, whereas PEAT increased hydroxyl-related oxygen via organic inputs and MICP was characterized by abundant carbonate oxygen associated with calcite formation. PMICP combined relatively low Olatt with substantial carbonate and hydroxyl oxygen, indicating effective coverage of mineral surfaces by an organic-carbonate composite layer [69]. In the N 1s spectra, organic N, NH_4^+, and NO_3^- species were detected. MICP was dominated by NH_4^+ generated from urea hydrolysis, while PMICP retained higher organic N, moderated NH_4^+ levels, and increased NO_3^- content, consistent with peat-mediated NH_4^+ adsorption and pH buffering that favors nitrification [70, 71]. Overall, the combined SEM-EDS, XRD, FT-IR, and XPS analyses consistently demonstrate that PMICP assembles an integrated organic-carbonate composite system. This multiscale structure enables effective Cu encapsulation while simultaneously enhancing surface nutrient retention and ecological functionality.

6.3.4 Microbial community analysis

Microbial diversity analysis revealed that different remediation treatments significantly influenced the microbial community structure of copper tailings. The α-diversity results (Figure 6.12 a-d, Table 6.7) showed that the PEAT treatment achieved the highest values across all indices, indicating markedly greater community richness and species diversity compared with the CK and MICP groups. In contrast, the single MICP treatment, due to its strong alkalinity and reagent toxicity, further suppressed the already limited microbial community [28]. Notably, the PMICP treatment exhibited a pronounced regulatory effect, with all α-diversity indices significantly higher than those of the MICP group and intermediate between the PEAT and MICP groups, suggesting that peat effectively mitigated the adverse effects of MICP. This pattern was further supported by β-diversity analysis, where principal coordinate analysis (PCoA, Figure 6.13) showed distinct separation among groups (ANOSIM, $R^2 = 0.649$, $P = 0.001$). Importantly, the PMICP samples were positioned between the PEAT and MICP groups in the ordination space, indicating a transitional community configuration shaped by the combined influence of organic amendment and mineralization processes.

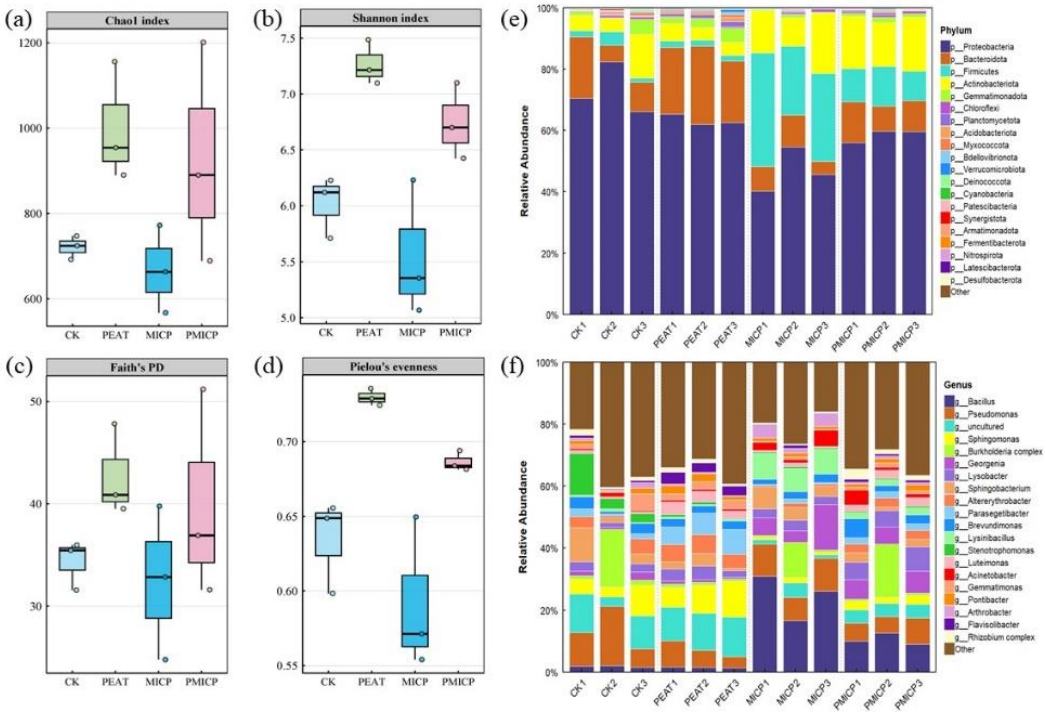

Figure 6.12 Alpha diversity and taxonomic abundance of bacterial communities across different treatment groups. The subfigures correspond to the (a) Chao1 index, (b) Shannon index, (c) Faith's PD, (d) Palou's evenness, (e) phylum-level relative abundance, and (f) genus-level relative abundance.

Based on microbial community analysis, PMICP synergistically enhanced functional activity and diversity through peat's regulation (Figure 6.12 e-f). At the phylum level, PMICP counteracted the structural imbalance induced by conventional MICP [28, 56]. It significantly reduced the over-proliferated *Firmicutes* (from 32.04% in MICP to 11.10%), a group enriched due to ureolytic activity, thereby preventing resource monopoly [72]. Concurrently, PMICP promoted the recovery of *Bacteroidota* (10.54%), essential for organic matter degradation, and *Actinobacteriota* (16.39%), beneficial for soil health [73]. Furthermore, it stabilized *Proteobacteria* at 58.44%, mitigating both its extreme dominance in CK (72.94%) and its sharp decline in MICP (46.84%), which collectively maintained overall community stability. At the genus level, PMICP achieved a "moderated functional community" by strategically regulating key bacterial groups. It controlled the abundance of core ureolytic bacteria, reducing *Bacillus* from 24.53% to 10.54% and *Lysinibacillus* from 7.93% to 2.08% [74]. Crucially, peat introduction activated and enriched specific functional genera: *Parasegetibacter*, involved in organic carbon metabolism, was nearly absent in MICP and increased to 2.02% in PMICP; *Sphingomonas*, which contributes to heavy-metal

detoxification via siderophore secretion, increased from 1.11% in MICP to 2.51% in PMICP; meanwhile, numerous uncultured indigenous taxa maintained moderate abundance, supporting functional diversity [75, 76]. The unique mechanism of PMICP lies in this peat-mediated balance: by limiting ureolytic overgrowth while enhancing functional taxa such as *Parasegetibacter* and *Sphingomonas*, it prevents excessive alkalinization and metabolic dominance, establishing a stable microbial system capable of efficient mineralization, metabolism, and detoxification.

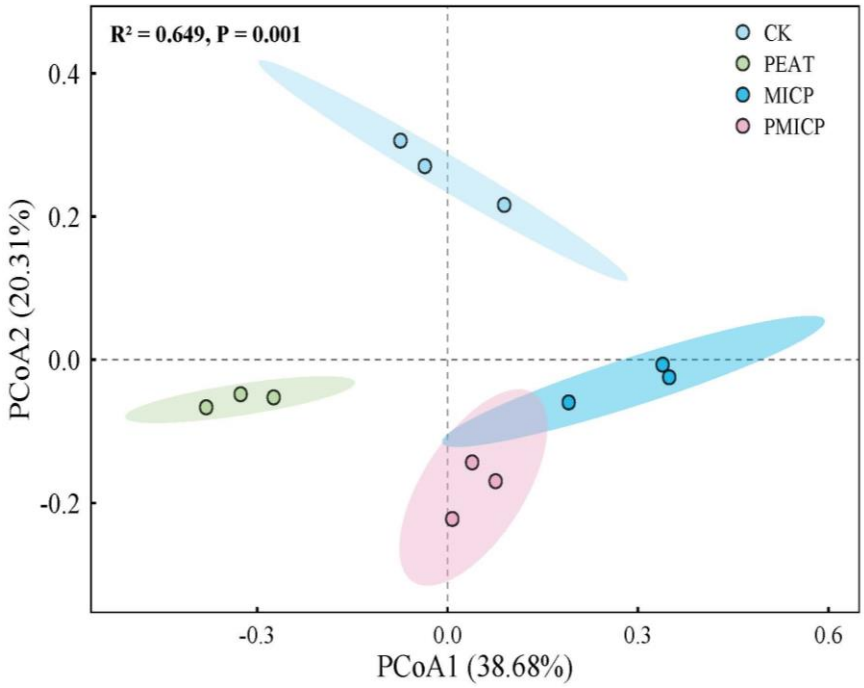

Figure 6.13 Principal coordinate analysis (PCoA) plot of bacterial community beta diversity across different treatment groups.

Table 6.7 Bacterial community indexes (diversity, richness, phylogenetic diversity, evenness) under different treatment groups (mean ± SD, n=3).

Groups	Chao1 index	Shannon index	Faith's PD	Pielou's evenness
CK	721.00±27.62ab	6.02±0.27bc	34.32±2.40b	0.63±0.03bc
PEAT	1000.00±138.84a	7.27±0.20a	42.73±4.45a	0.73±0.01a
MICP	667.33±102.57b	5.55±0.61c	32.45±7.51b	0.59±0.05c
PMICP	926.67±257.96ab	6.74±0.34ab	39.90±10.14a	0.69±0.01ab

To identify key discriminative taxa, linear discriminant analysis effect size (LEfSe) was performed (Figure 6.14). The CK group featured stress-tolerant taxa (e.g., *Proteobacteria*, *Enterobacterales*, *Massilia*), indicating survival-oriented communities [77, 78]. The MICP group displayed enrichment of ureolytic *Firmicutes* (including *Bacilli*, *Bacillus*, and *Lysinibacillus*), excluding indigenous microbes and simplifying community structure [28]. The PEAT group showed diverse peat endophytic biomarkers (*Bacteroidota*, *Sphingomonadales*, *Parasegetibacter*, and *Chitinophagales*-related taxa) that formed a multifunctional network for carbon decomposition, metal detoxification, and pH regulation [79]. Notably, PMICP exhibited the most distinct structure: retaining peat-associated *Pedobacter* for detoxification and carbon metabolism, preventing excessive *Firmicutes* proliferation as observed in MICP, and fostering unique core taxa including *Actinobacteriota*, *Micrococcales*, and *Lysobacter*. In summary, PEAT cultivated a multifunctional consortium via endophytes, MICP constrained microbial development by overemphasizing ureolysis, and PMICP—mediated by peat's "ecological engineers"—achieved an optimal balance between functional specialization and community stability for synergistic remediation.

Genus-level co-occurrence network analysis (Figure 6.15 and Table 6.8) delineated microbial interactions shaped by different treatments. CK formed a simple network (182 nodes, 6,639 edges; avg. degree 72.96; 57.09% positive). PEAT developed the largest and most stable network (268 nodes, 14,603 edges; modularity 0.6926; 50.83% positive), with peat endophytes serving as interaction hubs. In contrast, MICP produced the smallest, most fragmented network (166 nodes, 5,256 edges; avg. degree 63.33) yet paradoxically showed the highest positive interaction ratio (57.72%). This topology suggests a narrow, specialized consortium where strong internal cohesion may foster antagonism toward excluded taxa, a known risk to bioaugmentation efficiency [80]. Notably, PMICP constructed a balanced and integrated network (236 nodes, 11,102 edges; modularity 0.6425; 53.12% positive) [56]. Here, peat endophytes bridged functional and indigenous taxa, effectively mitigating antagonistic interactions and fostering a cooperative consortium, as sought in successful remediation designs [80, 81]. The progression from fragmented (MICP) to synergistic (PMICP) networks underscores peat's role in engineering stable microbial communities.

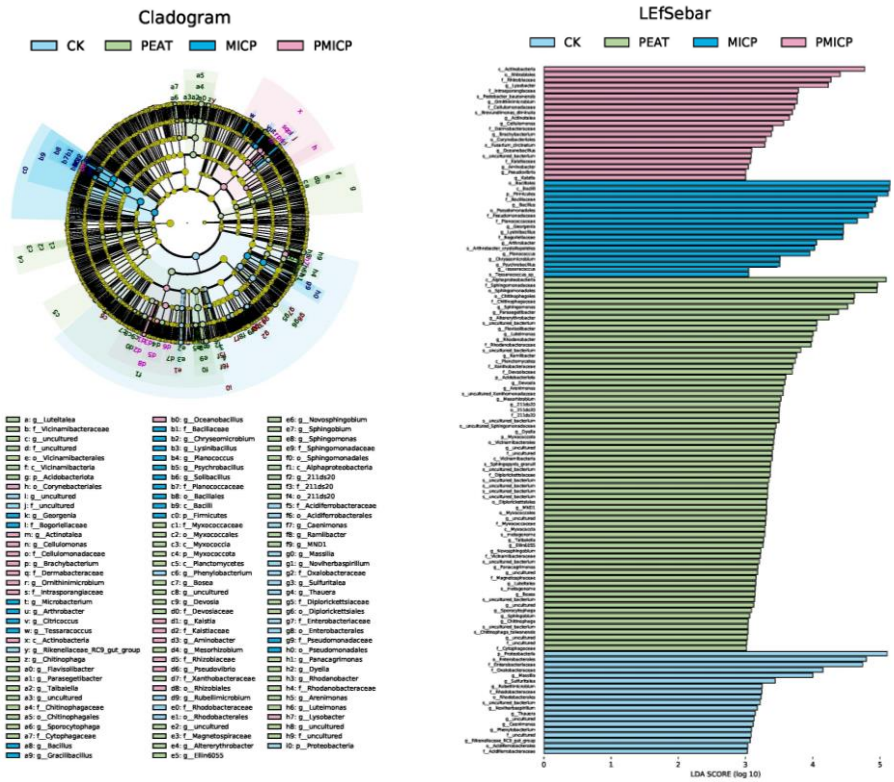

Figure 6.14 LEfSe analysis of bacterial community biomarkers distinguishing different treatment groups from phylum to genus level.

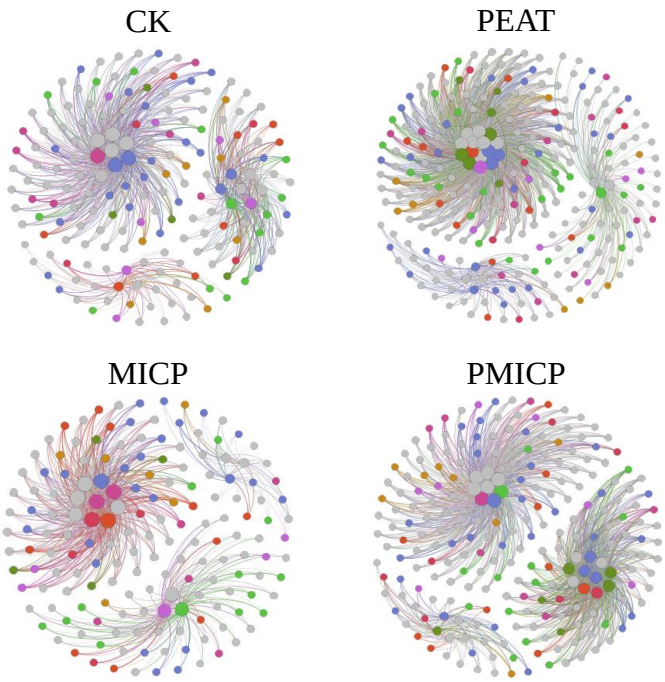

Figure 6.15 Network diagram of microbial communities within different treatment groups, at the Genus level.

Table 6.8 Topological coefficients of the microbial co-occurrence network across different treatment groups.

Groups	Positive Interaction (%)	Nodes	Edges	Average Degree	Modularity	Density
CK	57.09	182	6639	72.96	0.5548	0.4031
PEAT	50.83	268	14603	108.98	0.6926	0.4082
MICP	57.72	166	5256	63.33	0.6039	0.3838
PMICP	53.12	236	11102	94.08	0.6425	0.4004

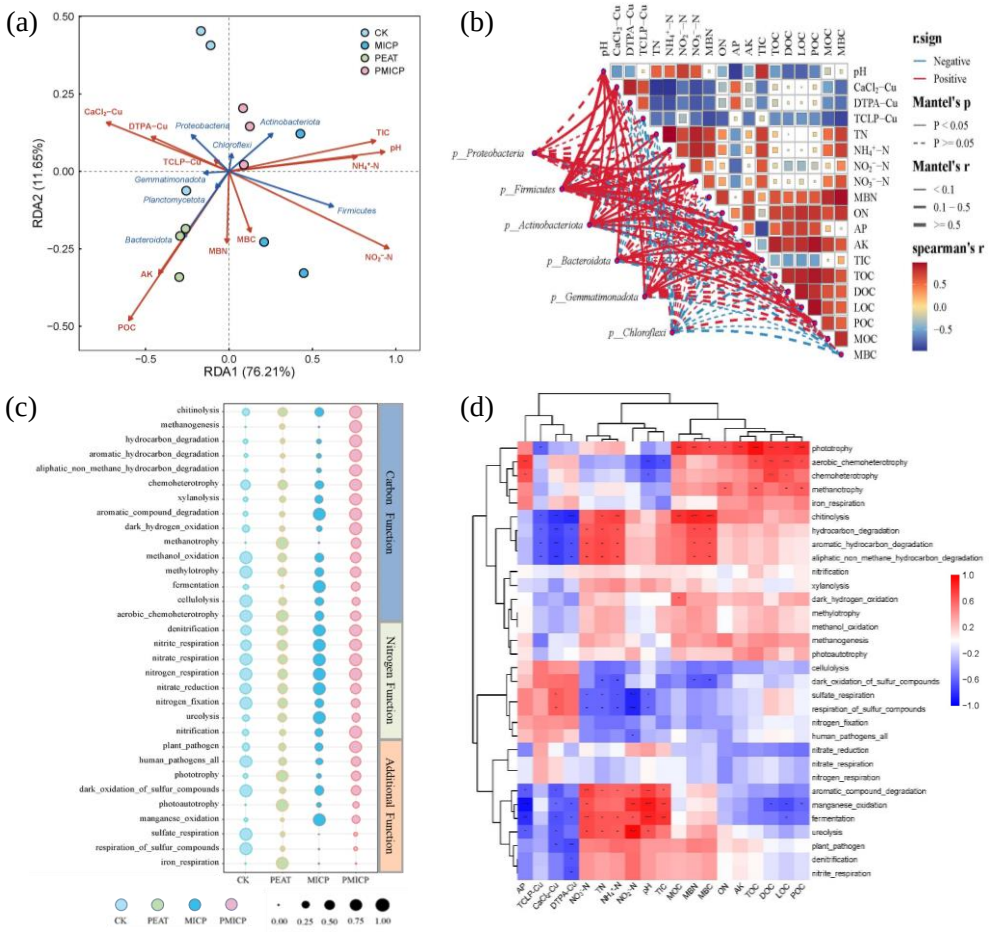

Figure 6.16 Integrative analysis of microbial community, functional pathways, and environmental factors: (a) Redundancy analysis (RDA) of microbial community and environmental factors; (b) Mantel test and Spearman correlation heatmap between microbial phyla and environmental factors; (c) Relative abundance of functional pathways across different treatments; (d) Correlation heatmap between functional pathways and environmental factors.

Redundancy analysis (RDA; Figure 6.16 a) revealed distinct environmental drivers of microbial community assembly across treatments, with the first two axes explaining 87.86% of total variation [35]. CK communities were strongly associated with elevated bioavailable Cu ($CaCl_2$-Cu, DTPA-Cu). The MICP treatment correlated with higher pH (RDA1 loading = 0.93) and TIC (RDA1 loading = 0.88), an environmental niche linked to the dominance of *Firmicutes* (mineralization). In contrast, PEAT was associated with increased POC (RDA1 loading = -0.60) and the prevalence of *Bacteroidota* (organic matter decomposition). Notably, PMICP samples occupied an intermediate position between the MICP and PEAT clusters, suggesting combined associations with both alkaline mineralizing conditions and organic carbon availability, corresponding to a more balanced consortium with complementary functions of mineralization (*Firmicutes*), organic matter decomposition (*Bacteroidota*), and nutrient cycling (*Actinobacteriota*). Complementary Mantel analysis (Figure 6.16 b) validated these phylum-environment couplings: MICP-driven pH/TIC showed strong positive associations with *Firmicutes* (Mantel's $r = 0.76$-0.82, $P < 0.001$). Meanwhile, AP and inorganic nitrogen species (NH_4^+-N, NO_2^--N, and NO_3^--N) correlated positively with *Actinobacteriota* ($r = 0.29$-0.52, $P < 0.05$), while AK associated with *Bacteroidota* ($r = 0.28$, $P < 0.05$). This confirms that treatments selectively regulate functional phyla, with PMICP's superiority deriving from balancing these groups, thereby reinforcing the coupling between contaminant immobilization and ecological recovery.

Building on the community structure data, FAPROTAX-based functional prediction uncovered distinct treatment-specific microbial metabolic patterns tightly linked to remediation mechanisms (Figure 6.16 c): MICP, centered on urea-driven carbonate precipitation for Cu immobilization, showed markedly enriched ureolysis; PEAT enhanced functions related to organic matter processing and carbon metabolism, such as chitinolysis and phototrophy; PMICP integrated the strengths of both treatments, retaining moderate ureolysis to maintain Cu immobilization capacity while achieving the highest chitinolysis (~2.9-fold higher than CK) and enhanced aromatic hydrocarbon degradation (~3.6-fold higher than CK), confirming that PMICP synergistically combines MICP's urea-mediated mineralization and PEAT's organic matter decomposition advantages to optimize both contaminant immobilization and ecological recovery. [82, 83]. Notably, all remediation treatments suppressed human pathogen genes compared to CK, concomitant with beneficial guild proliferation. Correlation

analysis (Figure 6.16 d) linked these treatment-specific functional shifts to distinct environmental drivers. Ureolysis, a core function for MICP's Cu immobilization, was strongly positively correlated with elevated pH ($r = 0.671$, $P < 0.05$) and NO_3^--N ($r = 0.706$, $P < 0.05$). Chitinolysis, a hallmark function of PEAT and PMICP for organic matter decomposition, showed a strong positive association with MBC ($r = 0.825$, $P < 0.001$) and a significant negative correlation with bioavailable $CaCl_2$-Cu ($r = -0.783$, $P < 0.01$). These results demonstrate that PMICP synergistically integrates two key regulatory drivers: Cu detoxification and organic carbon input via elevated MBC and substrate availability, which together promote nitrogen accumulation and enhance organic matter decomposition.

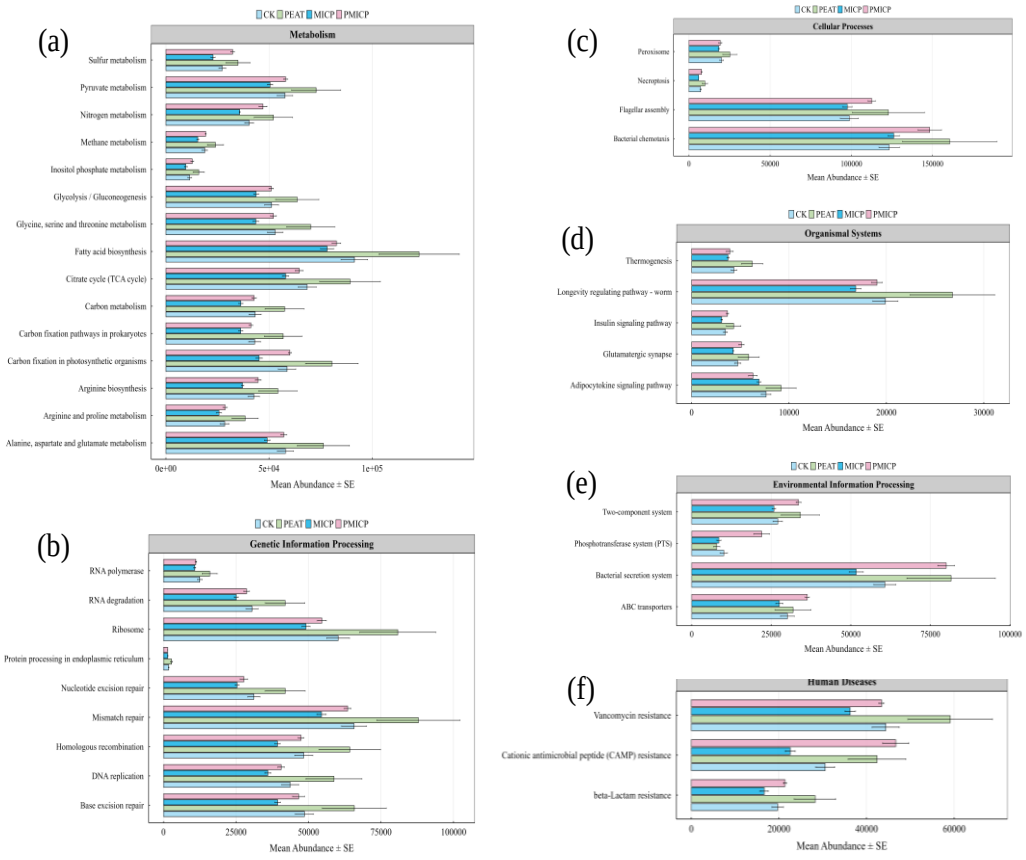

Figure 6.17 Predicted abundances of key microbial functional genes across treatments. Grouped bar plots display pathways in six categories: (a) Metabolism, (b) Genetic Information Processing, (c) Cellular Processes, (d) Organismal Systems, (e) Environmental Information Processing, and (f) Human Diseases. Error bars represent standard error (SE).

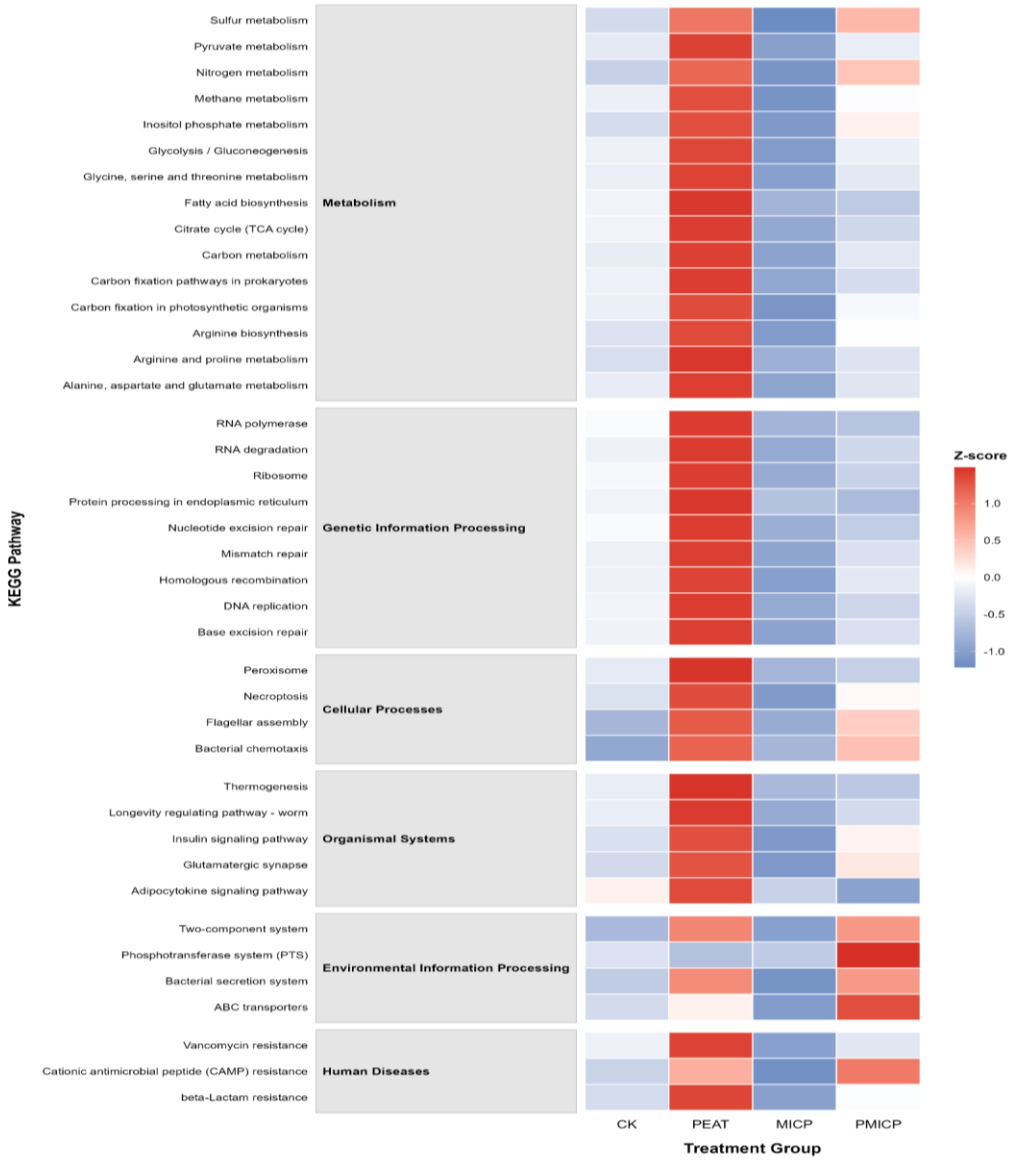

Figure 6.18 Heatmap clustering of microbial functional profiles reveals the integrated network in PMICP. The heatmap presents Z-score normalized abundances of KEGG pathways across six functional categories for each treatment.

To elucidate the underpinning metabolic mechanisms and identify the core functional pathways driving these synergistic outcomes, we conducted KEGG pathway analysis using PICRUSt2 (Figure 6.17-6.18). The PEAT treatment broadly upregulated core metabolic functions (e.g., glycolysis/gluconeogenesis, Z = 1.36; TCA cycle, Z = 1.42), aligning with its FAPROTAX-predicted shift toward heterotrophic carbon metabolism. In contrast, the MICP treatment induced a widespread suppression of nutrient metabolic pathways (nitrogen metabolism, Z = -1.12; sulfur metabolism, Z = -1.21), consistent with its failure to improve tailing fertility. Crucially, the PMICP

treatment not only mitigated MICP's metabolic suppression—restoring nitrogen metabolism to a positive Z-score (0.45) via peat's nutrient supply—but also uniquely enriched pathways for cationic antimicrobial peptide (CAMP) resistance (Z = 1.01) and the phosphotransferase system (PTS, Z = 1.49). This metabolic profile indicates that PMICP fosters a microbial consortium equipped with dual stress resistance (including to Cu) and enhanced nutrient competitive uptake capabilities. These integrated metabolic traits provide a mechanistic foundation for PMICP's superior performance in achieving simultaneous contaminant immobilization and ecological recovery.

6.3.5 Field-scale Validation of Ecological Restoration

Field-scale observations over 12 months revealed clear differences in ryegrass establishment, physiological performance, and metal uptake among treatments (Figure 6.19 a-e). PMICP plots exhibited the densest and most uniform ryegrass coverage, whereas CK and MICP plots showed sparse and discontinuous growth, with intermediate performance in PEAT plots (Figure 6.19 a). Quantitative results confirmed this pattern: PMICP achieved the highest fresh biomass, with shoot and root biomass reaching 2025.13 ± 87.06 g/m² and 653.19 ± 30.68 g/m², respectively, substantially exceeding those of CK, PEAT, and MICP. Chlorophyll a and b contents were markedly enhanced under PMICP (15.85 ± 1.44 and 4.15 ± 0.88 mg/L), accompanied by the lowest catalase (CAT) activity (80.05 ± 10.41 U/(g·min)), indicating alleviated oxidative stress. PMICP also significantly reduced Cu accumulation in plant tissues, with shoot and root Cu concentrations decreasing to 12.00 ± 3.29 and 71.8 ± 19.2 mg/kg dry weight, respectively, representing reductions of more than 70% relative to CK. Overall, PMICP simultaneously promoted plant growth and suppressed Cu uptake by reducing rhizosphere Cu bioavailability.

Consistent with these plant responses, soil Cu speciation further confirmed the long-term immobilization stability of PMICP (Figure 6.19 f-h). After 3 months, exchangeable Cu declined to 11.58 ± 2.02 mg/kg, accompanied by a shift toward carbonate-bound (110.55 ± 7.30 mg/kg) and residual (223.95 ± 7.51 mg/kg) fractions. At 5 months, corresponding to the first ryegrass harvest, exchangeable Cu remained low (14.19 ± 4.33 mg/kg), indicating negligible remobilization during intensive plant growth. After 12 months, PMICP maintained the most stable Cu partitioning, with exchangeable Cu stabilized at 13.19 ± 3.26 mg/kg, while organic-bound (64.1 ± 5.6 mg/kg) and residual (248.1 ± 2.8 mg/kg) fractions dominated. In contrast, CK and

single-treatment plots consistently exhibited higher proportions of bioavailable Cu, confirming that peat-assisted MICP enables durable Cu immobilization and sustained ecological recovery under realistic field conditions.

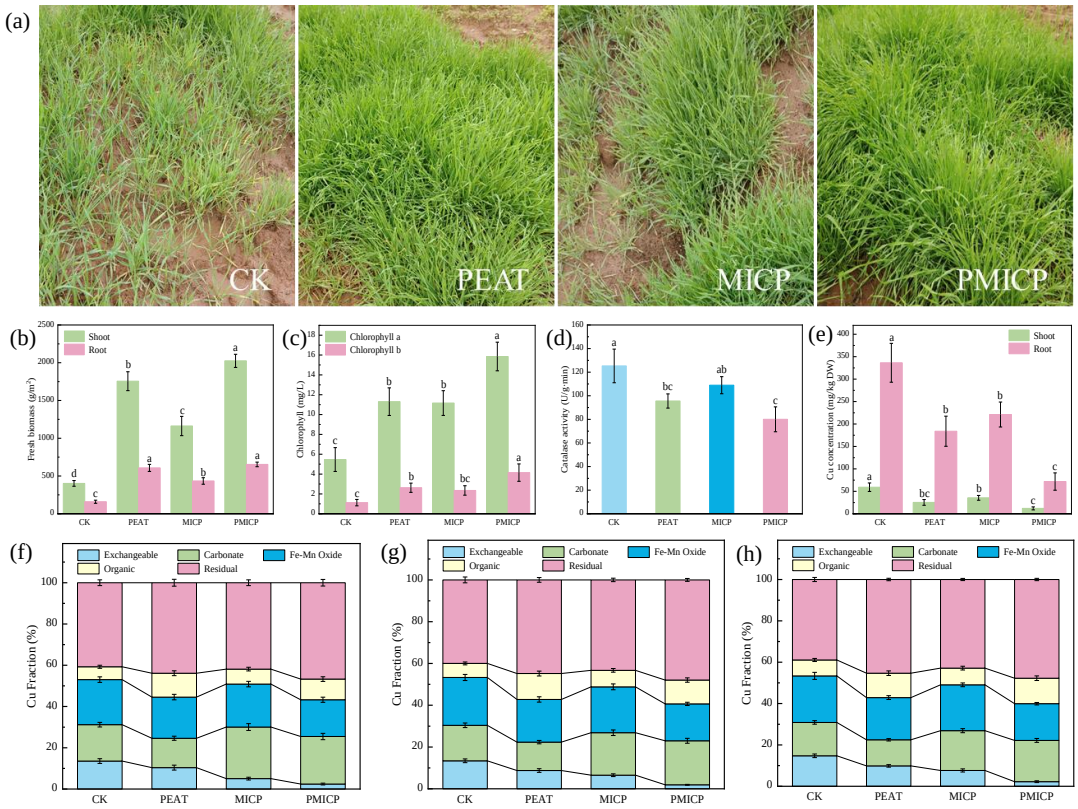

Figure 6.19 The effects of different treatments on (a) Vegetation growth status, (b) Plant biomass (shoot and root), (c) Chlorophyll a and b contents, (d) Catalase activity, (e) Cu accumulation in plant (shoot and root), (f) Cu fractions in tailings (March), (g) Cu fractions in tailings (May), (h) Cu fractions in tailings (December).

6.4 Conclusions

In conclusion, this study developed a peat-assisted microbially induced carbonate precipitation (PMICP) technology, achieving long-term copper stabilization and restoration of tailings ecosystem functions. Compared with raw tailings (CK), PMICP reduced exchangeable Cu, $CaCl_2$-Cu, DTPA-Cu, and TCLP-Cu by 86%, 79.5%, 32.7%, and 42.0%, respectively, while promoting the transformation of Cu into stable organic-bound and residual forms. PMICP also markedly enhanced tailings nutrient status, with total nitrogen and total organic carbon increasing approximately 8-fold, providing a stable nutritional foundation for microbial metabolism and plant growth. The synergistic mechanism involves the formation of an "organic-mineral dual

encapsulation" structure by peat and MICP-generated carbonates, effectively stabilizing Cu, while peat's buffering effect facilitates the restructuring of indigenous microbial communities, suppressing overdominance of functional taxa and promoting recovery of diversity and nutrient cycling networks. A 12-month field-scale validation showed that PMICP treatment reduced Cu accumulation in plants by more than 70% and increased biomass to 4.3-fold that of CK, achieving a synergistic effect of "pollution containment-vegetation restoration". This study overcomes the limitations of conventional remediation technologies that "stabilize metals but sacrifice ecology", advancing tailings management from "single detoxification" to "systematic ecological restoration", and provides a theoretical and technical basis for green and sustainable remediation of heavy metal-contaminated sites. Future research could employ multi-omics approaches to further elucidate key microbial functions and in-situ regulatory networks within this system.

References

[1] C. Beldjani, N. Belghar, K. Aoues, M.S.M. Saleh, Y. Boutera, M.A. Kethiri, Efficiency improvement of air-cooled photovoltaic modules utilizing copper heat dissipators, Desalin. Water Treat., 279 (2022) 140-146.

[2] C. Qi, Q. Wu, C.J. Lin, H.T. Yan, Z.Y. Liu, Comparison of thermal runaway and gas production behavior between copper-based/hard carbon sodium ion battery and Lithium-iron phosphate/graphite lithium-ion battery, Journal of Energy Storage, 132 (2025).

[3] L.S. Wei, H.X. Xu, J. Wu, C.L. Shen, X. Sun, A review of research progress on the resource utilization of copper tailing, Journal of Environmental Chemical Engineering, 13 (2025).

[4] Y.Q. Song, Y.T. Chen, Z.S. Fu, Y. Wen, W.Y. Zhao, J. Li, H.C. Wang, Y.K. Du, Y. Deng, Heavy metal exposure and cognitive impairment: An umbrella review of meta-analyses, Journal of Hazardous Materials, 498 (2025).

[5] M. Stepien, D.J. Hughes, S. Hybsier, C. Bamia, A. Tjonneland, K. Overvad, A. Affret, M. His, M.C. Boutron-Ruault, V. Katzke, T. Kühn, K. Aleksandrova, A. Trichopoulou, P. Lagiou, P. Orfanos, D. Palli, S. Sieri, R. Tumino, F. Ricceri, S. Panico, H.B. Bueno-de-Mesquita, P.H. Peeters, E. Weiderpass, C. Lasheras, C.B. Bonet, E. Molina-Portillo, M. Dorronsoro, J.M. Huerta, A. Barricarte, B. Ohlsson, K. Sjöberg, M. Werner, D. Shungin, N. Wareham, K.T. Khaw, R.C. Travis, H. Freisling, A.J. Cross, L.

Schomburg, M. Jenab, Circulating copper and zinc levels and risk of hepatobiliary cancers in Europeans, British Journal of Cancer, 116 (2017) 688-696.

[6] R.E. Frye, J. Cakir, S. Rose, L. Delhey, S.C. Bennuri, M. Tippett, R.F. Palmer, C. Austin, P. Curtin, M. Arora, Early life metal exposure dysregulates cellular bioenergetics in children with regressive autism spectrum disorder, Translational Psychiatry, 10 (2020).

[7] Z.X. Wang, J.W. Pan, Z.J. Lu, L. Xia, S.X. Song, Y. Hu, Y.T. Li, Microcoleus vaginatus: A novel amendment for constructing artificial soil from tailings, Environmental Technology & Innovation, 37 (2025).

[8] T. Jia, X.X. Liang, T.Y. Guo, T.H. Wu, B.F. Chai, Bacterial community succession and influencing factors for Imperata cylindrica litter decomposition in a copper tailings area of China, Sci. Total Environ., 815 (2022) 14.

[9] D. Rosa, F. Rizzo, L. Di Palma, Lime and pozzolan-based matrices for an efficient immobilization of hazardous waste, Chemical Engineering Science, 313 (2025).

[10] A.Y. Al-Bakri, H.M. Ahmed, M.A. Hefni, Experimental Investigation of Recycling Cement Kiln Dust (CKD) as a Co-Binder Material in Cemented Paste Backfill (CPB) Made with Copper Tailings, Minerals, 14 (2024) 25.

[11] T. Lu, Z.A. Wei, M.H. El Naggar, W.S. Wang, Y.H. Yang, X. Tian, H.W. Guo, Effect of chemical environment on copper tailings reinforced by microbially induced carbonate precipitation, Constr. Build. Mater., 400 (2023) 12.

[12] B. Kang, F.S. Zha, H.C. Li, L. Xu, X.G. Sun, Z.T. Lu, Bio-Mediated Method for Immobilizing Copper Tailings Sand Contaminated with Multiple Heavy Metals, Crystals, 12 (2022) 13.

[13] X.S. Hu, B.H. He, Y.C. Liu, S.Y. Ma, C.H. Yu, Genomic characterization of a novel ureolytic bacteria, Lysinibacillus capsici TSBLM, and its application to the remediation of acidic heavy metal-contaminated soil, Sci. Total Environ., 927 (2024) 12.

[14] D.O. Owolabi, M. Shokouhian, I. Ahmad, M. Jenkins, G.L. McLemore, Comparative Analysis of Autogenous and Microbial-Based Calcite Precipitation in Concrete: State-of-the-Art Review, Buildings, 15 (2025).

[15] X.W. Wang, S.X. Zhang, K. Chen, Enhanced biogeochemical remediation of Pb-contaminated loess via MICP integrated with graphene nanomaterials, Rsc Advances, 15 (2025) 29063-29076.

[16] Y. Zeng, Z.Z. Chen, Q.Y. Lyu, X.X. Wang, Y.L. Du, C.C. Huan, Y. Liu, Z.Y. Yan, Mechanism of microbiologically induced calcite precipitation for cadmium

mineralization, Sci. Total Environ., 852 (2022) 10.
[17] C.Y. Tang, J. Yao, X.Y. Liu, K. Masakorala, Y. Lv, J.L. Liu, Y. Cao, Research progress in utilization of microbial immobilization technology in microbially induced mineralization of heavy metals, Journal of Environmental Chemical Engineering, 12 (2024) 15.
[18] M. Li, J. Liu, D. Cao, X.Y. Chen, J.X. Shi, W.Z. Hu, C.Q. Xiao, Y. Fang, Heavy metal pollution simplifies microbial networks and enhances modularity during tailings primary succession: divergent assembly dynamics for bacterial and fungal communities, Frontiers in Microbiology, 16 (2025).
[19] V. Velianyk, M. Palusak, N.H.A. Nguyen, J. Riha, A. Sevcu, M. Cernik, V. Hlavackova, Microbial diversity at remediated former gold and copper mines and the metal tolerance of indigenous microbial strains, Applied and Environmental Microbiology, (2025).
[20] J.M. Yue, N.P. Song, C. Meng, L. Xie, D.Q. Chang, An Experimental Study to Improve the Nutrients and the Mechanical Properties of Copper Tailings Sand in China's Arid Zone by Biomineralization of Locally Isolated Urease-Producing Bacteria, Sustainability, 15 (2023).
[21] Y.M. Lai, J. Yu, S.Y. Liu, J.F. Liu, R.K. Wang, B.W. Dong, Experimental study to improve the mechanical properties of iron tailings sand by using MICP at low pH, Constr. Build. Mater., 273 (2021) 14.
[22] C.H. Jia, Y.K. Fan, Q.Q. Wei, L.J. Wang, W.J. Zhang, Soil organic matter enhances urease-mediated microbially induced carbonate precipitation: Dual benefits for inorganic carbon sequestration and cadmium immobilization, Journal of Hazardous Materials, 496 (2025) 10.
[23] L.L. Zheng, T.T. Yin, Y.R. Lu, H. Lin, Y.B. Dong, Changing patterns of tailings physicochemical properties, community structure, and functional genes during cadmium biomineralization in tailings by carbonate-mineralized bacteria, Process Safety and Environmental Protection, 197 (2025).
[24] D.H. Peng, S.Y. Qiao, Y. Luo, H. Ma, L. Zhang, S.Y. Hou, B. Wu, H. Xu, Performance of microbial induced carbonate precipitation for immobilizing Cd in water and soil, Journal of Hazardous Materials, 400 (2020) 10.
[25] Y.F. Wang, J. Xu, S.H. Dong, L.R. Li, S.L. Wang, Effects of biochar and magnesium oxide on cadmium immobilized by microbially induced carbonate: Mobilization or immobilization in alkaline agricultural soils?, Environmental Pollution,

358 (2024).
[26] Y.Z. Liu, K.J. Hu, M.L. Pan, W. Dong, X.J. Wang, X.Y. Zhu, Research and Application of Green Technology Based on Microbially Induced Carbonate Precipitation (MICP) in Mining: A Review, Sustainability, 17 (2025).
[27] Z.F. Xue, W.C. Cheng, L. Wang, Y.X. Xie, P. Qin, Effect of a harsh circular environment on self-healing microbial-induced calcium carbonate materials for preventing Pb2+migration, Environmental Technology & Innovation, 32 (2023).
[28] M. Xu, J. Ma, X.H. Zhang, G. Yang, L.L. Long, C. Chen, C. Song, J. Wu, P. Gao, D.X. Guan, Biochar-bacteria partnership based on microbially induced calcite precipitation improves Cd immobilization and soil function, Biochar, 5 (2023).
[29] L. Zhang, W.J. Wang, C.L. Yue, Y.B. Si, Biogenic calcium improved Cd2+and Pb2+immobilization in soil using the ureolytic bacteria Bacillus pasteurii, Sci. Total Environ., 921 (2024).
[30] Y. Wang, P. Zhu, X.X. Li, C. Liu, Immobilization of multiple heavy metals in contaminated soil using multi-walled carbon nanotubes enhanced MICP, Chemical Engineering Journal, 522 (2025).
[31] N. Sánchez, I. Merbach, S. Drabesch, E. Blagodatskaya, F. Jamoteau, M. Keiluweit, J. Bachelder, M. Tarkka, E.M. Muehe, Bioavailability and phyto-extractability of metals in a peat-amended agricultural soil under climate stress, Journal of Environmental Management, 394 (2025).
[32] I. Rijk, A. Ekblad, A.S. Dahlin, A. Enell, M. Larsson, P. Leroy, D.B. Kleja, C. Tiberg, S. Hallin, C. Jones, Biochar and peat amendments affect nitrogen retention, microbial capacity and nitrogen cycling microbial communities in a metal and polycyclic aromatic hydrocarbon contaminated urban soil, Sci. Total Environ., 936 (2024).
[33] P. Talukdar, S. Sengupta, A. Nandi, S. Sultana, S. Das, S. Mohanta, M. Karmakar, Role of Peat Moss (Sphagnum) in Reduction of Environmental Toxicity in Correlation with Various Microbes, Applied Biochemistry and Biotechnology, (2025).
[34] L. Li, Y. Chen, C.D. Yang, F. Chen, L. Chen, Y. Hu, C.X. Wu, X.Y. Huang, Organic fertilization enhances soil bacterial community function, but has minor effects on bacterial community diversity in mine desert soils, Environmental Earth Sciences, 84 (2025).
[35] X.Z. Wang, Z. Zhou, Z.J. Lu, L. Xia, S.X. Song, J.V.G. Meza, M.L. Montes, J.B. Li, Surge of native rare taxa in tailings soil induced by peat bacterial invasion, Sci. Total

Environ., 908 (2024).
[36] Q. Chen, B. Zhao, Y.H. Zhang, F.F. Zhu, H. Wang, J.W. Wang, X.M. Fu, The function of "Cambi® thermal hydrolysis plus anaerobic digestion" on heavy metal behavior and risks in a full-scale sludge treatment plant based on four seasons investigation, Journal of Hazardous Materials, 445 (2023).
[37] Z. Zhang, K. Zhou, Z. Lu, J.V. Garcia-Meza, Z. Wu, L. Xia, X. Hu, Yeast extract as a double-edged sword in microbial induced carbonate precipitation for copper remediation: Unraveling the nutrient - ligand dilemma, Process Safety and Environmental Protection, 203 (2025) 108028.
[38] X.Y. Zhang, K. Wang, C.C. Sun, K.Q. Yang, J.Y. Zheng, Differences in soil physical properties caused by applying three organic amendments to loamy clay soil under field conditions, Journal of Soils and Sediments, 22 (2022) 43-55.
[39] M.V. Slukovskaya, I.P. Kremenetskaya, I.A. Mosendz, T.K. Ivanova, S. Drogobuzhskaya, L.A. Ivanova, A. Novikov, A.A. Shirokaya, Thermally activated serpentine materials as soil additives for copper and nickel immobilization in highly polluted peat, Environmental Geochemistry and Health, 45 (2023) 67-83.
[40] G.S. Ji, C.C. Huan, Y. Zeng, Q. Lyu, Y.L. Du, Y. Liu, L.S. Xu, Y. He, X.P. Tian, Z.Y. Yan, Microbiologically induced calcite precipitation (MICP) in situ remediated heavy metal contamination in sludge nutrient soil, Journal of Hazardous Materials, 473 (2024).
[41] M. Rizwan, G. Murtaza, Z. Ahmed, Q.M. Lin, X.J. Chen, I. Khan, H. Abdelrahman, V. Antoniadis, E.F. Ali, S.S. Lee, L.J. Leng, S.M. Shaheen, H.L. Li, Synergistic effect of biochar and intercropping on lead phytoavailability in the rhizosphere of a vegetable-grass system, Sci. Total Environ., 954 (2024).
[42] T. Ramesh, N.S. Bolan, M.B. Kirkham, H. Wijesekara, M. Kanchikerimath, C.S. Rao, S. Sandeep, J. Rinklebe, Y.S. Ok, B.U. Choudhury, H.L. Wang, C.X. Tang, X.J. Wang, Z.L. Song, O.W. Freeman, Soil organic carbon dynamics: Impact of land use changes and management practices: A review, in: D.L. Sparks (Ed.) Advances in Agronomy, Vol 156, 2019, pp. 1-107.
[43] Z.R. Chen, J.L. Liu, H.J. Sun, Effects of Forest Types on Soil Available Nutrients and Carbon Contents in Coastal Areas, China, Phyton-International Journal of Experimental Botany, 93 (2024) 2557-2569.
[44] W.D. Wang, M.T. Zhu, C.X. Zou, T.T. Zhang, J.H. Han, Z.Y. Wang, Biosurfactant type and introduction order impact the morphology of biological CaCO3 during the

MICP process, World Journal of Microbiology & Biotechnology, 41 (2025).
[45] Z. Zhou, L. Xia, X.Z. Wang, C.Y. Wu, J.Z. Liu, J.B. Li, Z.J. Lu, S.X. Song, J. Zhu, M.L. Montes, M. Benzaazoua, Coal slime as a good modifier for the restoration of copper tailings with improved soil properties and microbial function, Environmental Science and Pollution Research, 30 (2023) 109266-109282.
[46] Z.J. Lu, H.S. Wang, Z.X. Wang, J.Z. Liu, Y.T. Li, L. Xia, S.X. Song, Critical steps in the restoration of coal mine soils: Microbial-accelerated soil reconstruction, Journal of Environmental Management, 368 (2024).
[47] C. Comadran-Casas, C. Unluer, A.M. Bass, J. Macdonald, E.K. Najafi, L. Spruzeniece, C. Gauchotte-Lindsay, Bioremediation of multiple heavy metals through biostimulation of microbial-induced calcite precipitation at varying calcium-to-urea concentrations, Journal of Hazardous Materials, 491 (2025).
[48] Z.F. He, Y.T. Xu, W.Y. Wang, X.L. Yang, Z.Z. Jin, D.Y. Zhang, X.L. Pan, Synergistic mechanism and application of microbially induced carbonate precipitation (MICP) and inorganic additives for passivation of heavy metals in copper-nickel tailings, Chemosphere, 311 (2023).
[49] Z.W. Wang, Z.Y. Zhang, J. Peng, Y.X. Zhang, F. Zhou, J.X. Yu, R. Chi, C.Q. Xiao, Magnesium polypeptide combined with microbially induced calcite precipitation for remediation of lead contamination in phosphate mining wasteland soil, Environmental Research, 262 (2024).
[50] Q. Fan, J.Y. Yu, J. Feng, H.Y. Wu, Y. Jiu, X.F. Wu, Q. Zhang, Z. Xu, Z.Z. Xu, Enhancing passion fruit (Passiflora edulis f. flavicarpa Degener) agriculture with application of alkaline humic acid fertilizer and chemical fertilizer: A effective approach to soil and fruit quality optimization, Environmental Technology & Innovation, 39 (2025).
[51] X.L. Dou, J.B. Zhang, C.Z. Zhang, D.H. Ma, L. Chen, G.X. Zhou, J.W. Li, Y. Duan, Calcium carbonate regulates soil organic carbon accumulation by mediating microbial communities in northern China, Catena, 231 (2023).
[52] K.Q. Yang, J. Hu, Y.Z. Ren, Z. Zhang, M. Tang, Z.K. Shang, Q. Zhen, J.Y. Zheng, Enhancement of Soil Organic Carbon, Water Use Efficiency and Maize Yield (Zea mays L.) in Sandy Soil through Organic Amendment (Grass Peat) Incorporation, Agronomy-Basel, 14 (2024).
[53] C. Gan, Y.B. Jiang, Y. Wang, S. Lin, Y. Luo, H.B. Li, Y.W. Li, N.N. Tang, Y. Fei, R.G. Hu, Organic fertilizer application reduce ammonia volatilization in an acidic soil,

Agriculture Ecosystems & Environment, 383 (2025).
[54] M. Tomaszewski, G. Cema, A. Ziembinska-Buczynska, Influence of temperature and pH on the anammox process: A review and meta-analysis, Chemosphere, 182 (2017) 203-214.
[55] Y.X. Zhu, S.Y. Shan, T.D. Hu, L. He, H.J. Zhou, Hierarchical pore carbon-calcium nanocages for highly effective removal of ammonium-nitrogen and phosphorus, Fuel Processing Technology, 247 (2023).
[56] Y. Li, M.L. Zhang, X.B. Wang, S. Ai, X.H. Meng, Z.Q. Liu, F. Yang, K. Cheng, Synergistic enhancement of cadmium immobilization and soil fertility through biochar and artificial humic acid-assisted microbial-induced calcium carbonate precipitation, Journal of Hazardous Materials, 476 (2024).
[57] Y.L. Wang, C.M. Yang, L.M. Zou, H.Z. Cui, Spatial Distribution and Fluorescence Properties of Soil Dissolved Organic Carbon Across a Riparian Buffer Wetland in Chongming Island, China, Pedosphere, 25 (2015) 220-229.
[58] M. Izqulerdo, P. Marzal, C. Gabaldón, M. Silvetti, P. Castaldi, Study of the Interaction Mechanism in the Biosorption of Copper(II) Ions onto Posidonia oceanica and Peat, Clean-Soil Air Water, 40 (2012) 428-437.
[59] G. Zhou, Z.Y. Zhao, G.Q. Zhang, X. Gao, M.J. Wang, B. Wei, X. Chen, J.H. Li, L. Li, Enhanced mineralization and dust suppression mechanism of Bacillus pasteurii synergized with Bacillus mucilaginosus capable of CO2 capture effect, Chemical Engineering Journal, 520 (2025).
[60] L.F. Zhang, Z. Wang, J.F. Su, A. Ali, X. Li, Mechanisms of ammonia, calcium and heavy metal removal from nutrient-poor water by Acinetobacter calcoaceticus strain HM12, Journal of Environmental Management, 351 (2024).
[61] M.D. Huang, X.C. Zheng, X. He, X.S. Lin, J. Ye, Paenibacillus mucilaginosus-induced CO2 fixation into amorphous and crystalline carbonate minerals, Process Biochemistry, 157 (2025) 242-255.
[62] T.T. Zhu, L.L. Xu, Z.L. Wu, L.J. Yang, Z.L. Song, A novel marine biomineralization bacterium Exiguobacterium sp. 9-2: Inducing calcium carbonate precipitation with ferric ion-mediated facilitation, Journal of Environmental Chemical Engineering, 13 (2025).
[63] Q. Cai, W.D. Zhao, J.P. Wang, G. Yang, R. Amils, J.M. Martínez, G. Mateos, I. Carrasco-Ropero, J. Wu, M. Xu, A cooperation mechanism between Bacillus thuringiensis and Citrobacter freundii that enhances cadmium biomineralization,

Journal of Hazardous Materials, 488 (2025).
[64] Y.T. Duan, L. Niu, Y. He, K.N. Lei, X. Xu, C.L. Zheng, H.Q. Xiao, Effectiveness and mechanism of cyanide tailings cementation by steel slag coupled with non-ureolytic microbially induced carbonate precipitation, Process Safety and Environmental Protection, 190 (2024) 162-172.
[65] H. Gandhi, U. Beladiya, M. Poriya, J. Vaghela, V. Mevada, R. Patel, C. Kothari, Carbon capture and sequestration through landfill-derived Bacillus strains: Enhanced microbially induced calcite precipitation for sustainable bio-brick production, Constr. Build. Mater., 491 (2025).
[66] Y.L. An, X.L. Li, L. Liu, J.J. Liu, Y. Yu, J.H. Zhang, Z.K. Tong, Remediation mechanism of Sporosarcina pasteurii XL-1 for removal of Cr(VI) and Cr(III) by induced carbonate precipitation, Biochemical Engineering Journal, 225 (2026).
[67] L.L. Wang, J.Q. Yao, X.M. Liu, J.J. Liu, Z.A. Ma, X.Y. Chen, C.L. Cao, R.P. Li, J.H. Jiang, Ureolytic Nocardia tenerifensis-driven carbonate precipitation for enhanced La3+adsorption and immobilization, Journal of Cleaner Production, 482 (2024).
[68] Y.R. Dong, Z.Q. Gao, J.Z. Di, D. Wang, Z.H. Yang, Y.F. Wang, X.Y. Guo, K.F. Li, Experimental study on solidification and remediation of lead-zinc tailings based on microbially induced calcium carbonate precipitation (MICP), Constr. Build. Mater., 369 (2023).
[69] H.W. Song, J.Q. Sha, S.H. Wei, J. An, Low nitrogen MICP remediation of Pb contaminated water by multifunctional microbiome UN-1, Environmental Technology & Innovation, 38 (2025).
[70] J.V. dos Santos, A.I. Goranov, L.G. Fregolente, M.C. Bisinoti, Z.H. Sun, K. Schmidt-Rohr, P.G. Hatcher, Deciphering the Chemistry of Condensed Aromatic "Black" Carbon and Nitrogen in Amazonian Anthrosols, Environmental Science & Technology, 59 (2025) 17047-17058.
[71] J. Baltrusaitis, P.M. Jayaweera, V.H. Grassian, XPS study of nitrogen dioxide adsorption on metal oxide particle surfaces under different environmental conditions, Physical Chemistry Chemical Physics, 11 (2009) 8295-8305.
[72] T.T. Yin, H. Lin, Y.B. Dong, B. Li, Y.H. He, C.J. Liu, X. Chen, A novel constructed carbonate-mineralized functional bacterial consortium for high-efficiency cadmium biomineralization, Journal of Hazardous Materials, 401 (2021).
[73] X.S. Hu, X.X. Liu, L.K. Qiao, S. Zhang, K.W. Su, Z.L. Qiu, X.H. Li, Q.C. Zhao, C.H. Yu, Study on the spatial distribution of ureolytic microorganisms in farmland soil

around tailings with different heavy metal pollution, Sci. Total Environ., 775 (2021).
[74] S. Koner, J.S. Chen, B.M. Hsu, J. Rathod, S.W. Huang, H.Y. Chien, B. Hussain, M.W.Y. Chan, Depth-resolved microbial diversity and functional profiles of trichloroethylene-contaminated soils for Biolog EcoPlate-based biostimulation strategy, Journal of Hazardous Materials, 424 (2022).
[75] M.P. Doane, C.J. Johnson, S. Johri, E.N. Kerr, M.M. Morris, R. Desantiago, A.C. Turnlund, A. Goodman, M. Mora, L.F.O. Lima, A.P. Nosal, E.A. Dinsdale, The Epidermal Microbiome Within an Aggregation of Leopard Sharks (Triakis semifasciata) Has Taxonomic Flexibility with Gene Functional Stability Across Three Time-points, Microbial Ecology, 85 (2023) 747-764.
[76] S.W. Zhang, J.L. Cao, J. Xu, X.L. Pan, F.S. Dong, Y.Q. Zheng, X.H. Wu, Organic Fertilization Mitigates Long-Acting Herbicide Mesosulfuron-Methyl Effects via Rhizosphere Soil Bacterial Community Regulation in Wheat, Journal of Agricultural and Food Chemistry, (2025).
[77] E. Anedda, D. Ekhlas, E. Alexa, M.L. Farrell, M.T. Gaffney, G. Madigan, D. Morris, C.M. Burgess, Characterization of antimicrobial resistant Enterobacterales isolated from spinach and soil following zinc amendment, Environmental Pollution, 361 (2024).
[78] K. Amirhosseini, M. Alizadeh, H. Azarbad, Harnessing the Ecological and Genomic Adaptability of the Bacterial Genus Massilia for Environmental and Industrial Applications, Microbial Biotechnology, 18 (2025).
[79] M. Liu, H.Q. Hu, M.S. Islam, X.F. Rao, J. Zhu, L.C. Fang, Q.L. Fu, How to balance cadmium immobilization and greenhouse gas emissions when using microbial induced-calcite precipitation (MICP): Regulate the N/ Ca molar ratio and dosage, Journal of Environmental Chemical Engineering, 13 (2025).
[80] Y.X. Xie, W.C. Cheng, Z.F. Xue, L. Wang, M.M. Rahman, Degradation of naphthalene in aqueous solution using a microbial symbiotic system founded by degrading and ureolytic bacteria, Environmental Research, 268 (2025).
[81] Y.X. Xie, W.C. Cheng, Z.F. Xue, L. Wang, P.F. Zhang, Removal of naphthalene from aqueous solution using bacteria-loaded carrier materials, Separation and Purification Technology, 377 (2025).
[82] C. Sansupa, S.F.M. Wahdan, S. Hossen, T. Disayathanoowat, T. Wubet, W. Purahong, Can We Use Functional Annotation of Prokaryotic Taxa (FAPROTAX) to Assign the Ecological Functions of Soil Bacteria?, Applied Sciences-Basel, 11 (2021).

[83] Z.C. Yang, C.Y. Peng, H.M. Cao, J.J. Song, B. Gong, L. Li, L. Wang, Y. He, M. Liang, J.C. Lin, L.L. Lu, Microbial functional assemblages predicted by the FAPROTAX analysis are impacted by physicochemical properties, but C, N and S cycling genes are not in mangrove soil in the Beibu Gulf, China, Ecological Indicators, 139 (2022).

Chapter VII. Conclusions

This study enhanced MICP for heavy metal remediation via additive engineering, establishing a four-dimensional framework covering bioactivity maintenance, mineralization control, byproduct mitigation, and ecological recovery. The synergistic effects of four functional additives were revealed:

(1) Yeast extract exhibits a nutrient-ligand trade-off in MICP. Low concentrations promote microbial growth and copper immobilization, while excessive doses chelate metal ions and reduce biomineralization efficiency. An optimal dosage balances growth support and mineralization inhibition under copper stress.

(2) Montmorillonite-composite microcapsules provide physical shielding for functional microorganisms. They alleviate heavy metal toxicity, improve microbial survival, and enhance lead immobilization through combined adsorption and biomineralization, offering an effective strategy for bioactivity protection.

(4) The peat-integrated MICP system couples heavy metal immobilization with ecological restoration. Peat improves soil structure, supplies nutrients, buffers alkaline stress, and mitigates byproduct risks. The system stabilizes heavy metals, reconstructs microbial communities, and restores soil fertility, transforming remediated sites into self-sustaining ecosystems.

Overall, additive engineering effectively addresses the core limitations of conventional MICP, enabling synergistic improvements in microbial activity, mineralization control, environmental safety, and ecological compatibility. Nevertheless, limitations remain: optimal dosages are site-specific and require case-by-case calibration; long-term metal stability under extreme environmental stresses (e.g., acid rain, freeze-thaw) is untested beyond 12 months of field monitoring; polystyrene nanoplastics themselves are pollutants and their introduction risks secondary contamination that must be carefully managed; and economic feasibility for large-scale application is still unassessed. Future work should focus on pilot-scale validation, accelerated aging tests, life-cycle assessment, and site-specific optimization using machine learning or response surface methodology.

Appendix I

Articles published in international journals during the PhD study

1. **Zijia Zhang**, Qingwei Zhang, **J. Viridiana Garcia-Meza**, Zhenbin Wu, Delong Meng, Ling Xia*. Synergistic Effects of Peat and MICP for Copper Tailings Remediation: Metal Immobilization, Nutrient Retention, and Microbial Regulation. **Journal of Hazardous Materials**, 2026, 502, 141028. **(IF=11.3)**
2. **Zijia Zhang**, Keqiang Zhou, **J. Viridiana Garcia-Meza**, Zhenbin Wu, Ling Xia*, Xiheng Hu*. Yeast extract as a double-edged sword in microbial induced carbonate precipitation for copper remediation: Unraveling the nutrient - ligand dilemma. **Process Safety and Environmental Protection**, 2025, 203, 108028. **(IF=7.8)**
3. **Zijia Zhang,** Keqiang Zhou, Yujing Bi*, **J. Viridiana Garcia-Meza**, Li Wu, Zhenbin Wu, Ling Xia*. From surface interception to biological stabilization: successional controls on lead immobilization and microbial resilience in biocrusts. **Environmental Pollution**, 2026, 398, 128055. **(IF=7.3)**
4. **Zijia Zhang**, Keqiang Zhou, **J. Viridiana Garcia-Meza**, Shaoxian Song, Ling Xia*. Montmorillonite Reinforced Polyvinyl Alcohol/Sodium Alginate/Chlorella FK Microcapsules for Repair of Lead (II). **Applied Clay Science**, 2025, 273. **(IF=5.8)**
5. **Zijia Zhang**, Zhen Wang, Jiaqi Tan, Keqiang Zhou, **J. Viridiana Garcia-Meza**, Shaoxian Song, Ling Xia*. Yeast-derived biochar to load CoFe2O4: Degradation of tetracycline hydrochloride by heterogeneous activation of peroxymonosulfate. **Journal of Environmental Chemical Engineering**, 2023, 11(3). **(IF=7.2)**
6. Xu Liu, Wenlu Xue, **Zijia Zhang***, Wei Zhou, Shaoxian Song, Yinta Li, Mostafa Benzaazoua, Xiheng Hu. Effect of cobalt isomorphic substitution on the properties of goethite and the adsorption of lead. **Frontiers in Environmental Science**, 2023, 11, 1186147. **(IF=3.7)**
7. **Zijia Zhang,** Keqiang Zhou, Yujing Bi, **J. Viridiana Garcia-Meza,** Zhenbin Wu, Ling Xia*. From Pollutant to Partner: Functional Roles of Polystyrene Nanoplastics in Microbial Carbonate Mineralization and Copper Remediation. **(Submitted)**
8. Yujing Bi, Keqiang Zhou, J. Viridiana Garcia-Meza, **Zijia Zhang***, Li Wu, Zhenbin Wu, Ling Xia*. Montmorillonite–cyanobacteria interactions drive soil surface structuring and early pedogenic processes in lead-contaminated sandy substrates. **(Submitted)**

Appendix II

Experimental datas

Table II. 1 Growth curves (OD_{600}) at different yeast extract concentrations.

Time (h）	0	4	8	12	24	36	48
0 g/L	0.031	0.029	0.03	0.026	0.019	0.023	0.018
	0.029	0.031	0.028	0.023	0.021	0.025	0.022
	0.028	0.032	0.025	0.027	0.022	0.024	0.019
0.5 g/L	0.033	0.046	0.382	0.598	0.729	0.773	0.787
	0.029	0.043	0.353	0.567	0.684	0.722	0.728
	0.03	0.039	0.324	0.522	0.692	0.728	0.802
1.0 g/L	0.034	0.052	0.564	0.933	1.423	1.678	1.646
	0.031	0.049	0.515	0.928	1.445	1.654	1.621
	0.032	0.056	0.547	0.992	1.453	1.697	1.699
1.5 g/L	0.032	0.054	0.724	1.082	1.589	1.762	1.722
	0.028	0.058	0.746	1.123	1.521	1.754	1.721
	0.032	0.061	0.752	1.097	1.563	1.715	1.687
2.0 g/L	0.035	0.06	0.807	1.225	1.653	1.714	1.698
	0.032	0.067	0.804	1.128	1.629	1.688	1.715
	0.033	0.063	0.842	1.188	1.633	1.698	1.714
3.0 g/L	0.034	0.079	0.826	1.138	1.316	1.297	1.208
	0.032	0.082	0.845	1.194	1.384	1.325	1.304
	0.029	0.084	0.837	1.229	1.298	1.348	1.333

Table II. 2 OD_{600} of SX1 after 48 h culture with 0–8 mM Cu^{2+} and 0.5–3.0 g/L yeast extract.

Cu^{2+} concentration	0 mM	0.1 mM	0.5 mM	1.0 mM	2.0 mM	4.0 mM	6.0 mM	8.0 mM
0.5 g/L	0.787	0.844	0.822	0.633	0.233	0.008	0.008	0.009
	0.728	0.839	0.789	0.589	0.287	0.009	0.012	0.007
	0.802	0.887	0.809	0.574	0.193	0.012	0.014	0.012
1.0 g/L	1.646	1.524	1.833	1.657	1.438	0.833	0.109	0.012
	1.621	1.656	1.825	1.679	1.475	0.854	0.182	0.007
	1.699	1.673	1.834	1.649	1.444	0.837	0.138	0.018
1.5 g/L	1.722	1.732	1.837	1.784	1.687	1.334	0.837	0.125

	1.721	1.722	1.772	1.802	1.668	1.357	0.777	0.132
	1.687	1.709	1.897	1.822	1.603	1.282	0.738	0.186
2.0 g/L	1.698	1.724	1.899	1.833	1.777	1.554	1.066	0.343
	1.715	1.733	1.902	1.795	1.698	1.609	1.145	0.354
	1.714	1.745	1.924	1.784	1.712	1.588	0.977	0.254
3.0 g/L	1.208	1.313	1.332	1.357	1.288	1.221	0.887	0.345
	1.304	1.421	1.312	1.335	1.364	1.184	0.875	0.332
	1.333	1.357	1.245	1.409	1.308	1.168	0.998	0.275

Table II. 3 Copper removal efficiency at different yeast extract concentrations.

Time (h）	0	4	8	12	24	36	48
0.5 g/L	0	0.61	0.59	1.42	1.61	0.39	0.78
	0	0.58	0.82	1.19	1.23	0.41	0.62
	0	0.19	0.23	1.21	0.58	0.62	0.99
1.0 g/L	0	0.62	2.58	7.42	18.79	62.41	64.58
	0	0.78	3.02	5.38	17.42	58.58	60.62
	0	1.02	2.58	4.22	20.58	60.98	63.22
1.5 g/L	0	0.78	5.62	13.58	42.79	44.42	45.18
	0	0.42	6.58	14.22	40.58	41.38	43.82
	0	0.22	7.62	16.18	38.98	43.78	44.22
2.0 g/L	0	0.58	13.62	20.98	23.22	24.62	27.58
	0	1.62	13.38	20.62	24.42	23.78	25.22
	0	0.18	10.42	18.18	24.22	26.78	26.18
3.0 g/L	0	0.62	2.98	4.62	5.78	6.42	7.58
	0	0.98	2.22	3.38	6.62	4.98	5.62
	0	0.58	2.62	6.18	6.42	7.58	7.22

Table II. 4 Urease activity (U/mL) at different yeast extract concentrations.

Time (h）	0	4	8	12	24	36	48
0.5 g/L	0.02	0.01	0	0.01	0	0.01	0
	0.02	0.01	0.01	0.01	0.01	0.01	0.01
	0.01	0.01	0.01	0.01	0.01	0	0
1.0 g/L	0.02	0.02	0.06	1.13	2.64	6.88	17.87
	0.01	0.04	0.08	0.9	3.86	8.74	14.77

	0.01	0.06	0.07	1.49	5	8.35	19.13
1.5 g/L	0.02	0.08	0.26	4.88	10.9	20.84	37.83
	0.01	0.06	0.25	3.88	12.23	22.65	32.2
	0.02	0.04	0.43	3.28	9.99	21.25	34.75
2.0 g/L	0.01	0.09	1.03	8.51	18.83	38.62	40.03
	0.01	0.1	0.83	7.82	20.35	38.83	42.23
	0.01	0.07	0.68	6.82	21.17	34.22	40.11
3.0 g/L	0.01	0.06	0.79	5.87	26.14	36.12	38.97
	0.02	0.07	0.9	6.63	24.72	38.24	41.23
	0.01	0.09	0.47	4.44	23.83	38.77	39.57

Table II. 5 NH_4^+-N concentration (mmol/L) at different yeast extract concentrations.

Time (h）	0	4	8	12	24	36	48
0.5 g/L	0.09	0.08	0.08	0.08	0.12	0.14	0.14
	0.08	0.11	0.09	0.09	0.13	0.15	0.16
	0.07	0.08	0.1	0.1	0.11	0.12	0.15
1.0 g/L	0.08	0.12	0.24	0.37	1.36	4.87	10.21
	0.08	0.15	0.25	0.55	2.21	5.49	11.79
	0.07	0.12	0.27	0.43	2.24	5.69	12.47
1.5 g/L	0.08	0.25	0.55	1.46	12.31	16.98	18.97
	0.1	0.22	0.63	1.52	14.63	16.48	18.63
	0.06	0.21	0.75	1.9	13.4	15.5	17.87
2.0 g/L	0.1	0.24	1.12	3.7	16.47	20.08	19.72
	0.1	0.16	1.23	4.99	16.79	19.87	19.2
	0.07	0.19	1.05	2.91	15.99	18.45	18.44
3.0 g/L	0.08	0.23	0.81	2.71	19.07	20.69	20.43
	0.09	0.19	1.05	2.9	18.18	19.22	19.69
	0.09	0.28	0.93	4.3	18.82	19.86	20.47

Table II. 6 pH and precipitation mass (mg/mL) at different yeast extract concentrations.

	pH	Precipitation mass (mg/mL)
0.5 g/L	6.58	0
	6.67	0

	6.61	0
1.0 g/L	8.58	0.7
	8.49	0.72
	8.64	0.67
1.5 g/L	8.78	0.54
	8.87	0.57
	8.84	0.57
2.0 g/L	8.89	0.31
	8.92	0.3
	8.84	0.29
3.0 g/L	9.02	0.03
	8.89	0.03
	8.87	0.03

Table II. 7 Effect of initial pH on removal efficiency.

Time (h）	0	2	4	6	8	12	24	36	48	72
2	0	25.23	37.6	52.76	62.02	65.67	66.48	63.1	66.42	64.85
	0	28.16	41.51	55.18	65.18	67.65	68.23	66.01	68.83	67.51
	0	31.08	45.42	57.59	68.34	69.64	69.97	68.92	71.24	70.17
3	0	42.17	62.61	70.66	72.1	81.33	79.66	80.59	82.17	80.91
	0	44.66	65.53	72.66	75.01	82.92	80.82	82.65	83.66	83.15
	0	47.15	68.45	74.65	77.92	84.5	81.98	84.71	85.15	85.39
4	0	49.43	67.89	76.71	77.04	82.22	81.91	82.35	81.84	80.7
	0	49.53	68.05	77.33	79.37	83.23	83.52	83.52	83.92	83.67
	0	49.64	68.2	77.95	81.69	84.23	85.14	84.69	86	86.64
5	0	50.88	70.73	82.45	86.14	86.2	86.63	85.37	85.61	85.58
	0	51.18	71.18	84.27	87.68	87.27	88.51	87.66	88.17	89.66
	0	51.48	71.63	86.09	89.22	88.34	90.39	89.95	90.73	93.74
6	0	23.63	32.8	42.88	49.98	53.27	54.44	54.01	56.25	56.73
	0	24.26	36.88	45.61	52.42	55.18	57.33	56.66	57.32	58.71
	0	24.89	40.96	48.33	54.87	57.1	60.23	59.31	58.39	60.69

Table II. 8 Zeta potential of microcapsules at different pH.

pH	2	3	4	5	6
rep1	-3.42	-8.51	-24.74	-31.78	-33.64
rep2	-2.50	-6.82	-22.20	-29.81	-32.01
rep3	-1.59	-5.06	-19.66	-27.82	-30.36

Table II. 9 Species composition at different pH.

Species composition	Pb^{2+}	$Pb(OH)_3^-$	$PbOH^+$	Pb_2OH^{3+}	$Pb(OH)_2$ (aq)	$Pb_3(OH)_4^{2+}$
1	100	7.29E-24	2.27E-05	4.01E-07	6.98E-14	9.06E-25
1.2	100	2.90E-23	3.60E-05	6.36E-07	1.75E-13	5.72E-24
1.4	100	1.15E-22	5.71E-05	1.01E-06	4.40E-13	3.61E-23
1.6	100	4.60E-22	9.05E-05	1.60E-06	1.11E-12	2.28E-22
1.8	100	1.83E-21	1.43E-04	2.53E-06	2.78E-12	1.44E-21
2	100	7.29E-21	2.27E-04	4.01E-06	6.98E-12	9.06E-21
2.2	99.99896	2.90E-20	3.60E-04	6.36E-06	1.75E-11	5.72E-20
2.4	99.99896	1.15E-19	5.71E-04	1.01E-05	4.40E-11	3.61E-19
2.6	99.99896	4.60E-19	9.05E-04	1.60E-05	1.11E-10	2.28E-18
2.8	99.99793	1.83E-18	0.00143	2.53E-05	2.78E-10	1.44E-17
3	99.99793	7.28E-18	0.00227	4.01E-05	6.98E-10	9.06E-17
3.2	99.99586	2.90E-17	0.0036	6.36E-05	1.75E-09	5.72E-16
3.4	99.99378	1.15E-16	0.00571	1.01E-04	4.40E-09	3.61E-15
3.6	99.99068	4.60E-16	0.00905	1.60E-04	1.11E-08	2.28E-14
3.8	99.98446	1.83E-15	0.01434	2.53E-04	2.78E-08	1.44E-13
4	99.97617	7.28E-15	0.02272	4.01E-04	6.98E-08	9.06E-13
4.2	99.96271	2.90E-14	0.036	6.35E-04	1.75E-07	5.71E-12
4.4	99.94095	1.15E-13	0.05704	0.00101	4.40E-07	3.60E-11
4.6	99.90573	4.59E-13	0.09038	0.00159	1.11E-06	2.27E-10
4.8	99.85186	1.83E-12	0.14316	0.00252	2.77E-06	1.43E-09
5	99.76484	7.27E-12	0.2267	0.00399	6.96E-06	9.00E-09
5.2	99.62809	2.89E-11	0.3588	0.00631	1.75E-05	5.65E-08
5.4	99.41262	1.15E-10	0.56743	0.00995	4.38E-05	3.54E-07
5.6	99.07179	4.55E-10	0.89623	0.01567	1.10E-04	2.21E-06
5.8	98.53724	1.80E-09	1.41272	0.02457	2.74E-04	1.37E-05

6	97.70227	7.12E-09	2.22014	0.03828	6.82E-04	8.45E-05
6.2	96.40423	2.80E-08	3.47187	0.05907	0.00169	5.12E-04
6.4	94.40381	1.09E-07	5.38838	0.08977	0.00416	0.00304
6.6	91.32808	4.20E-07	8.26178	0.13316	0.0101	0.01734
6.8	86.50264	1.58E-06	12.40236	0.18933	0.02404	0.09296
7	78.5217	5.72E-06	17.84212	0.24725	0.05481	0.43872
7.2	65.51331	1.90E-05	23.5937	0.27278	0.11487	1.60769
7.4	48.66363	5.62E-05	27.77686	0.23855	0.21432	4.15767
7.6	32.65928	1.50E-04	29.54418	0.17028	0.36129	7.92956
7.8	20.42059	3.74E-04	29.27794	0.10551	0.56744	12.23039
8	12.16927	8.87E-04	27.65358	0.05939	0.84943	16.33275
8.2	7.01792	0.00204	25.27401	0.0313	1.23039	19.76277
8.4	3.95825	0.00457	22.59298	0.01578	1.74319	22.37439
8.6	2.19994	0.01011	19.90055	0.00773	2.43365	24.23495
8.8	1.21071	0.02215	17.3573	0.00371	3.36414	25.48534
9	0.66165	0.0482	15.0347	0.00176	4.61825	26.24883
9.2	0.35964	0.10431	12.95245	8.22E-04	6.3055	26.59691
9.4	0.19451	0.22459	11.10225	3.81E-04	8.56635	26.5503
9.6	0.10464	0.48098	9.46587	1.75E-04	11.57568	26.07894
9.8	0.05591	1.02312	8.01595	7.91E-05	15.5361	25.101
10	0.02959	2.15539	6.72299	3.51E-05	20.65161	23.47042
10.2	0.01542	4.4726	5.55382	1.51E-05	27.03719	20.96965
10.4	0.00783	9.04247	4.47011	6.18E-06	34.4898	17.32829
10.6	0.00379	17.42567	3.4294	2.29E-06	41.93722	12.40133
10.8	0.00168	30.68476	2.40412	7.11E-07	46.59484	6.77147
11	6.41E-04	46.67461	1.45582	1.65E-07	44.71874	2.3832
11.2	2.10E-04	60.86502	0.75578	2.80E-08	36.79374	0.52845
11.4	6.23E-05	71.94137	0.35564	3.91E-09	27.44017	0.08727
11.6	1.75E-05	80.44442	0.15831	4.89E-10	19.35978	0.0122
11.8	4.74E-06	86.75334	0.06797	5.69E-11	13.17311	0.00153
12	1.25E-06	91.22967	0.02846	6.29E-12	8.7407	1.78E-04
12.2	3.25E-07	94.28779	0.01171	6.72E-13	5.69989	1.96E-05
12.4	8.34E-08	96.32135	0.00476	7.01E-14	3.67388	2.09E-06
12.6	2.12E-08	97.64736	0.00192	7.20E-15	2.35005	2.18E-07

12.8	5.38E-09	98.50306	7.72E-04	7.33E-16	1.4957	2.24E-08
13	1.36E-09	99.05004	3.09E-04	7.41E-17	0.949	2.28E-09
13.2	3.43E-10	99.39915	1.23E-04	7.47E-18	0.60088	2.30E-10
13.4	8.63E-11	99.61981	4.92E-05	7.50E-19	0.37998	2.32E-11
13.6	2.17E-11	99.75966	1.96E-05	7.52E-20	0.24008	2.33E-12
13.8	5.46E-12	99.84772	7.82E-06	7.53E-21	0.15162	2.33E-13
14	1.37E-12	99.90366	3.12E-06	7.54E-22	0.09572	2.34E-14
14.2	3.45E-13	99.93888	1.24E-06	7.55E-23	0.06042	2.34E-15
14.4	8.66E-14	99.96167	4.94E-07	7.55E-24	0.03813	2.34E-16
14.6	2.17E-14	99.97617	1.97E-07	7.55E-25	0.02406	2.34E-17
14.8	5.46E-15	99.98446	7.83E-08	7.55E-26	0.01518	2.34E-18

Table II. 10 Particle size distribution of three types of nanoplastics.

PS-Bare		PS-NH_2		PS-COOH	
Diamete (nm)	Percentage (%)	Diamete (nm)	Percentage (%)	Diamete (nm)	Percentage (%)
104.713	0	120.226	0	120.226	0
120.226	0.11308	138.038	4.78121	138.038	3.72938
138.038	6.58546	158.489	13.10913	158.489	11.15904
158.489	15.5455	181.97	17.11979	181.97	15.50938
181.97	19.29632	208.93	18.57441	208.93	17.47203
208.93	20.0799	239.883	16.65442	239.883	16.49487
239.883	17.06017	275.423	12.69075	275.423	13.51534
275.423	11.89991	316.228	8.21588	316.228	9.75158
316.228	6.50125	363.078	4.57924	363.078	6.29283
363.078	2.47137	416.869	2.35712	416.869	3.70953
416.869	0.44706	478.63	1.18859	478.63	1.84176
478.63	0	549.541	0.69817	549.541	0.51516
/	/	630.957	0.03131	630.957	0.00912
/	/	724.436	0	724.436	0

Table II. 11 Zeta potential of three types of nanoplastics at different pH.

Types of nanoplastics	PS-Bare	PS-NH_2	PS-COOH

3	-3.22	33.48	-8.99
	-1.24	38.75	-7.26
	-2.8	37.56	-6.44
5	-11.89	26.28	-22.34
	-8.55	32.14	-25.67
	-6.78	31.22	-21.68
7	-19.23	15.43	-40.26
	-16.45	18.33	-38.42
	-14.57	13.46	-37.32
9	-24.33	-0.23	-42.33
	-19.87	-3.38	-45.33
	-27.47	-1.74	-39.88
11	-30.35	-4.65	-43.38
	-34.24	-2.55	-45.89
	-26.77	-5.98	-48.68

Table II. 12 Physicochemical properties of copper tailings under different treatments.

Sample	CK			PEAT			MICP			PMICP		
pH	7.95	7.42	7.39	7.49	8.77	8.95	8.84	8.36	8.19	8.32	7.95	7.42
TN (mg/Kg)	112.39	279.53	318.21	299.67	457.12	514.76	495.83	862.35	927.14	904.81	112.39	279.53
NH_4^+-N (mg/Kg)	4.98	7.34	9.67	8.21	142.36	158.74	149.03	205.91	213.54	216.78	4.98	7.34
NO_2^--N (mg/Kg)	0.46	0.71	0.65	0.78	6.5	5.42	6.04	3.75	2.89	2.73	0.46	0.71
NO_3^--N (mg/Kg)	6.82	7.45	6.53	8.38	280.12	230.46	250.99	410.01	460.5	443.83	6.82	7.45
MBN (mg/Kg	0.42	4.8	4.93	4.38	2.08	2.42	1.91	6.07	6.38	6.95	0.42	4.8

)												
ON (mg/Kg)	77.91	240.12	270.51	255.87	90.01	75.33	81.73	226.16	247.51	240.12	77.91	240.12
TIC g/kg	32.73	32.26	32.89	31.14	38.18	39.88	39.83	38.26	39.85	39.22	32.73	32.26
TOC g/kg	1.18	9.74	9.54	9.86	1.09	1.21	1.04	9.69	9.36	9.29	1.18	9.74
DOC mg/kg	7.16	143.68	125.69	138.36	5.38	5.09	6.24	112.38	118.67	109.88	7.16	143.68
LOC mg/kg	91.24	874.32	935.67	907.55	79.38	70.26	65.49	668.77	709.87	725.34	91.24	874.32
POC mg/kg	219.87	2562.27	2649.87	2718.74	189.88	201.33	166.35	1046.98	897.38	1069.87	219.87	2562.27
MOC mg/kg	960.13	7177.73	6890.13	7141.26	900.12	1008.67	873.65	8643.02	8462.62	8220.13	960.13	7177.73
MBC mg/kg	5.48	31.32	33.87	29.76	21.35	17.88	19.64	49.38	54.67	43.85	5.48	31.32
Dehydrogenase activity (μg TPF/g/24h)	278.38	718.68	627.54	673.24	432.35	358.87	424.23	745.32	725.66	789.36	278.38	718.68
Urease activity (mg NH_4^+-N/g/24h)	0.49	0.9	0.71	0.75	1.5	1.21	1.45	2.32	2.15	2.23	0.49	0.9
Ammonia	0.08	0.28	0.21	0.25	0.36	0.34	0.35	0.5	0.42	0.45	0.08	0.28

monooxygenase activity (U/g)												
Nitrate reductase activity (NO_2^-/g/24h)	1.69	2.92	3.02	3.28	1.03	0.84	1.05	2.7	2.9	2.65	1.69	2.92
Nitrite reductase activity (NO_2^-/g/24h)	1.02	1.4	1.28	1.38	0.78	0.62	0.68	1.5	1.37	1.41	1.02	1.4

Table II. 13 Ryegrass biomass under different treatments.

Fresh biomass (g/m^2)	Shoot			Root		
CK	383.22	445.36	377.12	158.57	179.51	138.59
PEAT	1648.97	1723.68	1893.54	565.55	598.67	657.98
MICP	1045.63	1142.24	1298.37	397.04	423.17	481.23
PMICP	2112.37	1938.45	2024.56	651.97	623.23	684.38

Table II. 14 Chlorophyll and catalase activity of ryegrass.

Physiological traits	Chlorophyll a (mg/L)			Chlorophyll b (mg/L)			Catalase activity (U/g·min)		
CK	4.12	5.85	6.43	0.79	1.15	1.43	124.17	140.07	111.63
PEAT	9.85	11.42	12.63	2.09	2.88	2.91	88.82	97.55	100.37
MICP	10.18	10.74	12.56	2.32	1.89	2.84	106.54	117.09	103.26
PMICP	15.98	14.35	17.23	3.29	4.12	5.04	68.53	82.38	89.24

Table II. 15 Copper content in ryegrass.

Cu concentration (mg/kg dry weight)	Shoot			Root		
CK	50.12	68.95	58.47	320.56	385.42	303.25
PEAT	31.06	26.53	18.35	165.32	222.67	163.75
MICP	37.24	39.87	29.56	192.85	248.43	222.33
PMICP	8.75	15.32	11.93	54.16	68.92	92.38